THE EFFECTS OF AN SMA-BASED SLAT COVE FILLER ON THE AERODYNAMIC AND STRUCTURAL CHARACTERISTICS OF A WING PROTOTYPE

A Thesis

by

RYAN DAVID PATTERSON

Submitted to the Office of Graduate and Professional Studies of
Texas A&M University
in partial fulfillment of the requirements for the degree of

MASTER OF SCIENCE

Chair of Committee,	Darren Hartl
Committee Members,	Thomas Strganac
	Stefan Hurlebaus
	Nathan Tichenor
Head of Department,	Rodney Bowersox

December 2017

Major Subject: Aerospace Engineering

ABSTRACT

Current and new FAA regulations that are to be phased in have begun to pressure the aerospace industry to develop new noise reduction technologies to reduce aeroacoustic emissions that proponents say detriment the health and well-being of community members. With recent technological advancements improving noise emission from aircraft engines, emissions from airframe noise sources now project a larger footprint on the total emitted noise. This research proposes to investigate the previously developed shape memory alloy based slat cove filler concept and conduct aerodynamic and structural experiments with the purpose of characterizing the response under relevant flow conditions. The Texas A&M University 3'$\times$4' low speed wind tunnel will be used to determine the aerodynamic influences of the shape memory alloys based slat cove filler on wing performance. A previously developed wing prototype treated with a slat cove filler will be used to compare aerodynamic effects at multiple slat settings. Structural experiments was conducted using Digital Image Correlation measurements, and displacement measurements from a custom-designed laser displacement sensor to determine the structural response of the shape memory alloy slat cove filler during a typical retraction cycle under wind tunnel test conditions. Results from the structural experiments will be used to validate a finite element analysis model that will be used to further research development into computational modeling tools.

DEDICATION

Without my close friends and family, I would not have risen to the challenge and achieved as much as I have. Thank you very much for your unending support, words of motivation, and patience as I played with wind tunnel models in a basement laboratory.

ACKNOWLEDGMENTS

The road has been long and the struggle has been hard, but I would not have gotten as far as I have without the help and support of my friends and colleagues. I would like to personally thank William Scholten, my research partner on the Slat Cove Filler project. His assistance and help have been invaluable since the moment I first begun work on this project over two years ago.

I would like to thank the multiple exchange students from the ENISE school in St. Etienne, France. Jeff, Quentin, and Gregory all greatly contributed to work, and provided insight when it was needed most.

To Trent White, the undergraduate researcher working on this project, thank you very much. Your willingness to tackle difficult problems and create new, unique solutions have helped this research progress more than you think.

CONTRIBUTORS AND FUNDING SOURCES

Contributors

This work was supported by a thesis committee consisting of Dr. Darren Hartl [advisor], Dr. Stefan Hurlebaus of the Department Civil Engineering, Dr. Thomas Strganac of the Department of Aerospace Engineering, Dr. Nathan Tichenor of the Department of Aerospace Engineering, and special appointment chair Dr. Travis Turner of NASA Langley.

This work is done in collaboration with, and support of Dr. Travis Turner of the NASA Aeroacoustics Branch at the NASA Langley Research Center. The experimental wing prototype was developed with the assistance of William Scholten, Jeff Volpi, and Quentin Chapelon. Wind tunnel tests were conducted with the assistance of William Scholten, Trent White, and Quentin Chapelon. LABVIEW data analysis program was based on the framework developed by Yogesh Babbar and Vishvas Suryakumar. Digital Image Correlation testing was conducted with assistance from Rishabh Agrawal, and Gregory Methon. Data collected from the Scanivalve pressure scanner was analyzed by Trent White. Computational assistance was provided by William Scholten in model development and analysis of results. Testing and results from the NACA 0012 study in Appendix A was completed by Gregory Methon

All other work conducted for this thesis was completed by the student independently.

Funding Sources

This work was supported by funding from the National Institute of Aerospace (NIA).

NOMENCLATURE

CRM	Common Research Model
DIC	Digital Image Correlation
DOF	Depth of Field
FEA	Finite Element Analysis
FOV	Field of View
LDS	Laser Displacement System
NASA	National Aeronautics and Space Administration
PPDS	Pitch Plunge Drive System
psig	pounds per square inch (gauge)
SCF	Slat Cove Filler
SMA	Shape Memory Alloy
TAP	Tool Adapter Plate
TAMU	Texas A&M University

TABLE OF CONTENTS

Page

LIST OF FIGURES

FIGURE Page

LIST OF TABLES

TABLE Page

1. INTRODUCTION AND LITERATURE REVIEW

1.1 Overview and Background

Noise reduction in aircraft is important in the design process of, or upgrades to, any aircraft. With urbanification spreading the population to areas that were once limited to industrial and airport zoning, reducing aircraft noise in and around many developing communities provides a design challenge to aircraft designers. What once was an afterthought in aircraft systems design must now be deliberated on throughout the design process. In communities around the world, ranging from Heathrow Airport in London, UK, to Sky Harbor Airport in Phoenix, USA, reducing aircraft noise has become a topic of contention between residents and local governments [1], [2]. As populations increase in large metro areas, with air traffic volume increasing at a similar rate, there is now a larger voice advocating for lowered noise levels in and around communities [3]. The effects of aircraft noise on surrounding communities have been clearly documented citing multiple health studies, with provisions being made within the aerospace industry to focus new efforts on reducing noise generated from aircraft [4].

Aircraft can be generally separated into distinct categories: engine noise, air-frame noise, systems noise. After decades of engine design, by moving past turbojets to more efficient turbofans, the introduction of ceramic coatings to reduce wear, and the addition of exhaust chevrons to quiet engine exhaust during take-off and landing, noise reduction is now a critical criterion in engine design [5]. Significant strides have been made in lowering the noise threshold for aircraft engines to within an order of magnitude of aircraft systems such as hydraulics and electronics, and air-frame noise [6]. This research primarily focused on technologies and innovative methods in reducing the noise footprint of the air-frame. Some of the largest contributors to air-frame noise are the landing gear system

when deployed, high lift devices such as flaps, slats, etc., and any region of the aircraft that vibrates under normal operating conditions [7]. These contributing factors accelerate the transition from laminar to turbulent flow, often resulting in areas of separated and/or unsteady flow. Perturbations caused by the unsteady flow field and its interaction with the aircraft structure radiate as acoustic noise and that noise is most noticeable which are most noticeable during approach and landing flight phases, when aircraft engines are throttled down.

1.1.1 Slat Cove Filler Concept

One key contributor to air-frame noise is the leading edge slat [8], most significantly when deployed during the approach, and landing phases of flight. When the slat is deployed away from the wing, a gap between the main wing and slat is created, allowing flow to pass from the lower surface of the wing to the upper surface. As well, the lower surface of the slat is contoured primarily to stow flush with the main wing, rather than for aerodynamic efficiency. The inner contoured region between the slat and main wing produces a highly circulatory region of flow bounded by an unsteady shear layer. Unsteady flow mechanisms in the shear layer and its interaction with the recirculating region and the aircraft structure cause unwanted noise that can emanate into the surrounding environment [8], disturbing nearby communities, and can effect passenger comfort. This region between the deployed slat and the leading edge of the main wing is called the slat cove.

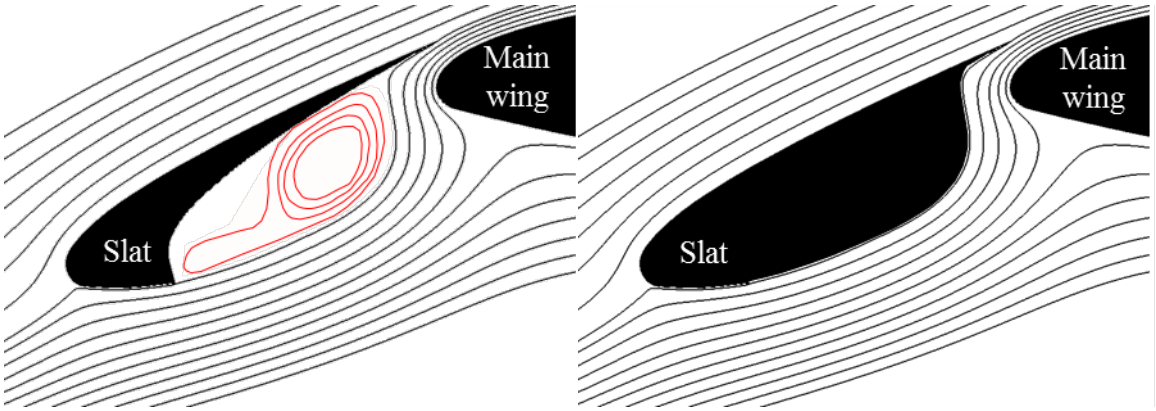

(a) Exposed slat cove

(b) Filled slat cove

Figure 1.1: Flow streamlines about the leading-edge slat in the high-lift configuration without and with the SMA slat cove filler.

One solution to reduce air-frame noise generated by the leading edge slat and circulatory flow regions in and around the main lifting surface of the aircraft, is to close-off or eliminate the slat cove region. Figure 1.1 demonstrates the circulation region aft of the slat, and shows the change when the cove is closed off from the flow. One such concept, called the slat cove filler (SCF), was investigated by Imamura et al. and advanced to structural concepts by Dr. Travis Turner and others at NASA Langley in the pursuit of reducing the aeroacoustic signature of high lift devices [9], [10], [11]. The proposed slat cove filler design would leverage the use of shape memory alloys (SMA) to enclose the circulation region in the slat cove when the slat is deployed, thereby reducing the aeroacoustic signature of the air-frame without adversely affecting the aerodynamic performance and with a small weight penalty. From preliminary work, it has been shown that the introduction of the slat cove filler reduces the aeroacoustic emissions by at least 10 dB [8]. Many designs were previously considered to fulfill the requirements of the slat cove filler; ultimately a continuous shape memory alloy sheet was found to be best in many cases to fill the slat

cove and have the ability to self-deploy [12].

The slat cove filler concept has ultimately moved forward with use of shape memory materials to achieve design requirements. However, multiple design iterations were required before a final concept was chosen. Designs utilizing inflatable cove fillers, composite materials featuring polymer skin with metal inner structure, and mechanical / hydraulic actuated components were all considered to satisfy design requirements [10]. The final concept consists of a thin, SMA sheet fixed to the upper trailing edge surface of the slat, and connected to the lower trailing edge through a hinge connection, allowing for self-stowage during slat retraction. The use of SMA material allows for the high strain required to stow inside the slat cove when the slat is fully retracted against the main wing, and provides sufficient stiffness to resist aerodynamic loading during typical flight environment during take-off, approach, and landing. For this research, the slat cove filler concept was advanced through the development of computational modeling tools, used to simulate the structural response during a full slat retraction cycle. This computational model was then validated through experimental testing of a scaled SCF wing prototype, tested in a wind tunnel environment to determine the aerodynamic effects and structural response.

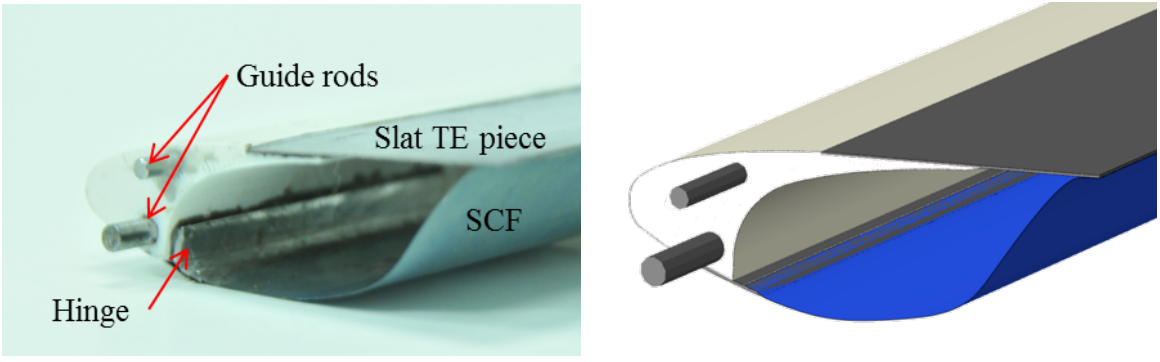

(a) Wing prototype slat

(b) Slat computational model

Figure 1.2: Slat Comparison

The SMA slat cove filler design is shown in Figure 1.2, which the SMA sheet attaching directly to the trailing edge of the slat. The lower connection between the SMA and the slat first connects a rotating hinge, allowing the flexible SMA sheet the ability to pivot up and into the slat cove during slat retraction and stowage. The SCF computational model matches the constructed experimental model to provide accurate validation from experimental results and to provide a framework for future development of aeroacoustic designs utilizing shape memory alloy materials.

1.1.2 Shape Memory Alloys

Shape memory alloys (SMAs) are a class of active materials that are known to exhibit a two-way shape memory effect that couples mechanical work with thermal energy. SMAs respond non-linearly to applied stress, depending on multiple factors: initial state, temperature, material phase, etc. Shape memory alloys exist in two main solid phases: Martensite and Austenite. The material microstructure differs between Martensite and Austenite. The Austenitic phase is characterized by having a cubic material structure, while when transitioning to Martensite, the material changes to a tetragonally shaped atomic configuration, shown in Figure 1.3 based on a figure created by Lagoudas et al [13].

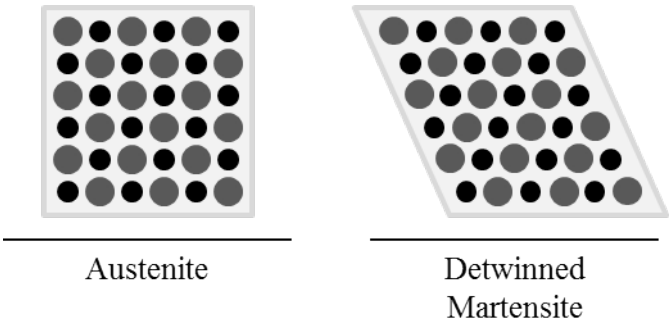

Figure 1.3: Material configurations of Austenite and Detwinned Martensite.

SMAs also have the highest energy density out of any class of active materials, making them ideal for actuators [13]. Multiple examples exist of SMA actuators being used in aerospace applications. For example, passive shape memory alloy actuators were used to control position of exhaust chevrons on Boeing aircraft. Work by Mabe et al. investigated the use of SMAs to replace mechanical actuators to passively control tip deflection on the exhaust section of an engine nacelle [14]. The advantage to using SMAs as actuators, is the activation though thermal input that caused the actuator to bend. The design used tuned SMA bars attached on each of the engine nacelle chevrons on the trailing edge of the nacelle near the exhaust. At low altitudes, the heat produced from the engine would overcome heat dissipation into the atmosphere causing the tips of the chevrons to deflect inward towards the exhaust nozzle. The tip deflection improved flow characteristics of the exhaust as well as a reduction in exhaust noise during take-off, approach, and landing. At high altitudes, the cooler atmospheric temperatures would cool the SMA actuators, extending the chevron tips outward and parallel with the freestream [6], [14]. This research has utilized SMAs as a passive flow control device used for noise reduction. This ability is obtained through the use of super-elastic SMAs which have ideal phase transformation properties.

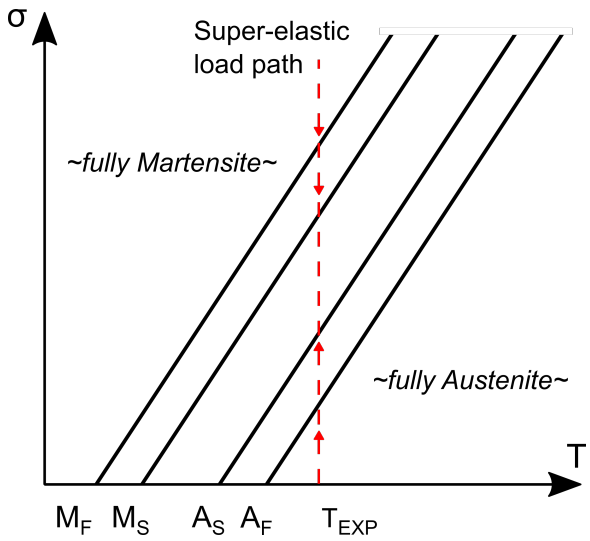

Figure 1.4: Super-elastic load path diagram of shape memory alloys.

Superelasticity, is associated with phase transformation from austenite to detwinned martensite and back without heating to rearrange the microstructure shown in Figure 1.4 [13]. This research used super-elastic SMAs to complete a full phase transformation cycle without the need for material heating / cooling. This is ideal in reducing the amount of required hardware and mechanical / electrical complexity of the SCF design. The SMA SCF is able to be fully retracted into the slat cove when not in use, experiencing high strains achievable by SMAs, super-elastically returning to the fully deployed configuration without the need for thermal input, and remaining sufficiently stiff to resist aerodynamic loading during flight.

1.2 Experimental and Computational Testing

The research conducted in this study seeks to investigate the aerodynamic and structural response of an SMA based slat cove filler. To determine the response of the SMA SCF, an experimental prototype, developed in continuation of the work by Scholten et al., were tested using the 3×4 low speed wind tunnel in the H. R. Bright Building at Texas

A&M University [12]. A variety of experimental methods were used to gather aerodynamic and structural response data to fully characterize the performance of the SMA slat cove filler. Aerodynamic loads and pressure distribution over the airfoil were collected to determine the aerodynamic effects of the SMA slat cove filler in multiple configurations of deployment. Of main interest is the comparison between an untreated slat configuration without a SMA slat cove filler, and a treated slat with SMA slat cove filler.

1.2.1 Wind Tunnel Testing

Prior to any flight testing, the aerodynamic response of any body or structure is typically tested experimentally in a wind tunnel, and modeled using a computational fluid dynamics program. Primitive wind tunnel testing can be traced back to the Wright Brothers era. Most notably, the Wright Brothers used rudimentary wind tunnels to develop airfoil shapes in preparation for their historic 1902 flight [15]. Wind tunnel testing is an important experimental validation tool for any aerodynamic design. Designers and researchers have used wind tunnel experiments to study the aerodynamic characteristics of everything from aircraft, ships and other nautical vessels, building structures, and even scale models of urban environments to measure how different wind directions and velocities affect city centers [16]. Modern technology has progressed from the early Wright Brother's design, adding complex environmental control systems to replicate different atmospheric strata, flow filtering methods to control or suppress turbulence, and the ability to replicate high Mach number flow conditions for reentry vehicles and other high speed experiments.

Data collected during wind tunnel testing is often used in making predictions about the fligh performance of a model or prototype. Most wind tunnel facilities have a limited test section area, requiring test subjects to often be far smaller than the full scale design. This work uses a 6.25% scale, two-dimensional airfoil section extracted from Common Research Model (CRM) developed jointly by NASA and the Boeing Company [17]. To

compare aerodynamic performance between subjects of different scaled sizes, multiple parameters are used to compare different flow conditions and aerodynamic response. Typically, for low speed applications the Reynolds Number, and Mach Number are used to scale viscous and compressiblity effects, respectively. To paraphrase from Wolowicz et al[18], the Reynolds Number is a non-dimensional scaling unit defined as the ratio of the inertial to the viscous forces acting on the boundary fluid layer above the surface of an object .

$$Re = \frac{\rho_\infty V_\infty L}{m u_\infty} \tag{1.1}$$

The Reynolds Number is important in comparing the turbulence transition point between objects; if the Reynolds Number differs by orders of magnitude, the flow over that object may transition from laminar to turbulence in a different location along the chord of that object. For this work, limitations in model scale and wind tunnel operating velocities limit the Reynolds Number to 300,000, while comparative full-scale values reach 30,000,000 during takeoff, approach, and landing phases of flight for the wing prototype. However, this work will not be used to directly compare and predict flight test results. Instead, the SMA SCF project will use results gathered from experimental testing to develop computational tools to accurately model the SMA SCF response. For this reason, matching Reynolds values between experiment and full scale is not required. The Mach Number is a non-dimensional parameter describing the ratio of the free stream velocity in reference to the speed of sound.

$$M = \frac{v}{a} \tag{1.2}$$

$$a = \sqrt{\gamma R T} \tag{1.3}$$

When the free stream velocity is greater than 0.3 times the speed of sound, fluid compressibility effects are more prominent in the aerodynamic response, requiring similarity

when comparing scaled experiments to full-scale operation. However for this work, both the full-scale free stream conditions and experimental test conditions are below the 0.3 M threshold value: 0.23 M full scale, 0.044 M experiment. As previously mentioned, while Reynolds and Mach Number matching during experiment is not possible with the current experimental set-up, this work instead will be used in the development of more accurate computational tools.

1.2.2 Digital Image Correlation

To determine the deflection of various structural features of the SMA SCF wing, digital image correlation (DIC) methods will be used during wind tunnel testing. Digital Image Correlation (DIC) is a non-intrusive, full-field, structural response measurement tool which captures and compares images to determine how the test subjects are re-positioned or deformed during the span of measurement. The origins of DIC are closely tied to photogrammetry, which compares images to determine the shape of three-dimensional objects. The foundation on which DIC is based is the analysis of the intensity of contrast in an image. A thin coat of paint is applied as a base layer to a test sample, either white or black matte. Then a speckle pattern is applied with contasting paint, either black or white matte, with a random or ordered pattern. Imaging software is used to correlate the intensity difference between the various speckles on the image and compares the test images to a reference image taken prior to testing. From this difference in intensity, the motion of each individual speckle is tracked in each collected image frame. From the sum-total of all speckles, the full-field response of the test sample is determined [19].

Commonly used in the aerospace industry, DIC systems have been previously used in determining the structural response of experimental prototypes inside a wind tunnel environment. Research by Wu et al., [20], investigated the deformation of a 80 mm flapping wing able to rotate 90°per flapping cycle in a micro air-vehicle application . The wing was

painted with a speckle pattern, and a DIC camera system was used to track out of plane displacements on the surface of the flapping wing. This test also used a strobe lighting system to synchronize the frequency of the image collection with the flapping frequency. This allowed for the prescription of the image sampling rate with respect to the flapping frequency by limiting strobe light activation [20]. As mentioned previously, research conducted by Albertani et al., [21], investigated large scale structural deflections using DIC of a micro air-vehicle during wind tunnel testing. A flexible wing body aircraft was tested at multiple flight configurations to measure the wing deflection. In this work, flexible wing design was a key factor in improving the aerodynamic performance of the micro air-vehicle by allowing for passive gust rejection in unsteady flows and improving the stall characteristics of the wing. DIC testing was used to measure the out of plane deformation over the entire surface of the wing through the use of a camera system mounted on the top of the wind tunnel test section. Similar experiments have been conducted for this research to determine the structural response and deformation of the SMA-based slat cove filler.

1.2.3 Laser Displacement Measurement

In conjunction with the lower mounted DIC system, a custom laser displacement measurement system was designed specifically for this work. In previous work by Wagner et al., [22], and Gwashavanhu et al., [23], laser vibrometry has been used to resolve vibrations in aerospace structures. One major limitation to using a laser Doppler vibrometry system is the inability to measure static structural deflections and low frequency oscillations on the order expected to arise in the SMA SCF. Research conducted by Wagner et al., [22]. investigated the aeroacoustic effects of exposed hanging stores under a variety of flow conditions. For aeroacoustic purposes, laser vibrometry is useful in determining the frequencies at which objects vibrate when exposed to flow, and how resulting vibrations are transferred through the structure and into the surrounding environment. Laser

vibrometry uses a single beam or multi-beam system to extract velocity information from a surface through the reflection of the emitted laser beam. Similarly, Gwashavanhu et al., [23], conducted experiments to determine vibrational mode shapes of a rotating turbine rotor. Vibrometry was used to measure structural oscillations parallel to the angular velocity of the rotor and experimentally determine the structural dynamics of the system.

For this current work, a laser displacement sensor was instead used to measure structural displacements of the SMA-based slat cove filler during a full slat retraction cycle [1] While the ultimate goal of the present research is to measure the aeroacoustic properties of the addition of an SMA-based SCF, this work has focused on the structural response of the SMA SCF under flow and its aerodynamic effects. The use of the laser displacement sensor allows the outer mold line of the lower surface of the wing to be measured though successive experiments, each comparing the lower surface of the SMA SCF as it transits though a full retraction cycle. Each retraction frame will be compared with data collected during DIC to determine the deflection of the SMA SCF during retraction.

1.2.4 Computational Modeling

Computational modeling allows researchers and designers to implement mathematical models describing systems not easily tested through experiments, allowing for cost effective design and testing. Computer modeling tools allow designers to develop and test complex new concepts without the need for expensive, iterative prototype fabrication, and they are able to replicate environmental and operating conditions of the intended design. The main deliverable in the present project is to develop and test new design tools able to model the complex interaction of shape memory alloys used in aerospace structural applications, specifically with the goal of reducing the aeroacoustic signature of high lift devices. Here we will focus on structural analysis and provide aerodynamic analysis

[1] Starting in the fully deployed state, the slat is retracted at 10% intervals until reaching the fully retracted state. Then the slat is deployed at 10% intervals until returning to the fully deployed state.

comparisons as well. For this research, ABAQUS CAE REFERENCE TO DASSAULT] was utilized in creating a model to describe the structural response of the SMA-based slat cove filler. A previously developed User Material Sub-routine (UMAT) was utilized to mathematically describe the thermo-mechanical response of the SMA SCF [24].

To accurately model the structural response of the SMA-based SCF, specific material parameters were required to fully define the non-linear response of shape memory alloys. For this work, a SMA material model based on the Souza-Auricchio model was used [24]. Due to this work utilizing superlastic SMAs in an isothermal environment, both in modeling and during experimental testing, a superelastic material model is most computationally efficient. The Souza-Auricchio model defines a set of seven material parameters and internal state variables which specify the structural response of the shape memory material, specifically the microstructural rearrangement during transformation. While there are more accurate and intensive computational solutions to modeling SMA response in the SCF, reduced modeling critera and the inclusion of purely superelastic effects allow for the computational efficiency of the Souza-Auricchio model [24].

The main focus of this research is to expand the body of knowledge contained in the CRM program [17]. This is achieved through the use of developing useful computational modeling tools while better developing aerospace applications. This research specifically is investigating the reduction in aeroacoustic emissions of the leading edge slat through the use of an SMA-based slat cove filler. Experimental testing will be conducted to develop accurate computational modeling tools which build off of previously developed tools. Previous work by Scholten et al. developed two-dimensional computational fluid-structure interaction tools used to model the SMA SCF under flow [12]. This work seeks to build on the previous model by expanding the structural scope to include a three-dimensional structural response. Deflection of the slat, and SCF during a full retraction cycle will be investigated at multiple points along the span of the wing. Results from experimental test-

ing will be used to validate computational model results, and conclusions implemented to improve further iterations.

1.3 Closing

The overall goal of this work is to design and test working, deployable SMA-based slat cove filler in a wind tunnel test conditions to determine the aerodynamic effects of the SCF, and to verify structural and aerodynamic computational modeling tools through wind tunnel experimental methods that non-intrusively measure structural response and to assess the lift, drag, and pressure distribution. This work will build upon the previous computational and experimental work of Scholten et al., [12], utilizing a previously constructed experimental model to develop a working slat cove filler. The multiple experimental methods and instruments by which the experimental and computational testing will be undertaken are discussed in the next section. Further, results from experimental and computational testing will be presented and discussed leading into future work on this topic.

2. EXPERIMENTAL TESTING METHODS AND COMPUTATIONAL MODELING DEVELOPMENT

2.1 Experimental Overview

To determine the aerodynamic and structural response of an SMA-based slat cove filler and to develop the necessary tools to design similar aeroacoustic structures, an experimental prototype will be tested in conjunction with computational modeling tools. This work builds on the computational and experimental work of Scholten et al., in which a fluid-structure interaction model was developed to investigate complex aerospace designs, and validated with experimental results [25]. In this section, descriptions of the testing facilities, instrumentation, an explanation of the experimental prototype, and experimental testing methods will be discussed. A computational finite element analysis model will be described, as well as assumptions made in the construction of the model. This work has primarily used an experimental prototype, previously developed and modified for this work, tested in the 3'×4' low speed wind tunnel in the H.R. Bright Building at Texas A&M University. To determine how the SMA SCF affects the aerodynamic and structural response of the wing prototype, experiments were conducted in a wind tunnel environment using multiple experimental methods and instruments. Wind tunnel testing was conducted to measure aerodynamic response and to determine the influence of the SMA SCF. Structural testing was conducted non-intrusively on the wing prototype during wind tunnel testing, and statically. Structural results will be compared to determine aero-structural response, and used to validate the computational model.

2.1.1 3'×4' Low Speed Wind Tunnel

Experimental work for this research was performed primarily in the fluid dynamics lab in the basement of the H.R. Bright Building at Texas A&M University. The facility is

home to multiple wind tunnels used for both research and classroom education to advance knowledge in fluid dynamics and morphing structures. For this work, the 3'×4' low speed wind tunnel was used to experimentally test the SMA-based slat cove filler in an relevant flow environment, shown in Figure 2.1. Each removable test section contains 3' W×4' H×7' L of usable space from which to explore the aerodynamic response of different prototype models, with the wind flowing through the long dimension of the test section. The 3'×4' is a closed-loop wind tunnel, where the air circulates continuously, passing first through the fan section, shown in Figure 2.2, to accelerate the air, then to a contraction section with flow filter to accelerate and straighten the flow, into the main test section, through a catch screen and expansion section, and then back through the fan blades to complete the loop. At the top of both corner sections, stator blades are used to turn the flow through the corner while limiting flow turbulence.

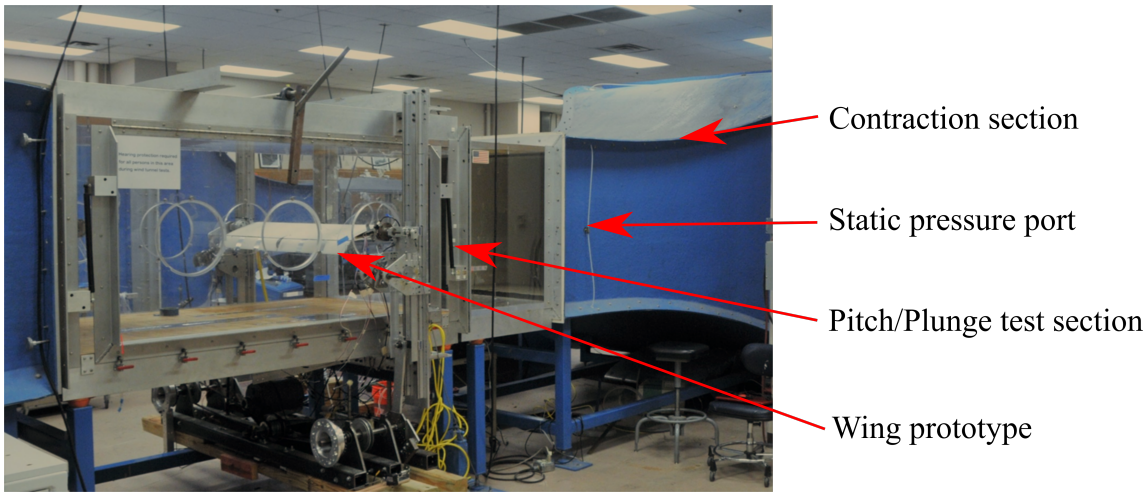

Figure 2.1: Texas A&M University 3'×4' low speed wind tunnel showing contraction and test section with installed wing prototype.

Prior to the contraction section and mid-way through the first turn, the flow passes

around a condensation-line cooling system. This system uses the cold waterline of the building to chill the circulating air to a constant 13°C when the tunnel is in operation. The temperature is monitored through the use of a thermocouple rod placed directly into the flow, upstream of the removable test section. This system allows for consistent testing conditions to easily repeat experiments, and a test metric from which to base any developed computational modeling tools. The wind tunnel is powered by a variable speed, constant pitch, electric motor-driven propeller that allows the 3'×4' wind tunnel to test experimental prototypes at free stream velocities of up to 50 m/s. For this work however, testing velocities are kept below 20 m/s to minimize any unwanted aeroelastic effects and eliminate the potential for structural deflections. Due to the use of 3-D printed parts in construction of the wing prototype, certain sections of the wing are much less stiff than if a steel or aluminum prototype were used. For instance, the trailing edge flaps have a tendency, at high angles of attack, to deflect outwards due to the impinging flow on the lower surface.

The 3×4 low speed wind tunnel has been used previously in multiple research projects and classroom experiments, and has produced repeatable, verifiable published results [26], [25]. For this work however, a qualitative flow visualization study was completed to determine whether any unwanted three dimensional flow effects were present during wind tunnel testing. This will be discussed in the following sections. The 3×4 low speed wind tunnel has three removable, re-configurable test sections, each with different methods of mounting experimental prototypes, and different methods of measuring aerodynamic performance. The first test section has a large hinged wall section to access experimental prototypes for installation, and a large electric motor powered, rotational floor mount, able to rotate 360° during testing. The second test section has a traversing roof and floor mounted sting to support prototypes from multiple surfaces. Each sting is attached to a force balance which measures the aerodynamic forces acting on the model prototype. The third

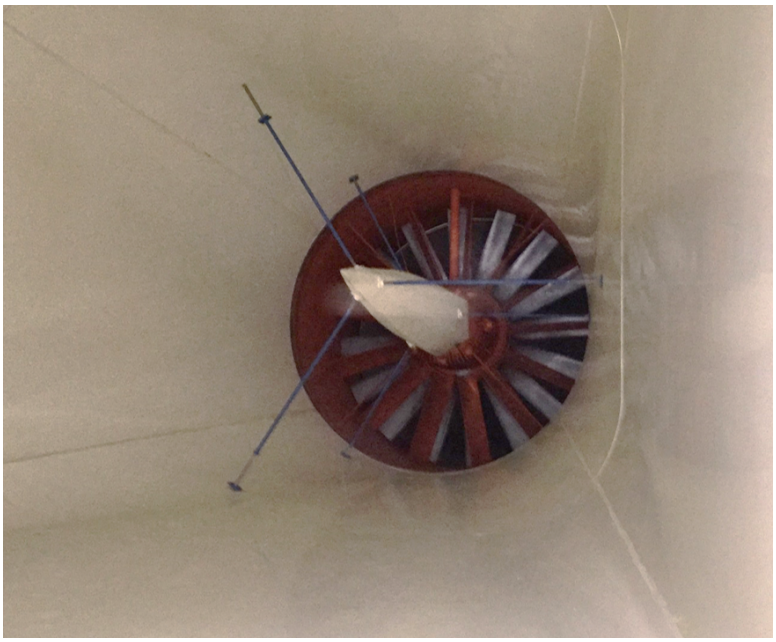

Figure 2.2: Fan section of the Texas A&M University 3'×4' low speed wind tunnel

test section, and one used for this work, has six wall mounting access ports from which to support experimental prototypes, which allow for prototypes to be cantilevered or fixed at both ends to the test section. This test section primarily secures test prototypes through the use of two, two-degree-of-freedom pitch/plunge mounting systems, one motor-driven, and the other free-response.

2.1.2 Wind Tunnel Test Section

As previously described, to determine aerodynamic and structural characteristics of an SMA-based slat cove filler, experimental testing was undertaken using the 3×4 low speed wind tunnel, the experimental prototype was mounted in one of the three removable wind tunnel test sections. This work utilized the Pitch Plunge Drive System (PPDS) test section, previously developed by Babbar et al.[26] and shown in Figure **??**. This specific wind tunnel test section has two pitch/plunge experimental mounting points, one motor-driven and the other free-response, from which to suspend experimental prototypes such

as wings or aircraft models. The test section has clear Lexan walls and ceilings to allow for experiments to be monitored during wind tunnel operation. The test section also has a 2" thick plywood floor panel with optical windows under the main wing mounting point to allow for various measurement systems to externally measure structural and aerodynamic data. The PPDS allows for a wing prototype, mounted span-wise from the side walls of the test section, to have motor-controlled, variable pitch angles and plunge positions, allowing for two-degree-of-freedom motion during wind tunnel testing. Secured to the test section and aligned with the first set of mounting ports, the PPDS is suspended from the top of the test section via aluminum L-section beams, and reinforced with a similar connection to the bottom of the test section structure. In this work, only the pitch mechanism is active during tests, as vertical plunge motion of the SMA SCF wing was not of interest. The pitch mechanism is powered by a Parker electric motor, and uses a motor controller to set the position and drive speed of the pitch mechanism. To vary the SMA SCF wing's angle of attack, a jog command is given to the motor controller to rotate the motor the desired amount. The current PPDS configuration powers the wing rotation on the port side, while the starboard side is free to rotate.

The PPDS test section is outfitted with multiple methods of measuring the aerodynamic effects on the SMA SCF wing prototype. The instantaneous angle of attack is measured through a US Digital Optical Encoder, mounted concentrically to the exposed PPDS rotation shaft and aligned with the installed SMA SCF prototype wing. To support the SMA SCF wing and measuring the forces acting on it, at each span-wise extent of the wing, an ATI Delta F/T load cell is directly mounted to the PPDS. The F/T load cell directly measures forces and torques acting on the SMA SCF wing along six-degrees-of-motion: F_x, F_y, F_z, T_x, T_y, T_z. Data from each load cell is collected in reference to each load cell's internal reference frame, aligned with the wing. A simple rotation about the pitch axis is required to transform the forces and torques from the wing centered frame to an inertial,

test section centered frame. From these forces and moments, the lift, drag, and pitching moment of the wing can be calculated. Shown in Figure 2.4, the reference frames used to convert loads collected by each load cell is shown. Prior to any data analysis, the load cell data must be converted from the individual load cell reference frame to an inertial reference frame with respect to the free stream velocity.

Of great interest to this work is the consistency and fidelity of data collection instruments used during wind tunnel testing. Noise in data streams is often caused by electromagnetic interference in the test environment, from improper grounding techniques, and from inconsistent power sources. A great deal of electromagnetic interference is generated by the PPDS when active and enabled[1] to control the pitch/plunge system.

2.1.3 Aerodynamic Data Collection

Data collection during aerodynamic testing is handled through a single data collection LabView routine. The code collects aerodynamic and environmental data from all of the wind tunnel instruments, except the Scanivalve pressure scanner, at a 100 Hz sample rate. The data code was developed by previous research groups, and expanded for this work to include instantaneous temperature measurement, free stream velocity, and slat and flap position control and tracking. To ensure all data streams have simultaneous collection rates, the code prioritizes data collection and only permits data to be written to file if sufficient memory is available. The front panel of the LabView virtual instrument (VI) has multiple added features to assist experimental testing in the 3×4 wind tunnel.

The front panel allows for live changes to the experiment, but is typically used to visualize data streams during the test. Within the data collection loop, preliminary data analysis is performed allowing live-stream updates of the wing pitch angle, instantaneous

[1]Note: When the system is powered but disabled, the general instrument noise is equivalent to background levels. However, when the system is enabled, instrument noise across all unshielded instruments significantly increases

coefficient of lift, coefficient of drag, as well as environmental status (temperature and free stream velocity). During the entire test, a rudimentary, unprocessed chart is populated with instantaneous values of pitch angle and coefficient of lift, creating a live lift-curve-slope plot. In figure 2.3, the main front panel view is shown for reader clarity. As mentioned in

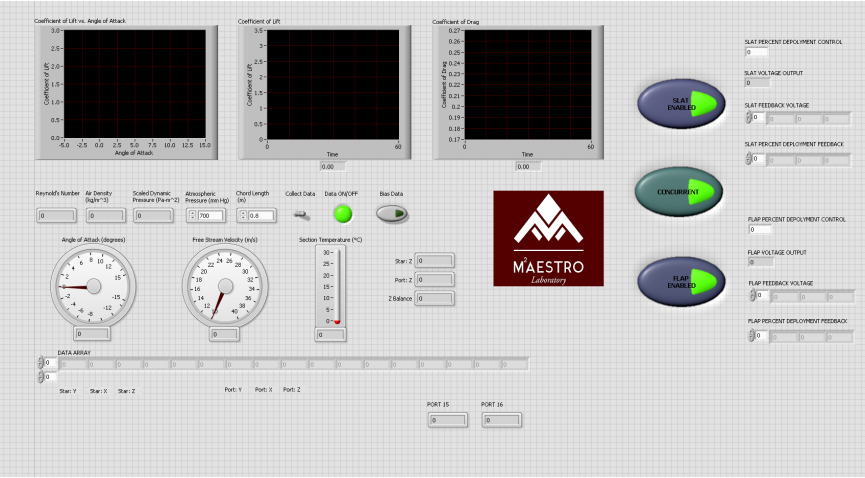

Figure 2.3: LabView front panel

the previous section, this work neglects transient aerodynamic effects, only static aerodynamic forces are of interest. The data collection code uses a toggle switch to save input data when desired, while still reporting test conditions when toggled off. This allows for suspension of data collection during pitch motion, high lift device retraction, and changes in free stream velocity. The data collection code is also designed to control and visualize the positions of the high lift device actuators. From the front panel viewport, the slats and flaps are independently controlled with a live output visualizing current position.

2.1.4 Aerodynamic Data Analysis

Once collected, the aerodynamic and wind tunnel environmental data must be analyzed and converted into usable and comparable forms. For this work, MATLAB was used to

post-process the aerodynamic data and to report collected data through plots and tables. The analysis program is based on the methods used in previous research in the 3×4 low speed wind tunnel [26], in which data collected from the ATI load cells are combined in the wing-centric coordinate system with inertial terms accounted for as a result of wing motion.

Data collected from all aerodynamic instruments (loads, temperature, velocity, angle of attack, etc.) are stored in a single, comma-delimited text file. For this work, only static, non-inertial measurements are of interest, so all changes in angle of attack are removed from the data set, up to the second derivative change. Next, all data collected at discrete angles of attack are averaged to give a single value for all forces, temperature, and velocity at each angle of attack. This is to take into account electromechanical interference caused by the PPDS, which has a large effect on temperature and free-stream velocity data signals. As well, this averages the aerodynamic forces applied on the wing at each angle of attack.

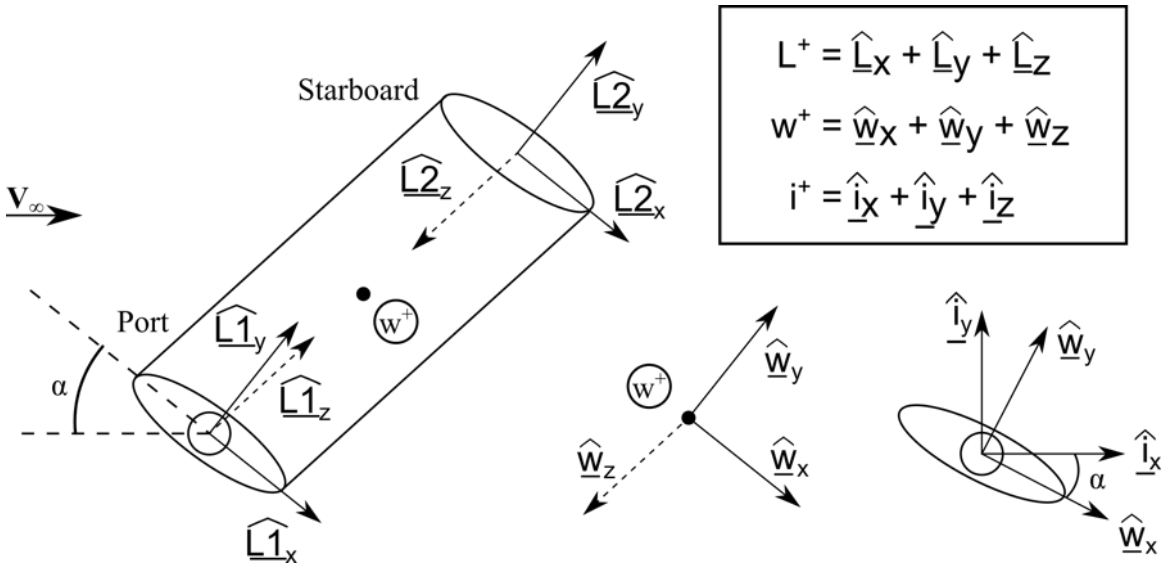

Figure 2.4: Diagram showing load cell, wing, and inertial reference frames of entire wing prototype system.

Figure 2.4 shows the various coordinate systems used in analyzing the collected data from wind tunnel tests. After averaging, loads from the load cells are reported in the local coordinate system of each ATI load cell, located at the extents of the wing. All forces are then combined and converted to the wing-centric coordinate system, shown in Equations 2.1, 2.2, and 2.3, located at point w in Figure 2.4. Forces are then converted to the inertial reference frame located at point w, that remains stationary with respect to the test section, using the direction cosine matrix shown in Equation 2.4.

$$F_{YW} = F_{YS} + F_{YP} \tag{2.1}$$

$$F_{XW} = F_{XS} + F_{XP} \tag{2.2}$$

$$F_{ZW} = F_{ZS} + F_{ZP} \tag{2.3}$$

$$C = \begin{bmatrix} \cos\alpha & -\sin\alpha & 0 \\ \sin\alpha & \cos\alpha & 0 \\ 0 & 0 & 1 \end{bmatrix} \tag{2.4}$$

From the inertial reference frame, lift and drag can be determined from the forces perpendicular and parallel to the free-stream velocity, respectively. To make comparisons between different wing configurations, the aerodynamic forces are non-dimensionalized into section coefficients of lift and drag using the free-stream dynamic pressure and the wing geometry. This also allows comparison with any computational fluid dynamics and fluid-structure interaction models that may have different wing geometries but use the same airfoil section. Equations 2.5, 2.6 represent the section coefficient of lift and coefficient of drag, where S is the planform area of the retracted wing geometry, V is the free-stream velocity, ρ is the free-stream density, c is the chord of the retracted wing geometry, and L and D represent the lift and drag respectively. Equation 2.7 describes the pitching moment

coefficient, which measures the stability of the wing in pitch.

$$c_l = \frac{L}{\frac{1}{2}\rho V^2 S} \tag{2.5}$$

$$c_d = \frac{D}{\frac{1}{2}\rho V^2 S} \tag{2.6}$$

$$c_m = \frac{M}{\frac{1}{2}\rho V^2 S c} \tag{2.7}$$

2.1.5 Experimental Wing Prototype

To validate the aerodynamic characteristics of the SMA-based slat cove filler, an experimental model was tested in the previously described wind tunnel facility. The wing geometry is based on the Boeing-NASA Common Research Model (CRM) with a rigid main wing structure and deployable slats and flaps. The CRM was developed in a joint effort by NASA and the Boeing Company to develop a wing template from which to base computational modeling tools [17]. The main wing is structurally supported by an aluminum main spar attached at each span-wise extent of the wing to an ATI Delta F/T load cell, which then mounts directly to the PPDS. Enveloping the main spar and prescribing the outer mold line as defined by the CRM geometry, a series of 3-D printed plastic, hollow, clam-shell parts are connected directly to the main spar through inset screws, flush with the lower surface of the wing. This construction method used allows for multiple airfoil section geometries to be quickly 3-D printed and easily installed to the main wing spar. This added flexibility gives this work the option of considering different span-wise geometries of the CRM independently, through the use of a multiple 2-D airfoil sections. 3-D printing was chosen for this work due to its extremely low material cost to procure

and manufacture quickly into usable parts. A typical top and bottom cover section of the wing, 1/6th of the entire span and shown in Figure 2.5, can be printed within (4 hours), then sanded to desired smoothness and installed on the wing by the end of one day. This flexibility allowed for multiple changes in design and the ability to damage parts without the high cost of manufacturing a solid steel or aluminum wind tunnel prototype. However, the tolerance of 3-D printed parts is still much less than that of machining a part from metal. Multiple rounds of wet-sanding, smoothing rough overlapping sections, and filling gaps to create a tight fit and smooth finish were required prior to wind tunnel testing. A SolidWorks model of the wing prototype is shown in Figure 2.6 with top covers removed to expose the inner structure.

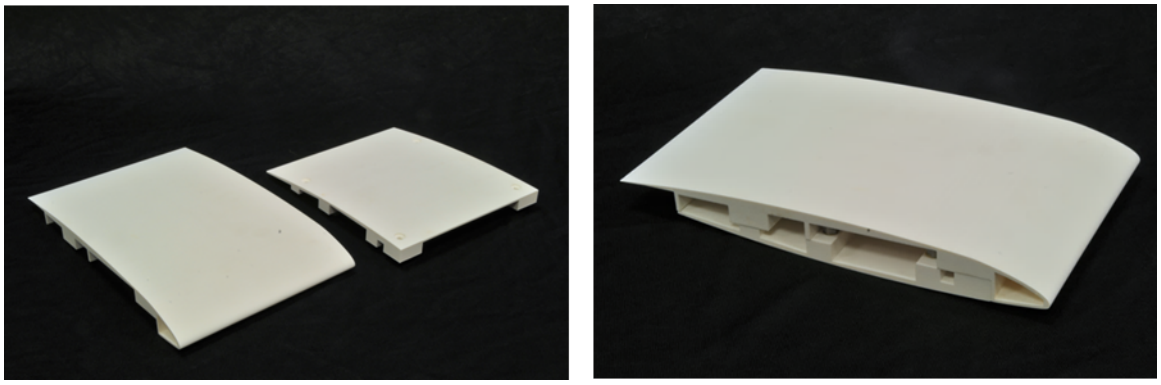

Figure 2.5: 3-D printed airfoil section of the SMA SCF wing prototype

To actuate the slats and flaps, a series of six powered and controllable Actuonix L12-R linear actuators, three each for the slats and flaps, are inset into the main wing spar and extend through the 3-D printed skin through rectangular ports on the leading and trailing edges of the main wing. The actuators are computer controlled and send continuous feedback signals, reporting the current actuated position of the high lift devices. The slats and flaps are formed using the same 3-D printed plastic as the main wing, and contain inter-

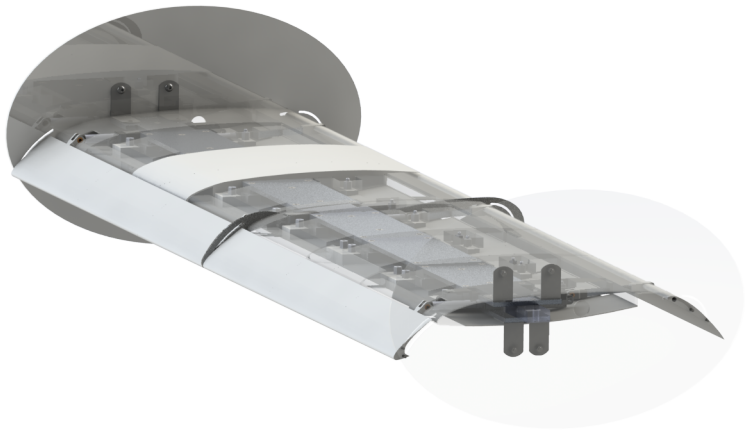

Figure 2.6: Exploded view of wing prototype SolidWorks model.

nal support spars that run the span of the slats and flaps for stiffening. Two sets of slats were used for this work: treated slats with the addition of the SMA-based slat cove filler, and untreated slats without aeroacoustic treatment. The SMA-based slat cove filler was connected to the slat directly at the trailing edge, and to a hinge along the lower surface to allow the SMA to pivot during retraction and deployment. The untreated slats provided a reference configuration from which to compare wing performance and determine the effects of an SMA SCF.

The hinge connecting the SMA SCF to the treated slat required multiple design iterations before a sustainable bond allowed for the hinge life to extend to multiple retraction cycles. Prior designs utilized nylon fabric hinges that would conform to the inner surface of the slat cove allowing for a strong bond to the slat. However, the nylon fibers proved problematic to bond to the smooth SMA surface. Accurate placement of the hinge location was investigated to minimize retraction force required from the actuators; however,

the bond overlap joint between the hinge and SCF needed to be sufficiently large to be of manufacturable scale. A steel spacer was fixed to the lower surface of the slat cove to both provide a stable and secure mounting surface for the hinge, and to move the hinge location further aft, in accordance with the results of the hinge placement study. Two-part, quick-bond epoxy was used to bond the hinge spacer, hinge, and SMA SCF to the lower surface of the slat. The top bond between the top trailing edge cusp and the SMA SCF was secured using a two-part metal adhesive. Preliminary testing however showed that frequent bond failure occurred at the top bond between the SMA sheet and the steel cusp. The adhesive, while secure to the steel, failed adhesively at the joint with the SMA material, requiring further investigation into SMA bonding methods. The final bond design utilized a surface pre-treatment on the surface of the SMA, which removed the unstable oxide layers present, while providing a bond foundation layer to assist the two-part metal epoxy. In Figure 2.7, the SCF bond layers are shown to clarify how the SMA SCF connects to the slat, the constructed slat is shown in Figure 1.1 a.

To specify the precise shape required to construct the slat cove filler, the SMA sheet needed to be formed and permanently set into shape. Shape setting is the process used to prescribe the stress-free configuration in shape memory alloys, and to instill the shape which will be "remembered" by the material after it deforms. The process is similar to annealing, by which the metal is constrained to a specified shape, heated to a certain temperature for a specified time, then promptly water quenched to quickly cool the metal and "seal" the prescribed shape. The complex shape needed for the slat cove filler required the use of steel mold blocks, shown in Figures 2.8, 2.9, to hold the Nitinol sheets to the required shape during the heating and cooling cycle. Equipment limitations limited the maximum length of Nitinol sheet that could be shape-set at once to less than 9.5", due to the interior dimensions of the furnace used for shape setting. By adding this constraint, it required the SMA SCF to have a segmented design, rather than be a single continuous

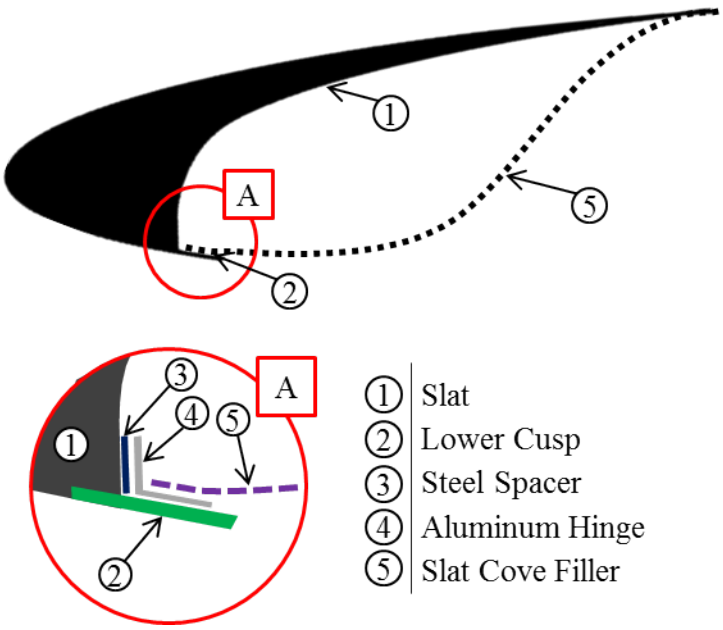

Figure 2.7: Construction diagram of slat with slat cove filler.

sheet between actuator connections.

Ideal shape setting conditions were tested though trial-and-error to find the temperature and time required to fully shape set the Nitinol sheets to conform to the SCF geometry. The time was initially set at 20 minutes, and the temperature was incrementally increased until the material began to "remember" the prescribed SCF shape. Time was then increased, keeping temperature constant, until the entire Nitinol sheet exhibited the shape memory effect, and conformed to the SCF geometry. The installed SMA SCF sheets were shape-set at 600°C for 30 minutes, then promptly quenched in room temperature water until cooled. To ensure that the shape-set material was completely treated, and to determine if any material changes had occurred during the process, extra material was set aside prior

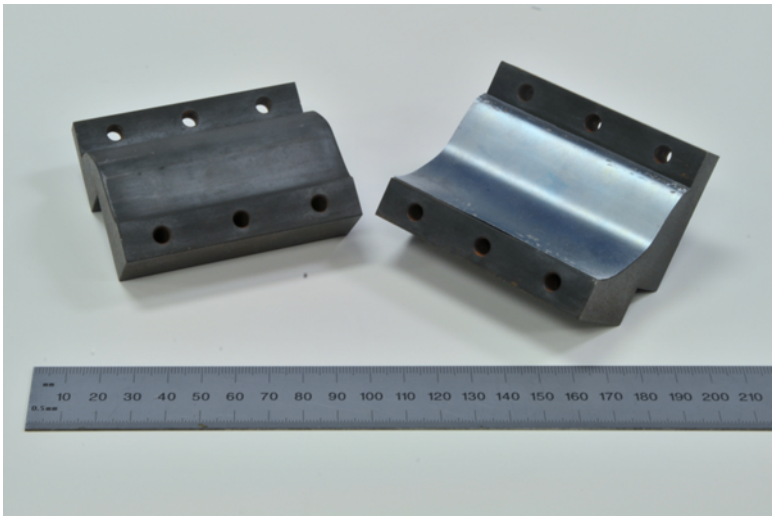

Figure 2.8: Shape set block with set SMA.

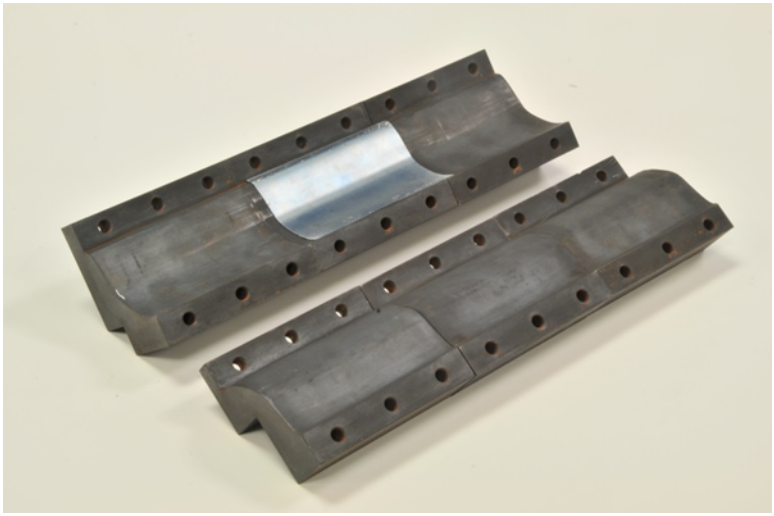

Figure 2.9: Full length shape set blocks for 23 cm SMA strips.

to, and after shape-setting for material characteristic testing using an MTS load frame. Data collected from the SMA characterization, shown in Figure 2.10, was then used to calibrate the material parameter model to develop a more accurate computational model of the SMA SCF [12].

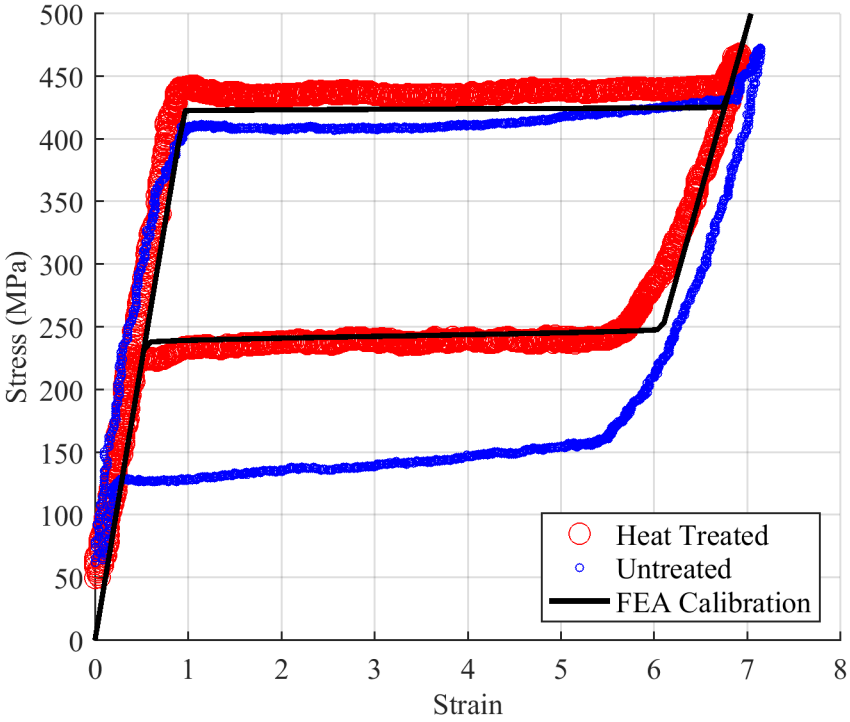

Figure 2.10: SMA characterization comparing standard and heat treated superelastic response.

2.1.6 Experimental Instruments - Wind Tunnel

To determine the aerodynamic characteristics of the wing prototype, multiple experimental instruments were used during wind tunnel testing to measure the lift, drag, angle of attack, flow conditions, and pressure over the wing prototype. This section will describe the systems used to accurately measure the test conditions in the wind tunnel test section, and how the flow effects the SMA SCF wing prototype.

2.1.6.1 Temperature

Constant temperature during experimental testing is important for repeatability of results, especially when considering the response of pseudoelastic SMAs [13]. The 3×4 low

speed wing tunnel used a forced convection water-cooling system placed upstream of the test section inside the flow loop. This system allows the wind tunnel, when running, to remain at a constant temperature of 13°C. Beyond allowing for a consistent test standard, the cooling system also acts to cool the electric motor powering the propeller. Without, the cooling system active, the motor would cause test section temperatures to rise to over 30°C. An internally mounted thermocouple, placed directly upstream of the test section, continuously reports the free stream temperature of the wind tunnel. The thermocouple interfaces directly with the LabView data collection program, and provides instantaneous temperature data used in calculating the free stream density of the flow.

2.1.6.2 Velocity

Free stream velocity in the test section is instantaneously calculated from multiple static pressure ports located upstream of the test section. Along the inner perimeter of the converging section of the 3×4 wind tunnel, at two locations, multiple static pressure ports collect air pressure in the wind tunnel and convey it through solid-walled pressure tubing to a differential pressure sensor. From the static pressure difference, velocity could be determined by relating the free-stream velocity to changes in the static pressure difference. To calibrate the velocity, and to provide a second trusted back-up system, pressure difference was recorded and compared with a FlowKinetics pressure differential sensor, shown in Figure 2.11. The FlowKinetics sensor uses an internally mounted pitot tube, at the upstream edge of the test section, and compares the static and total pressures to determine the free stream velocity. However, this system was unable to stream velocity data directly to the main data collection LabView program. Without instantaneous free stream velocity, variations in flow velocity due to tunnel blockage and rapid disturbances in the flow would not be recorded. During testing, the free stream velocity can decreased by up to 1.5 m/s when a wing prototype is pitched to high angles of attack. To calibrate

the differential pressure sensor for live measurements, the test section was emptied of all prototypes and sealed to reduce any turbulent effects from open portals. The free stream velocity, reported by the FlowKinetics device was compared with a differential pressure measurement at multiple free stream velocities until a there was a clear relationship between the two values. Of most interest was the range of free stream velocities between 12 m/s and 25 m/s, where most testing for this work was conducted.

Figure 2.11: FlowKinetics multi-function pressure, velocity measurement device.

2.1.6.3 Pressure

Pressure measurements were recorded at two times during wind tunnel testing: once prior to the test to measure the atmospheric conditions at the time of testing, and during the test to gather more information about flow over the wing prototype. The former will be discussed in the next section as it pertains to initialization prior to each experiment. A Scanivalve MPS4264 Miniature Pressure Scanner was used, to report and collect instantaneous static pressure during wind tunnel testing. The Scanivalve, shown in Figure

2.12, is a multi-port scanning pressure sensor capable of collecting instantaneous pressure measurements at up to 2500 samples per channel per second. The model used in this work has two sets of 32 pressure ports mounted in separate "test banks" installed down the long axis of the pressure scanner. Each test bank had a separate calibration. Half of the pressure ports (32) were scaled to read pressures between -1 to 2.5 psig. The other half, and the section used for this work, were calibrated to $\pm$ 1 psig. The device is accurate up to a resolution of 0.06% of the full scale pressure range (i.e. 0.0006 psig or roughly 4 Pa) The Scanivalve device internally calculates the instantaneous pressure and references with respect to a port reading the static pressure in the test section. The Scanivalve is able to report data in multiple usable formats. For this work, the pressure collected from the Scanivalve was not collected in synchronization with the main LabView data collection program. At each discrete angle of attack, high lift device location, and free stream velocity, the pressure was collected to be post-processed after each wind tunnel experiment.

Figure 2.12: Scanivalve MPS4264 Miniature Pressure Scanner

2.1.6.4 Force and Torque System

To directly measure the forces and torques acting on the SMA SCF wing prototype, a set of two ATI Delta F/T transducers were mounted at the wing connection points of the PPDS. The ATI Delta load cell is encastered to an adapter using the Mounting Adapter Plate, provided with the ATI load cell on the PPDS locking all motion and rotation with the motion of the PPDS. On the opposite end of the load cell, the connector for the wing prototype is secured to the Tool Adapter Plate (TAP) such that the entire load path of the wing passes through the TAP for accurate measurements. The ATI Delta load cell is a six-axis force/torque measurement system capable of measuring three forces and three torques aligned with its internal 3-dimensional coordinate system. The X and Y directional sensors, of most interest to this work, are able to sense and measure forces up to 330 N with an accuracy of 1/8 N.

2.1.6.5 Electrical Noise

Each electronic device used to collect data from experimental testing has an electrical error associated with it. Data collection systems transmit data through voltage signals to a data collection suite, in our case a Data Acquisition device (DAQ). This voltage is never perfectly constant, and oscillates a small amount around the actual measurement result. The variation, or noise, associated with each data collection instrument is determined by multiple instrumental, and environmental factors. Environmental electromagnetic signals often interfere with, and cause increases in data collection noise. As noted previously, it has been hypothesized that the Pitch/Plunge device, when active, disrupts data collection instruments. To determine the effects of the PPDS, and on what instruments, data noise tests were conducted with and without the PPDS system engaged. In Figure 2.13, signal variations are shown from the F_X output channel from on of the ATI F/T load cells. The output value has been offset to clearly show differences in signal variations. From multiple

experiments, it was found that the ATI F/T load cells are relatively unaffected by the electromechanical interference from the PPDS.

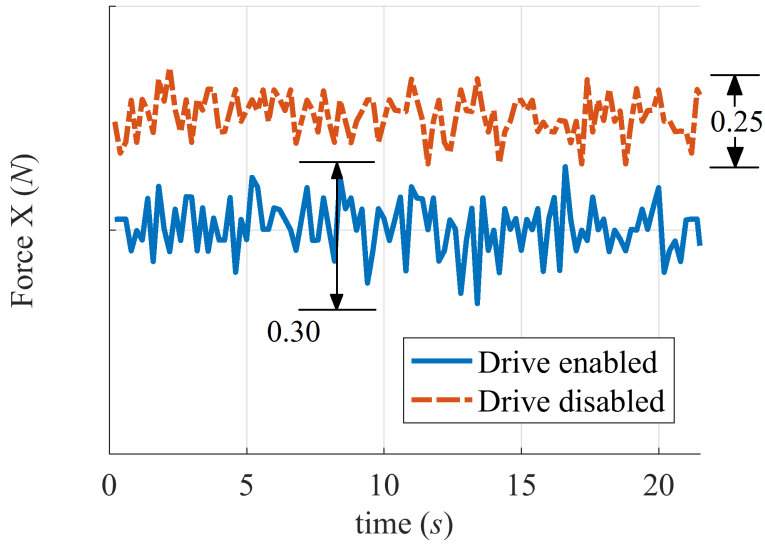

Figure 2.13: Normalized data signal from ATI F/T load cell F_X channel comparing interference caused by PPDS activation.

Other systems, especially ones which transmit data signals through un-shielded cables, are highly effected by outside electromechanical (EMI) interference. Of greatest note is the variations in noise collected from the velocity sensor system. This system uses un-shielded cables to connect the differential pressure sensor to the DAQ system. As expected, this system is highly effected by the introduction of EMI emissions from the PPDS system. This noise is present in both wind-off PPDS activation and wind-on PPDS activations, shown in Figure 2.14. As in previous, the signal value has been adjusted to allow for comparison between signal variation levels. To determine which systems are most influenced by EMI emissions from the PPDS and other sources, multiple experiments were conducted with results recorded in Tables 2.1 and 2.2.

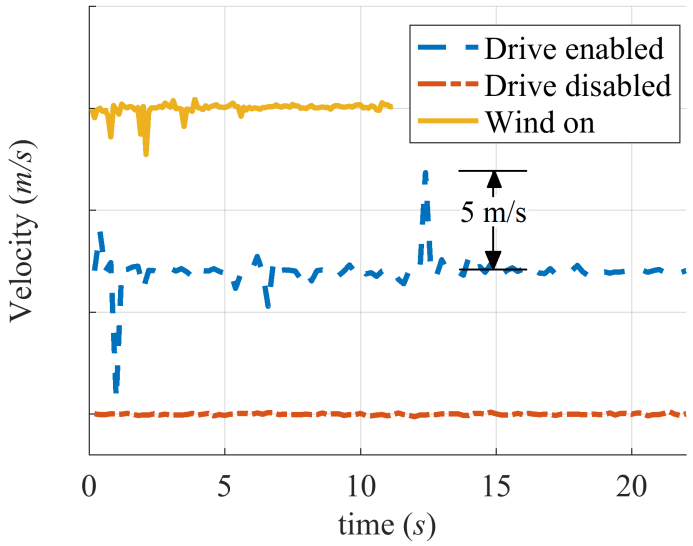

Figure 2.14: Data signal from free-stream velocity sensor comparing normalized signal noise at various stages of testing.

	Pitch/Plunge On	Pitch/Plunge Off
ATI F/T F_X	0.0489	0.0521
F_Y	0.0559	0.0651
F_Z	0.0897	0.1079
T_X	0.0042	0.0045
T_Y	0.0025	0.0025
T_Z	0.0017	0.0020
Temperature	0.0413	0.0364
Velocity	0.0409	0.6446

Table 2.1: Standard deviation from mean of instrument signals.

2.1.7 Wind Tunnel Testing Procedure

To ensure accurate and repeatable results from experiments in the 3×4 wind tunnel, a procedure was devised to standardize testing. Prior to any set-up of data collection software, the internal atmospheric pressure in the laboratory space was recorded from a manually calibrated mercury manometer. Typically, the pressure recorded in the lab did

	Pitch/Plunge On	Pitch/Plunge Off
ATI F/T F_X	0.3060	0.2630
F_Y	0.3460	0.3020
F_Z	0.6320	0.5170
T_X	0.0250	0.0210
T_Y	0.0150	0.0120
T_Z	0.0120	0.0130
Temperature	0.1820	0.2600
Velocity	11.123	0.2600

Table 2.2: Uncertainty of experimental instruments.

not deviate by more than 1-2 mm Hg from the atmospheric pressure recorded hourly by the weather station located at Easterwood Airport (KCLL), roughly 3.5 miles away from the laboratory. Once the atmospheric pressure at the time of test is recorded, a final inspection of all structural connections on the prototype, debris check in the test section, and cable connection checks are performed. This is both for safety concerns as well as a final check on data collection suites to ensure a test is carried out safely and with all data streams intact. Loose connections can cause catastrophic structural failure of a wing prototype under flow, and cause unintended load paths which alter the test results.

To initialize the data collection systems and standardize how each experiment is conducted, the wing prototype being tested is initially set to 0° angle of attack. A hand-held, digital inclinometer is placed on top of the main wing spar connection joint with the load cell on the free end of the wing prototype (starboard side). The wing is slowly pitched using the PPDS until the inclinometer reports an angle with the test section floor of 0.00° angle of attack. Even a slight misalignment will have drastic effects on the aerodynamic results of the test, shifting the lift-curve-slope. The angle initialization was performed twice, or until a repeated read-out of 0.00° is reported, for accuracy.

Once all final safety pre-checks have been performed, atmospheric pressure recorded,

and pitch angle set, the data collected code is started and biased with respect to initial starting conditions. The initial loads and angles are tared to zero. The test velocity is then dialed into the wind tunnel controller unit and the test begins. This work only considered the static aerodynamic effects of the SMA SCF wing prototype and as such, only static measurements were collected. All transient events, during active pitch control, deploying and retracting the high lift devices, and any changes in free stream velocity were not recorded by the data collection program. This was done primarily to reduce data analysis complexity and standardize test procedures. Future work on this research topic, which will be discussed in later sections, may include the transient effects of slat deployment and retraction.

2.2 Structural Testing and Computational Modeling

The structural response of the SMA SCF is of interest to this work to determine the kinematic and deformation characteristics during stowage and to determine the static and dynamic response and stability of the structure with flow. Two methods will be used in conjunction with computational modeling to determine the structural response of the SMA slat cove filler. Introduced in Subsection 2.2.1, Digital Image Correlation (DIC) enables investigation of the slat and slat cove filler deflections during wind tunnel testing without physical contact or flow influence over the wing. DIC testing was conducted at both wind-off and wind-on flow conditions to determine the aerodynamic influence on the structural response. Separately, to confirm DIC results, a custom-built laser displacement sensor was mounted beneath the test section to measure deflections of the slat and slat cove filler, as introduced in Subsection 2.2.2. Due to EMI noise emissions during wind tunnel testing, the laser displacement experiments were only conducted in the wind-off configuration. The experimental results from the two testing methods will be used to validate a finite element analysis (FEA) model, developed using ABAQUS CAE to predict the structural

response, introduced in Subsection 2.2.3. Ultimately, the results from experimental testing and the FEA model will be used to determine how the SMA SCF responds to aerodynamic loading.

2.2.1 Digital Image Correlation

Conducting structural experiments, especially non-contact measurements, in a wind tunnel environment provides a great deal of challenges, but is contrasted with the useful results determined from testing. Often, direct measurement tools such as strain gauges are required to be installed in locations such that the aerodynamic characteristics of the subject are not altered. This limitation is further compounded with the current wing prototype used to test the slat cove filler response. At a 6.25% scale of the full-size CRM wing, the prototype measures 0.3216 m (1.06 ft) along the chord in the retracted configuration, and 1.219 m (4 ft) along the span. This small size makes direct structural measurement a challenge. As well, the SMA SCF is directly exposed to the flow, limiting possible placement of external measurement instruments. For this work, non-intrusive, far-field measurement systems will be used to measure the structural response of the SMA SCF.

2.2.1.1 Test Configuration

For this work, a two-camera set-up is used, allowing for 3-D DIC testing, which corresponds to the measurement of out-of-plane deflections. Comparing between the base calibration image set and an initial reference image, the DIC software is able to resolve the location of the speckled sample of interest in three-dimensional space. Mounted directly underneath the wind tunnel test section, the DIC cameras are pointed upwards, viewing the underside of the wing through a Plexiglas window on the floor of the test section shown in Figure 2.15. The camera system is mounted roughly 1.0 m from the test specimen using a standard t-slotted rail system giving both flexibility in camera alignment and a secure connection isolated from wind tunnel vibrations. Two Point Grey Grasshopper3

USB3 cameras with 60 mm NIKKOR Nikon f/2.8 D micro lenses were used for this test. The camera / lens set-up was chosen for this test to maximize the depth-of-field (DOF) available for clear images, while limiting the field of view (FOV). For the test set-up, the DOF and FOV allowed by the lens configuration were: 3 cm, and 16 cm respectively. Spot lighting of the area of interest to be viewed is important to give the most contrast between the white background, and the black speckled pattern. This contrast is what the VIC 3-D software uses to determine distance and orientation of the sample. Preliminary SMA SCF testing showed an maximum out-of-plane deflection of 15 mm; this limitation coupled with the distance between the specked SMA SCF and the camera system required an intermediate micro lens to retain high resolution imaging with a large DOF. The first round of testing utilized a Tokina 100 mm fixed focal length lens pair only achieving 1 - 2 mm of out-of-plane focus; the required depth of field was not possible with that set-up, so a pair of 60 mm lenses were purchased. The improved lens selection in the current set-up allows for greater than 3 cm of out-of-plane focus. The two-camera set-up is connected via USB3 directly to a computer running VIC 3-D DIC analysis software.

2.2.1.2 Surface Preparation

The treated slats are painted using a two-step system to emphasize the contrast of the speckle pattern. A light coat of white, matte, non-reflective latex paint is first applied to the surface of interest. in this case, the lower surface of the slat from the leading edge, including the lower slat cusp, and along the SMA SCF ending at the trailing edge of the slat. The leading edge of the main wing is painted matte black to act as a contrasting boundary surface to delimit the slat from the naturally white 3-D printed plastic wing. The speckle pattern is applied using a Correlated Solutions patterned stamp roller, shown in Figure 2.16 with evenly spaced, equal sized raised circles with slight imperfections to add speckle contrast. This allows for consistent speckle pattern resolutions to better match the

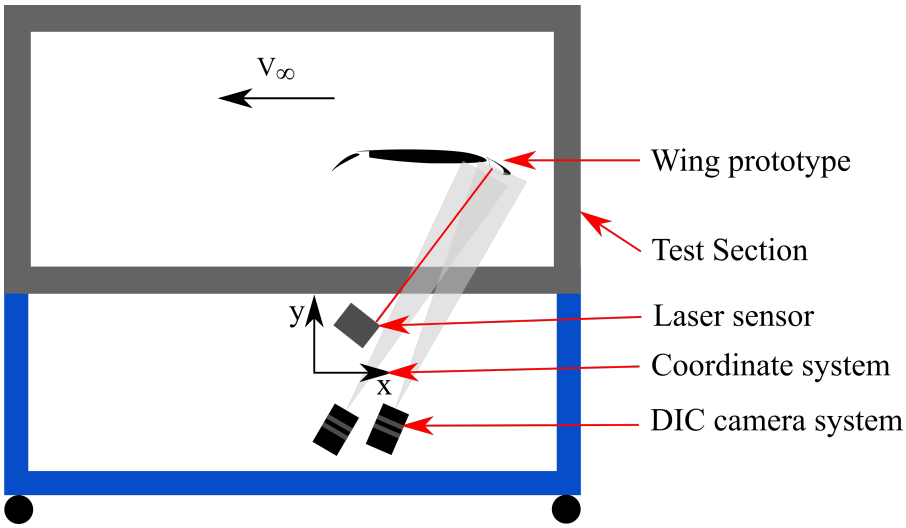

Figure 2.15: Schematic of DIC and LDS sensor alignment beneath wind tunnel test section.

chosen calibration disk. Due to the complex curved shape of the SMA slat cove filler, an interior jig was required to keep the SMA sheet from deforming and "snapping-in" to the slat cove during pattern application, since significant pressure must be applied to achieve a consistent speckle pattern. A 3-D printed jig was constructed to be placed inside the slat cove to restrict the SMA SCF from deflecting inward during speckle application. The speckle pattern was applied in multiple coats; the complex curve only allowed for application along the span of the slat, rather than along the chord length. Figures 2.17 and 2.18 shows the lower surface of the treated SMA slat with applied speckle pattern.

2.2.1.3 Calibration

A Correlated Solutions (3 mm 14x10) calibration disk, shown in Figure 2.20, was used to calibrate the test system prior to data colletion. The calibration disk, when photographed in multiple rotational configurations, allowed the DIC software to determine the orientation of the cameras with respect to each other and to the speckled sample. To accurately calibrate the DIC system, the wing was pitched-up to over 13° angle of attack, away from

Figure 2.16: Correlated Solutions 0.07" speckle roller

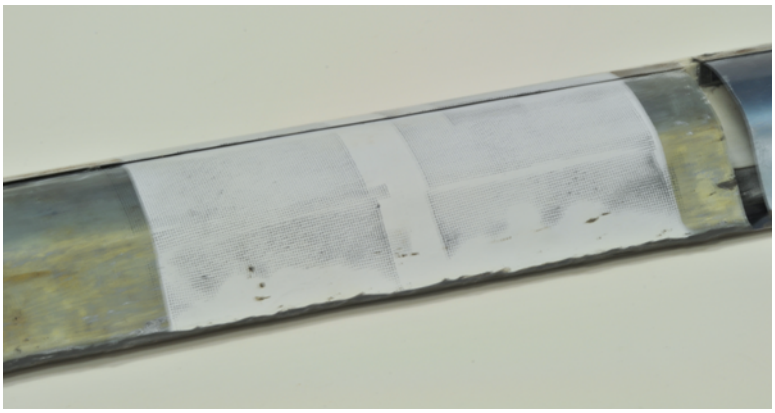

Figure 2.17: Lower surface of the treated slat section with speckle pattern for DIC testing.

testing configuration. The calibration disk was held steady in the region of focus. It is important to keep the calibration disk in maximum focus during set-up, without changing the physical lens focal point. Multiple images were then taken of the calibration disk in multiple rotation configurations. The disk was rotated along each axis with at least 15 images collected along each rotation path to get a complete calibration sample of images. The internal software package (VIC3D) imports and analyzes the calibration files to determine if an accurate three-dimensional space can be constructed to measure out-of-plane structural responses. If the software determined an insufficient set of calibration images, either from poor camera focus, lighting, or from calibration disk blockage, poor images

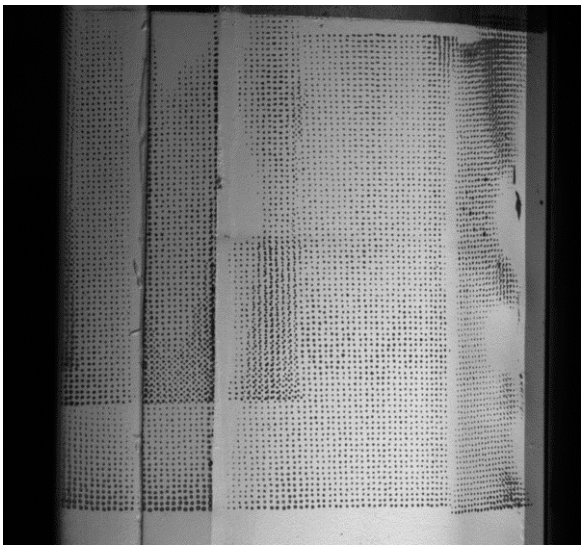

Figure 2.18: Speckle pattern shown on the lower surface of the treated slats

could be either removed from the calibration file group, or the calibration sequence could be repeated with new images. It is important to note that calibration can be conducted either prior to, or after DIC test images are collected, however for this work, each DIC test was preceded by calibration to ensure the test set-up produced DIC images of good quality.

2.2.1.4 DIC Testing

DIC testing was separated into two main experiments: wind-off and wind-on. Results from both experiments were then compared to determine the change in structural response. The wind-off test was conducted with the SCF prototype wing held constant at six degrees angle of attack and at zero free stream velocity. This test acted as the control from which to base the structural performance. The slats and flaps were simultaneously retracted from the fully deployed starting configuration, stopping at each 10 percent deployment interval. This was done to replicate flight conditions in all wind-on experiments, since slats and flaps are often simultaneously deployed in the landing and approach phases of flight. All

high lift device configurations will be referenced in terms of percent deployment, with the actuation direction being noted as: retracting direction or deployment direction. At each interval, the camera system was commanded to collected one image from each camera. During the wind-off experiment, the slats and flaps underwent a single retraction cycle, fully retracting to 5 percent deployment, then subsequently deploying back to 100 percent deployment. The retraction arc was halted at 5 percent deployment to reduce the possibility of damaging the slat cove filler connection bonds and the actuator connection pin-joint. This test was repeated to test the wind-on response of the SMA SCF during a single retraction cycle. The wing was held constant at six degrees angle of attack at 15.5 m/s free stream velocity. The high lift devices then underwent a full retraction cycle, pausing at each 10 percent interval and again at 5 percent deployment. The images gathered from the test were then processed using VIC 3-D software to resolve the structural response of the SMA SCF during the retraction cycle.

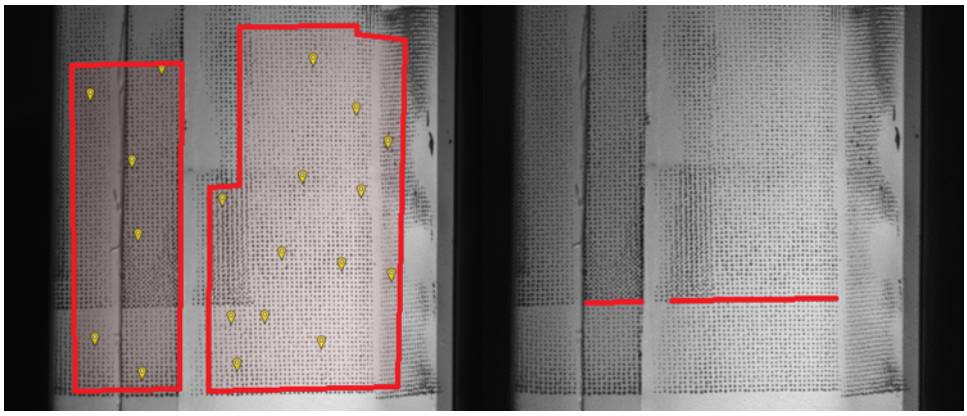

(a) Area of interest (b) Line of interest

Figure 2.19: VIC 3-D analysis areas.

2.2.1.5 Data Processing

The VIC-3D software package was used for this work to resolve the 3-D DIC images collected during wind tunnel tests. To effectively use 3-D DIC, The analysis system requires information on the camera position and orientation with respect to the test sample to create a 3-D full-field analysis. The calibration images, either taken prior to, or after the test, are analyzed by VIC 3-D to determine test configuration. Test images are then uploaded, with each test frame containing an image from each of the cameras used. To begin the analysis, an area of interest must be manually chosen within the bounds of the speckle pattern. For this test, two areas of interest were selected; one along the slat cusp to reference rigid body motion shown in Figure 2.19, the other on the SMA SCF to analyze structural deflections, due to gaps in the speckle application process. Within each area of interest, multiple points of interest must be chosen to assist the analysis program with motion tracking. When post-processing the captured images, the best results were acquired when multiple points of interest were manually selected at each frame of retraction. This allowed the VIC 3-D software to continue tracking selected points after they went out of frame during slat retraction, and then return during the follow-up deployment cycle. As well, rigid body tracking is made possible by selecting speckled points along the lower leading edge of the slat and lower slat cusp. During the full retraction cycle, the slat cusp is assumed to be a rigid body; the overall structural deformation is negligible when compared with the deformation of the adjacent slat cove filler.

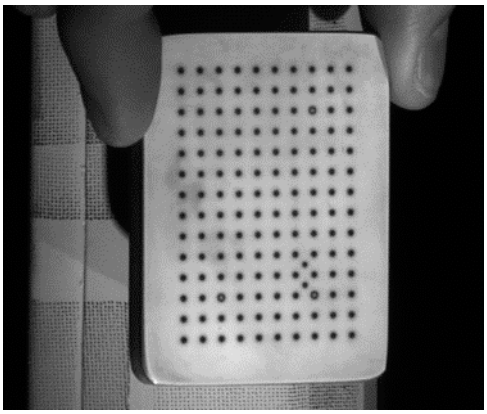

Figure 2.20: DIC calibration image with 3 mm calibration disk (14x10 dot matrix).

2.2.2 Laser Displacement System

Developed both as a validation tool to confirm results from DIC testing and as a more efficient testing alternative, the Laser Displacement System (LDS) uses off-the-shelf electronic components to measure wing geometry during wind tunnel testing. This system is able to track distance using a Keyence IL-600 laser displacement sensor shown in Figure 2.21, and rotation about a fixed axis with a Vishay Rotary Potentiometer. The system is used to scan the lower surface of the SMA SCF wing prototype and measure the outer mold line of the wing during wind tunnel testing. Multiple scans of the wing are taken at multiple retraction configurations during a retraction cycle to determine slat deformation under retraction / deployment, and to compare the SMA SCF geometry with results from DIC testing. This system was developed as a cost-effective, and time saving alternative to DIC testing, with potential applications in other projects. The LDS system in its entirety cost less than the most basic DIC camera / software packages by an order of magnitude, and is able to reduce set-up and testing time significantly requiring only a single calibration to conduct multiple experiments. The following sections will describe the individual instruments used in the LDS and the system design, system calibration and preliminary testing to determine ideal settings, and typical test procedure and data analysis.

2.2.2.1 Instruments and System Design

The LDS relies on two separate electronic systems for data collection to determine the geometry of any tested surface: the Laser displacement sensor, and the rotary potentiometer. This combined system allows for a distance and an angle to be measured with respect to a fixed rotating axis. With the information collected, the position and shape of any measurable surface or object can be measured with respect to the point of rotation.

To determine radial distance from the LDS, a Keyence IL-600 model Laser Displacement Sensor was chosen. The IL-600 boasts variable sampling rate (100, 250, 500, 1000,

Figure 2.21: Keyence IL-600 Laser Displacement Sensor head

3000 Hz), high resolution measurement (0.05 mm) at relatively large distances (200 mm - 1000 mm). The IL-600 laser sensor was originally designed for industrial applications especially in fabrication mills to determine thickness tolerances in sheet metal rolling. Not used in this test, the IL-600 is equipped with a "judgment" zone setting, allowing for communication with lab interface software to alert the program if measured distances lie outside of a predetermined, user-set range. Another feature worth noting is the "zero shift" function on the face of the measurement unit. This feature performs a numeric tare of the current measurement reading, and relating all further measurements made to the new reference point. The sensor is ideal for this research, which requires structural geometry measurements to be collected externally to the wind tunnel test section during tunnel operation.

Sensor position is determined via rotational shaft connected to a Vishay Model 357 Rotary Potentiometer. This sensor unit resolves a change in electric potential (voltage) across a resistive electrical circuit. As the inner shaft is rotated relative to the main sensor body, an output voltage signal varies linearly with rotation angle. The potentiometer is free to rotate with mechanical stops restricting rotational travel to 340°, and is specified to have a 2% maximum variation from linear relationship between rotation angle and output

voltage across the entire angular range.

The LDS consists of a displacement measurement system, the IL-600, connected via rotational shaft to a potentiometer, shown in Figure 2.22. The main shaft supporting the laser system is a threaded 4 mm steel rod allowing for washer and nut, coupling rotation between the laser system and the rotary shaft. The shaft is braced at two points by a bearing block harness to eliminate any out-of-plane rotation. The potentiometer, fixed by a structural support, is connected directly to the threaded rod by a 6 mm to 4 mm shaft coupler, locking the rotation between the laser sensor and potentiometer. The bearing block and potentiometer support are then connected separately to a fixed base. In total, the LDS measures roughly 3" W x 6" H x 16" L, providing a compact and lightweight design allowing for quick installation and test preparation. Rotation of the LDS is controlled via an attached 12" lever arm allowing for smooth, manually controlled rotation of the sensor. During each test measurement, the LDS scanned the wing prototype from the leading edge of the wing, back towards the trailing edge.

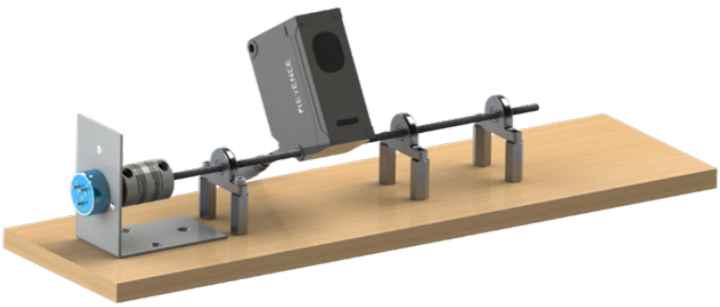

Figure 2.22: SolidWorks model of Laser Displacement System (LDS).

2.2.2.2 Calibration

To ensure accurate measurements received from the LDS, each sensor must be independently calibrated. The IL-600 is pre-calibrated from the manufacturer and is accurate at measurements within 50 mm of any arbitrary zero-shift reference point. However, for measurements made at farther distances from the reference point, or tests requiring a wide range of distance measurements, re-calibration of the system is recommended. For this work, the IL-600 was re-calibrated to be most accurate at ranges between (100 mm to 300 mm) from any declared reference zero-shift position. Calibration was performed by securing the IL-600 head unit to a fixed location, then placing an object with a flat surface facing the head unit at two known distances aligned with the beam emitted from the IL-600. It is important to ensure that the head unit and flat object are placed such that both exposed areas are aligned parallel with each other. This is done to guarantee the emitted beam is perpendicular to the calibration object. To calibrate the IL-600 for experimental testing on the SMA SCF wing prototype, the calibration object was placed at 100 mm and 300 mm away from the zero-shift reference point. This distance range was determined from preliminary measurements to best encompass the full test space for the SMA slat cove filler. Similar measurements methods were used to correlate the system output voltage with the digital data display. Five distinct calibration points were measured at known distances leading to a linear relationship between output voltage and measured distance, shown in Figure 2.23.

The potentiometer was calibrated in a similar manner to the laser displacement sensor. Once the laser had been calibrated and a relationship between output voltage and distance determined, the laser was installed on the LDS. The top surface of the laser displacement sensor provided a flat surface parallel to emitted beam from which to calibrate the potentiometer. The laser sensor was fixed in five different angular positions, with the

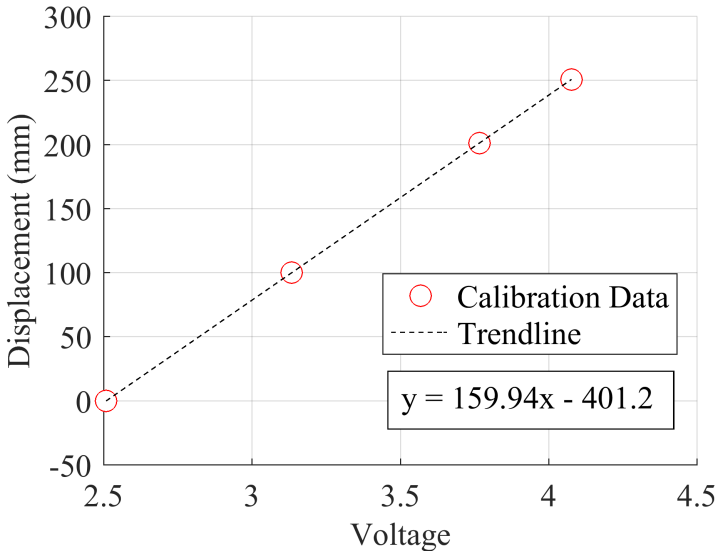

Figure 2.23: Calibration trend-line of Keyence IL-600.

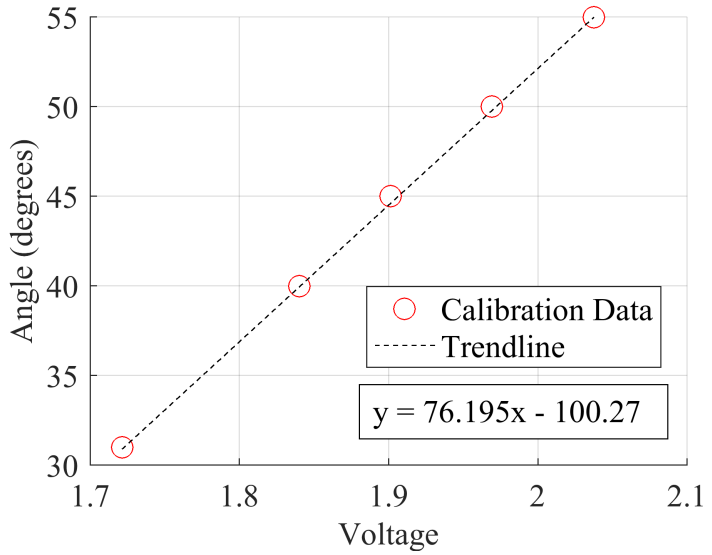

Figure 2.24: Calibration trend-line of rotary potentiometer.

potentiometer output voltage being measured with respect to the angle of incidence of the sensor, and the emitted beam. A linear relationship between the output voltage and

measured angle was determined to be the best fit, shown in Figure 2.24.

2.2.2.3 Testing Procedures

To experimentally determine the outer geometry of the SMA SCF wing prototype, more specifically the SMA slat cove filler, a LDS, previously described, was used. The system couples a distance measurement collected from a laser displacement sensor with a angle measurement describing the orientation of the laser sensor, from which the x-distance and y-distance of the beam from the rotation shaft can be determined. The results output from the LDS system were coordinatized in an inertial reference frame located at the LDS rotation shaft, beneath the test section. Multiple laser "sweeps" taken at various retraction stages can be used to track the deformation of the SMA SCF during a slat retraction cycle and ultimately compared with DIC measurements.

The LDS is installed beneath the wind tunnel test section, in a similar manner to the DIC camera system described previously. However, the DIC and LDS experiments must be conducted separately, as they both use the same installation area beneath the test section. The beam was aligned to pass through a viewing window beneath the wing prototype, allowing for an unobstructed view of the SMA SCF during a full retraction cycle. The LDS was secured to a cantilevered mounting stand with the beam direction aligned with the long axis of the test section, in the upstream direction of the flow. Prior to any testing, the laser displacement sensor must be powered on for 40 minutes prior to testing to warm-up the internal electronics. This is done in accordance with the user manual to prevent measurement drift during long-term experiments. Data was collected for this work at a constant 6° angle of attack with respect to the free-stream flow at multiple stages of slat retraction during a full slat retraction cycle.

Data post-processing was completed using MATLAB to extract collected data from text files and manipulate into a usable form. Initial output distances measured by the IL-

600 needed to be shifted into the proper coordinate system. The beam emitter is offset from the rotational axis of the LDS both along the axis of the beam, and perpendicular to measurement direction. The IL-600 User Manual states that the beam is emitted 29.50 mm away from the rotation axis along the beam direction, and 5.70 mm perpendicular from the beam direction. For this research, the zero shift reference point was set to 500 mm from the emitter face of the laser displacement sensor, requiring distance correction on all collected measurements.

2.2.3 Computational Modeling

A computational model was developed with the previously mentioned experimental testing, with the results of the experimental tests being used to validate further refinement in modeling the SMA SCF. ABAQUS CAE with a UMAT specific to shape memory alloys was used to build and run the computational model. The computational model was developed using dimensions and construction methods matching the wing prototype used for wind tunnel testing to ensure accurate results and validation. Small variations were required to improve model convergence and reduce computational complexity, especially with modeling the hinge connection between the slat and the SMA SCF. The computational model simulated a complete retraction cycle starting from fully deployed, transiting to fully retracted, and back, with structural response information output at each node location. From the full retraction cycle test, data from each retraction stage could be analyzed and compared with experimental test results to improve modeling tools.

2.2.3.1 Model Development

The computational ABAQUS model was developed with model geometry and part interactions matching the experimental wing prototype used in aerodynamic and structural testing. The model consists of a rigid, fixed leading edge of the main wing section, a deformable leading edge slat, and the deformable SMA slat cove filler. Deformation of

the slat and slat cove filler are the only areas of interest in this model. As such, the trailing edge flap will not be considered in the computational model. As well, the main wing is modeled as a rigid, hollow section of the leading quarter-chord. Deformation on the main wing is not of interest, and to reduce complexity and run time, the entire wing will not be considered. Due to symmetry present in the wing prototype, the computational model only considers a half-span section of the wing/slat with pinned connections at both span-wise extents. This is mirrored in the wing prototype construction where the slat is divided into two main sections, pinned at each span-wise extent, and connected through a pin-track system at the mid-span. Shown in Figure 2.25 is the half-span wing prototype section modeled in ABAQUS CAE.

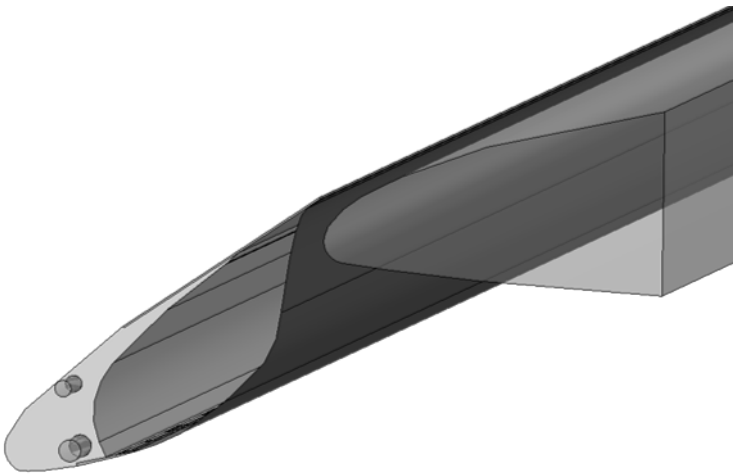

Figure 2.25: Side view of FEA model of SMA SCF wing.

Apart from simplifications in modeling (rigid main wing, non-inclusion of flaps), the hinge connection between the SMA SCF and the slat was designed to be kinematically similar, but not an exact model of the constructed wing prototype. To allow for accurate hinge modeling, the lower edge of the SMA SCF is kinematically fixed to the inner, lower

cusp of the slat. The motion between the two parts is constrained to only allow rotation along the span in the reference or undeformed coordinate system, keeping the SCF fixed to the deformable slat but allowing rotation as the slat retracts. The experimental prototype instead uses a thin metal/adhesive membrane to connect the SCF to the leading edge slat. In both models however, the hinge axis along the slat is initially positioned in the same location. Previous iterations showed that when considering a continuous, rigid hinge down the entire span-wise axis of the slat produced incorrect results when compared with experimental results. The rigid, continuous hinge design remained parallel to the undeformed slat axis, while during retraction, the slat and slat cove filler deflected upwards parabolically with a maximum deflection at the quarter-span. The resulting model allowed the rigid hinge to travel through the lower cusp of the slat, leading to very incorrect results. In addition, friction between contacting surfaces is present to best model the sliding action of the SMA SCF on the main wing, and SMA SCF on the inner surface of the slat during retraction. The SMA material assignment used in describing the SCF in the computational model was created using the Souza-Aurucchio model to accurately predict the structural response of the shape memory alloy SCF [24].

To accurately test the SMA SCF computational model, and to be of good comparison with experimental test results, the slat must undergo similar actions during modeled retraction as in experimental tests. When the 3-D CAD model of the wing prototype was being designed and developed, the previous computation model was used as the template. Work completed by Scholten et al. designed the slat retraction path to consist of a single rotation point by which the entire slat would rotate around. Thus, a single reference point can define the rigid body motion by which the slat retracts and deploys [25]. The computational model developed for this work and the experimental wing prototype are both based on the previously developed 2-D computational model, and both share a single point rigid body rotation which defines the slat retraction path. The computational model is able to track

the structural response of the SMA-based slat cove filler along the entire retraction cycle path, with important data being selected from each 10% retraction stage.

2.2.3.2 Model Analysis and Comparison

While the computational model calculates the full-field structural response of the SMA-based SCF model, notable comparisons are only made with data collected during experimental testing. Experiments conducted on the physical wing prototype collected deflection data along the trailing edge of the slat at each retraction stage, and deformation data in both 2-D along a chord slice, and in 3-D over the entire speckled area collected through DIC testing. Experiments conducted using the LDS were able to collect SCF coordinates during retraction and are used to reinforce data collected during DIC testing. Similarly, results from the computational model will be used to predict the trailing edge tip deflection and the response of the SMA SCF during a full retraction cycle along the same selected 2-D chord slide. It is important to note that the entire cycle must be considered as the retraction response differs greatly from the deployment response. This will be discussed further in the following results section.

2.3 Closing

To fully characterize the performances changes due to the addition of an SMA-based slat cove filler, a wing prototype was constructed and tested. To determine the aerodynamic influence, the wing was tested at a variety of conditions and configurations using the Texas A&M 3'×4' low speed wind tunnel. Each high lift device configuration and retraction percentage was pitched at constant free-stream velocity to measure the change in total wing lift across a wide range of angles of attack. For this work however, the angle range of most interest lies between 4° and 8° angle of attack; this is the pitch range the slat cover filler will operate in when an aircraft is flying in during the takeoff, approach, and landing phases of flight. This test method was conducted for each aerodynamic configuration

for both consistent test procedural methods, and to ensure precise comparison between different slat configurations.

To determine the structural response of an SMA-based slat cove filler, the wing prototype was experimentally tested using digital image correlation methods, and a custom-designed laser displacement system to determine structural deflections. DIC and laser sensor testing were conducted separately under the same test conditions (i.e. 6° angle of attack, retraction percentages) to ensure result comparability. Co-developed with experimental testing, a finite element analysis model was constructed and validated using information gathered during experiments of the SMA SCF wing. Through multiple testing methods, a characterization can be made of both the aerodynamic performance and structural response of an SMA-based slat cove filler in a wind tunnel environment.

3. RESULTS AND DISCUSSIONS

3.1 Opening Statement

This section details the experimental and computational results obtained. Results will be separated into two main sections, one presenting and discussing the aerodynamic effects of an SMA-based slat cove filler, and the other regarding the structural response. Preliminary testing to characterize testing methods will be briefly presented, with results being used to support fundamental bases for experimental methods. The results from each testing method will be compared with supporting experiments, and determinations will be made to provide useful information on the testing applications for each method. The ultimate goal for this research is to fully characterize an SMA-based SCF using proven experimental methods, from which one can validate co-developed computational modeling tools.

3.2 Aerodynamic Results

The aerodynamic characteristics of an SMA-based slat cove filler were determined from testing methods described previously in the Section 2.1.7 of the Methods section. Primary aerodynamic results were formed using data collected during wind tunnel testing in the Texas A&M 3'$\times$4' low speed wind tunnel. The wind tunnel facility provided an excellent experimental test-bed from which to collect results which were both repeatable, and consistent with fundamental aerodynamic theory. Two main preliminary tests were completed to determine the flow quality experienced in the test section, and to compare well-tested aerodynamic configurations with historical results. The performance of an SMA SCF was compared to a reference high lift device configuration, providing a base-line measurement tool. Results presented in this section will be shown in typical standardized formats: lift curve slope, drag polar, pressure curves.

3.2.1 Preliminary Testing

Without proper instructional guides, or laboratory technicians to advise in wind tunnel testing procedures, multiple preliminary tests were conducted to realize the potential of the 3'×4' wind tunnel. To develop and archive a consistent knowledge base, two separate tests were conducted to characterize the wind tunnel facility and to determine repeatability of testing data.

The first test used simple flow visualization techniques to qualitatively determine the flow conditions inside the test section during tunnel operation, and to identify problematic areas of aerodynamic influence. Cotton string tufts, secured to the surface of the SMA SCF wing prototype, allowed for flow field visualization during wind tunnel testing. This simple technique, while classical, allowed for inexpensive and temporary visualization treatments to be applied to the wing surface. Tufted strings were first considered in place of more common smoke-wand flow visualization testing. The use of a smoke-wand in closed loop wind tunnel testing would leave a thin residual film on all surfaces, as well residual smoke would remain in the flow loop well after testing cessation. Black cotton strings were cut to roughly 2" in length, and frayed halfway through each length to spread the tuft strings on the free end, while remaining tightly coiled at the end to be secured to the wing skin. Tufted strings were attached to the surface, at a grid spacing of 4" maximum on the surface of the main wing, leading edge slat, and trailing edge slat, using transparent adhesive film to secure the coiled end of the tuft. The SMA SCF wing prototype was tested in the 3x4 wind tunnel at multiple angles of attack and two high lift device retraction configurations. For preliminary tuft testing, the untreated slat was used.

Figure 3.1 is a still frame image from a flow visualization test conducted at 15.0 m/s across a wide range of angles of attack (-4° to 12°). Note the blurred tuft strands becoming more frequent the further aft of the wing that they are placed. The blurred tuft effect is

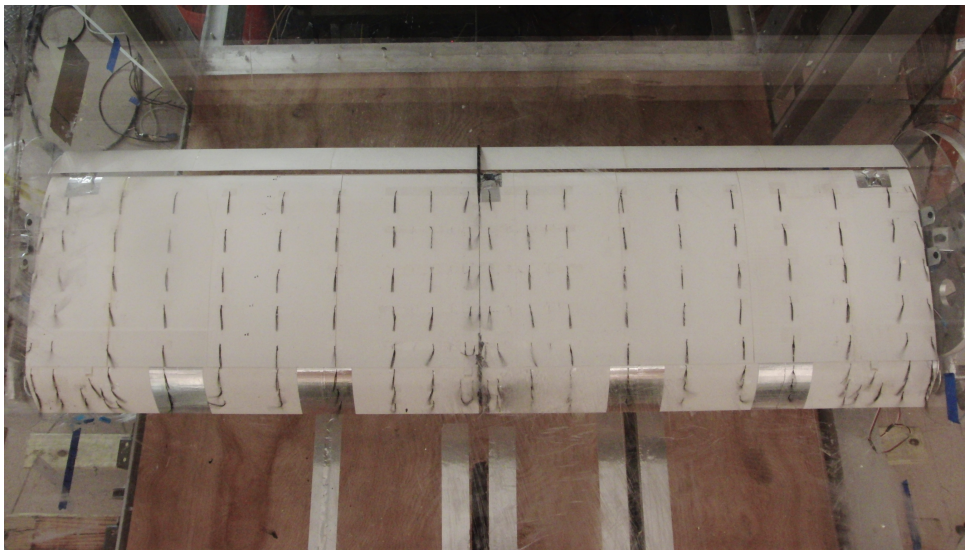

Figure 3.1: SMA SCF wing with attached tufted strings during 15.0 m/s flow visualization test

caused by unsteadiness in the flow at that point along the wing. From observations made, it was determined that the blurred, vibrating tufted string indicated flow separation from the surface of the wing at that location. In general, across multiple test configurations, it was noted that overall flow direction was parallel with the ideal flow characteristics of the wind tunnel. Minimal sidewall effects were visualized only extending <6 cm in from the test section wall, and were only present along the trailing edge and at high angles of attack (>8°). Of note and concern is the flow separation regions caused by the presence of the leading edge actuator ports. It was found that covering the ports with smooth adhesive backed aluminum strips greatly reduced unsteady flow conditions downstream of the ports. However, this method proved unfeasible for wind tunnel tests spanning multiple retraction configurations.

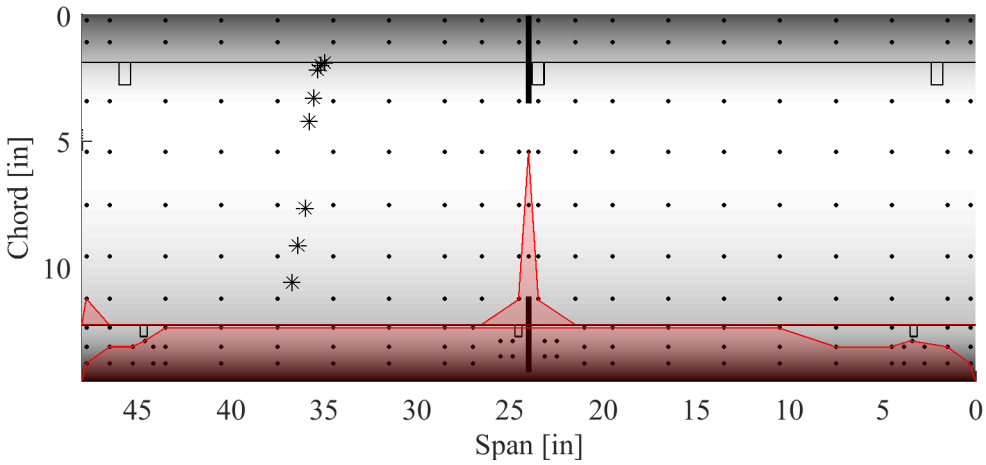

(a) Flow visualization analysis, tufted wing at 0° angle of attack

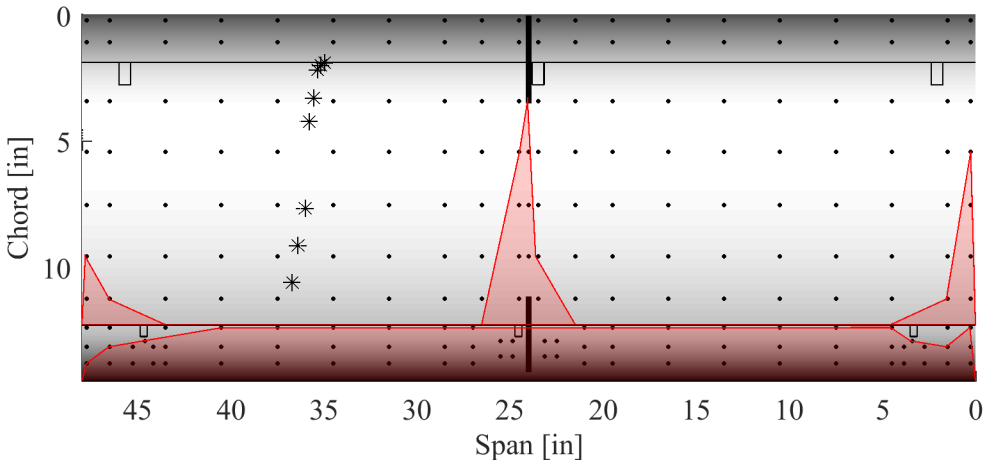

(b) Flow visualization analysis, tufted wing at 6° angle of attack

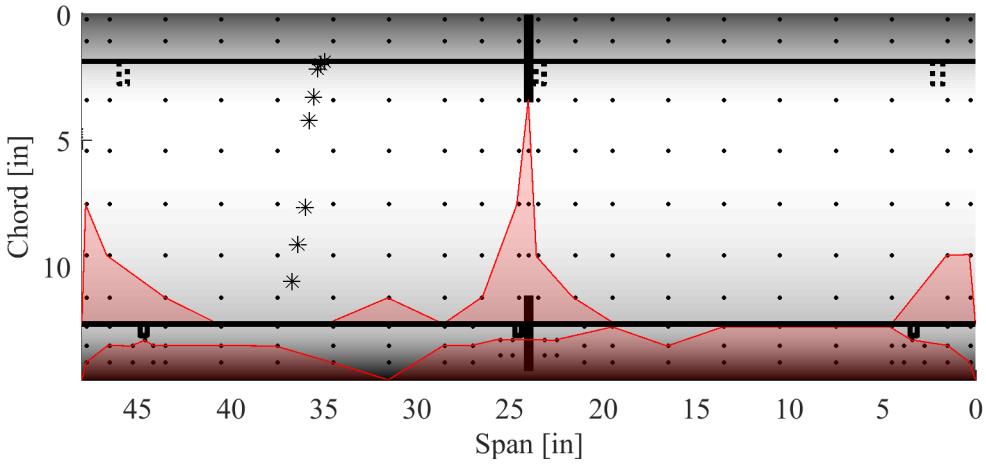

(c) Flow visualization analysis, tufted wing at 9° angle of attack

Figure 3.2: Flow visualization at multiple angles of attack

Multiple methods of recording separation on the wing were tested, from video recording, still-frame photography, but the most consistent collection method was recording by hand, the location of separation. This recorded data was then analyzed after the test and plotted using a MATLAB script to show the line of separation on the wing. From this separation line, the flow conditions over the wing could be analyzed at multiple angles of attack, and with multiple high lift device configurations (retracted, deployed). Shown in Figure 3.2, results from flow visualization experiments are shown with the line of separation overlaying the wing planform area. Note how as the angle of attack increases in each image, the line of separation moves further upstream. From this test, it was determined that the current wind tunnel set-up was unable to capture the onset of stall of the fully deployed wing. Even at 15° angle of attack, the flow remained attached over most of the wing.

The second characterization experiment will not be discussed in great detail, and can be found attached in Appendix A. To ensure the quality of any data collection system, and to better understand the performance of the 3x4 low speed wind tunnel, a test was conducted using a common historical airfoil shape. A fiberglass wing section of a NACA 0012 airfoil was used to characterize the flow conditions of the 3x4 wind tunnel, and allow for familiarization of the Scanivalve scanning pressure sensor. The NACA 0012 airfoil section has been extensively studied for decades and has a library of recorded aerodynamic data describing its performance under flow. A wind tunnel test was conducted at multiple free-stream velocities and at multiple angles of attack to validate wind tunnel operating performance and confirm factory calibration for the Scanivalve pressure scanner. This validation testing was conducted by Gregory Methon of the ENISE school in Saint-Etienne, France as a portion of his international placement at Texas A& University.

3.2.2 Reference Configuration

To characterize the aerodynamic performance of an SMA-based slat cove filler, a comparison must be made to a similar wing configuration to determine any potential detriments and improvements. This research utilized an untreated slat, (i.e., without an installed SMA SCF) to act as a reference airfoil shape on which to compare results. The untreated slat was rigorously tested across a wide spectrum of test conditions and configurations to determine a baseline on which to determine SCF performance: angles of attack varying from -4° to 12°, multiple high lift device retraction configurations, and at two free-stream velocities.

(a) Fully Deployed Configuration; untreated

(b) Fully Retracted Configuration; treated

(c) Fully Deployed Configuration; treated

Figure 3.3: SMA SCF wing configurations

Shown in Figure 3.3, the fully retracted, untreated slat configuration represents the SMA SCF in the general cruise flight condition. The slat cove filler is only designed for the takeoff, approach, and landing phases of flight and will not be deployed during cruise. Tested only at low Reynolds flows (< 300,000), it is unknown how the SMA SCF will perform at much higher cruise speeds. For all following figures showing coefficient of lift,

drag of any airfoil configuration, the author would like to clarify that this is presenting the total coefficient of lift, or wing coefficient of lift, not the airfoil section lift coefficient.

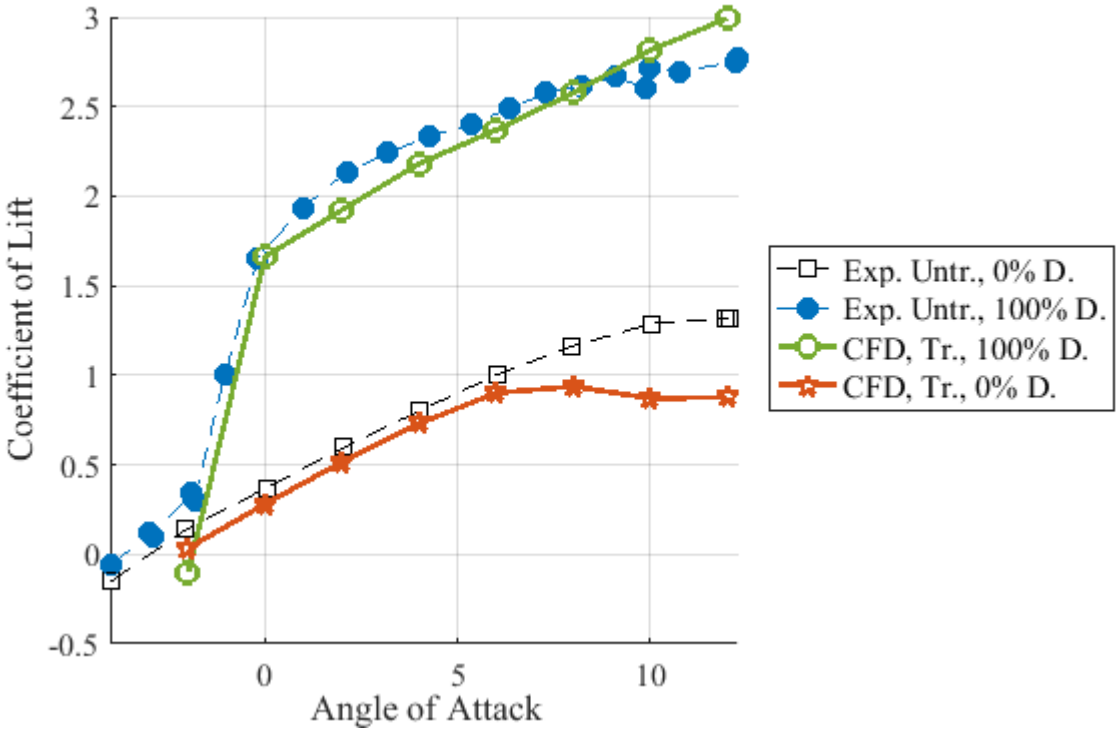

Figure 3.4: Lift curve slope comparing fully deployed, untreated high lift device configuration with fully retracted, untreated configuration

Figure 3.4 describes the aerodynamic performance of the untreated slat tested at 15 m/s at multiple angles of attack. The lift performance of the retracted configuration is linear with respect to change in angle of attack and begins to show a plateau in the lift curve at angles greater than 9°. The fully deployed high lift device wing configuration increases the lift performance over the retracted configuration substantially at angles of attack greater than -1°. The two high lift devices perform different functions in improving the aerodynamic performance of the wing prototype. The leading edge slat acts to reduce

the incident angle of attack of the airfoil with respect to the flow, improving the stall characteristics at high angles of attack, but at the cost of reducing lift at lower angles. The trailing edge flap increases the incident angle of attack at low angles, but lowers the angle of attack at stall from the retracted configuration. When deployed simultaneously, the slat and flap act to improve the lift characteristics of the airfoil across a wide range of angles of attack. Note the high-slope linear lift region for fully deployed at angles of attack (-2° to 2°). This rapid change in lift is due to flow attaching to the lower surface of the wing as the angle increases. At low angles of attack the flow is separated from the lower surface by the drooping leading edge slat.

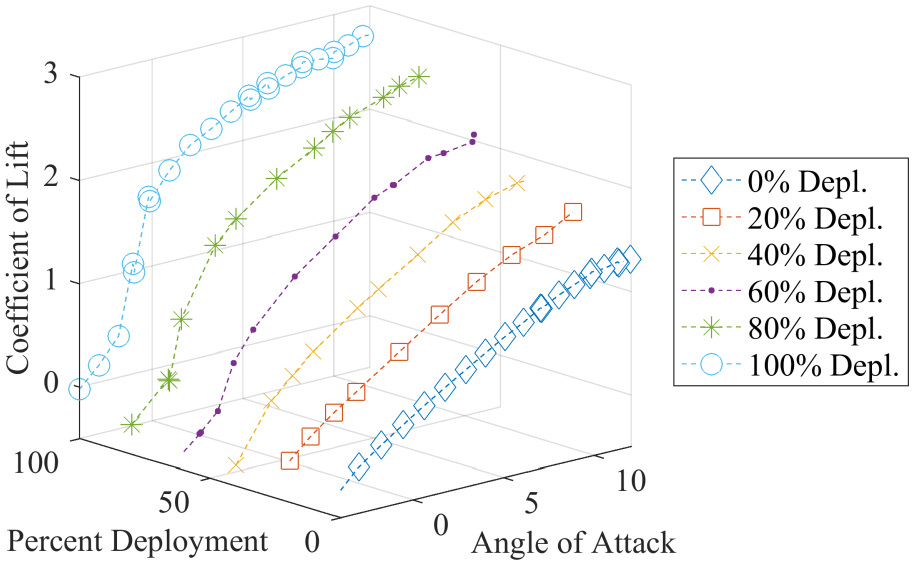

Figure 3.5: Surface plot of the untreated slat configuration wing prototype when compared with retraction percentage

The reference slat configuration was tested at multiple stages of retraction to measure the effects of the high lift device position on aerodynamic performance. In Figures 3.5 and 3.6, multiple lift-curve-slopes are plotted with respect to changing retraction percentage.

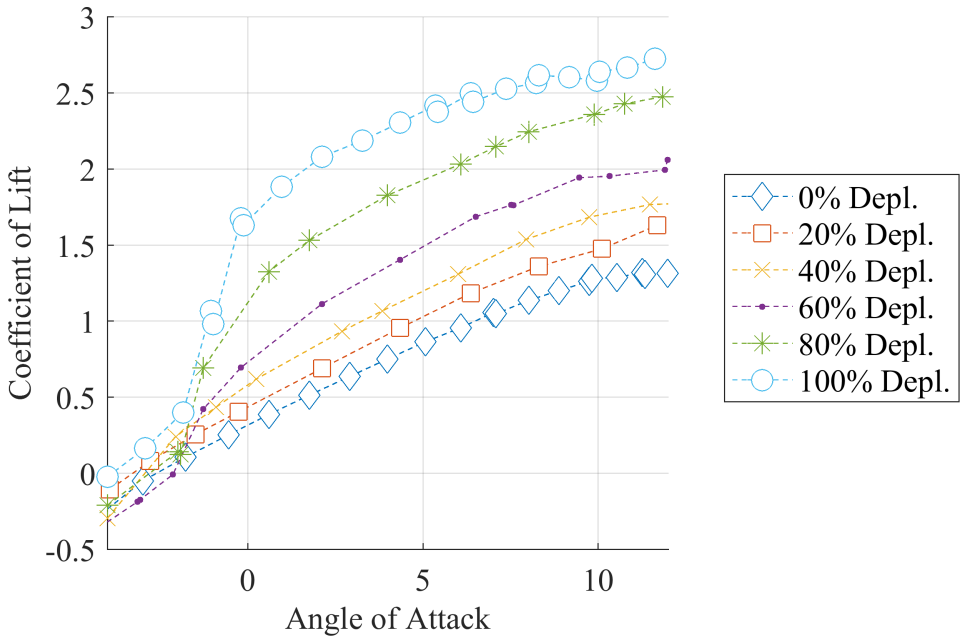

Figure 3.6: Lift curve slope of SMA SCF wing prototype

This figure shows the performance surface of the wing prototype and how the lift-curve-slopes are changing. Note how the multi-linear lift regions present at full deployment transitions to a single linear region at as the high lift devices retract. This experiment was performed in separate wind tunnel tests, each test collecting aerodynamic load data during angle of attack sweeps. For reference, each percent deployment corresponds to how far each high lift device has traveled with respect to the entire retraction arc. For instance, at 30% deployment, both the slat and flap have been deployed 30% from the fully retracted state. Typical flap and slat operations on a flight vehicle are not referenced in this manner. Flap and slat deflections are often given as percent down or degrees down. However, for the present research program, each high lift device configuration is referred to in terms of percent deployment. During all tests, the slats and flaps are actuated at the same increment simultaneously; no tests were conducted with either slats or flaps actuated individually.

The final method by which the aerodynamic reference state of the untreated wing prototype characterization was through pressure measurements collected during wind tunnel testing. The Scanivalve pressure scanner measured static pressure from surface mounted ports over the surface of the main wing, allowing for a pressure distribution to be determined. This pressure distribution can be integrated to determine the lift acting on the surface of the main wing. This data however is not able to be compared directly with lift collected through the ATI load cells. A limited number of ports were installed on the main wing, providing low resolution data, and pressure ports were unable to be installed in the slat and flaps. Figures 3.7, 3.8 show the pressure distribution plotted over the normalized chord length of the wing at multiple angles of attack, with the top and bottom of the wing representing the top and bottom curves shown in the C_P figures. The referenced chord length is with respect to the retraction high lift device configuration. The pressure distributions follow the same trend as the lift curve slope, with the lowest overall lift at low angles of attack, rising to a peak at 12° angle of attack. It is important to note that the stall condition of the untreated wing prototype has not been investigated, but lies beyond the test range of (-4° to 12° angles of attack).

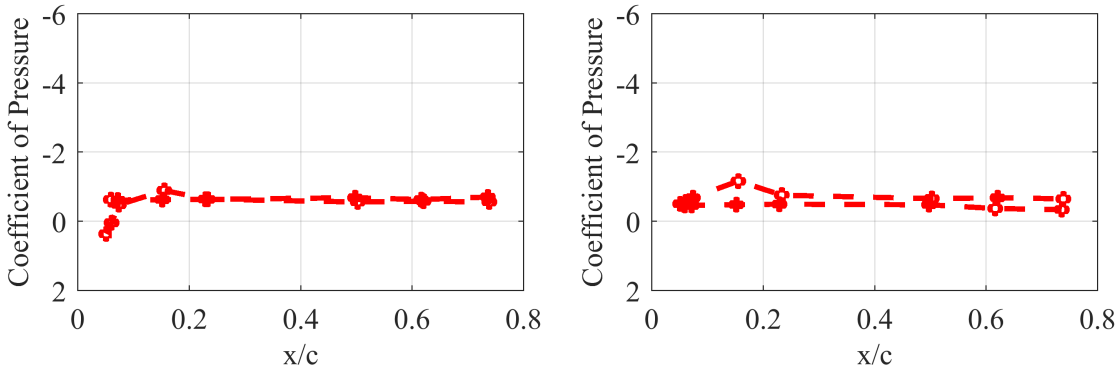

(a) -4° angle of attack

(b) -2° angle of attack

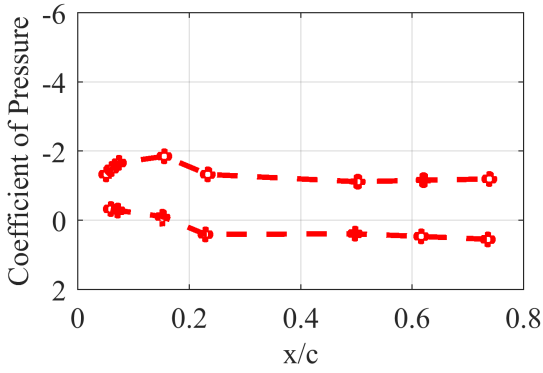

(c) 0° angle of attack

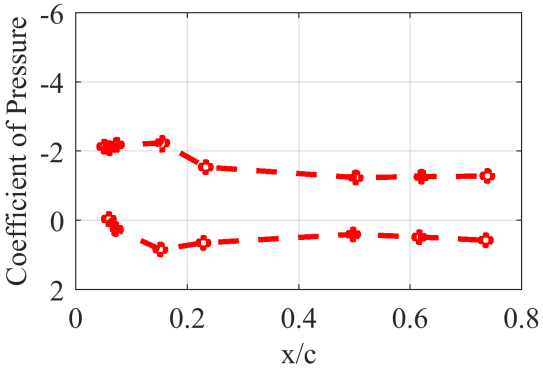

(d) 2° angle of attack

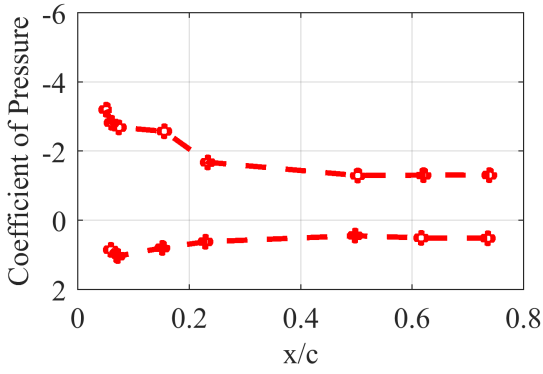

(e) 4° angle of attack

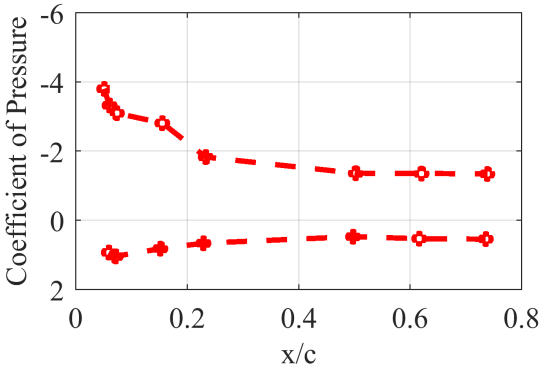

(f) 6° angle of attack

Figure 3.7: Pressure distribution over main wing of untreated high lift device configuration at multiple angles of attack.

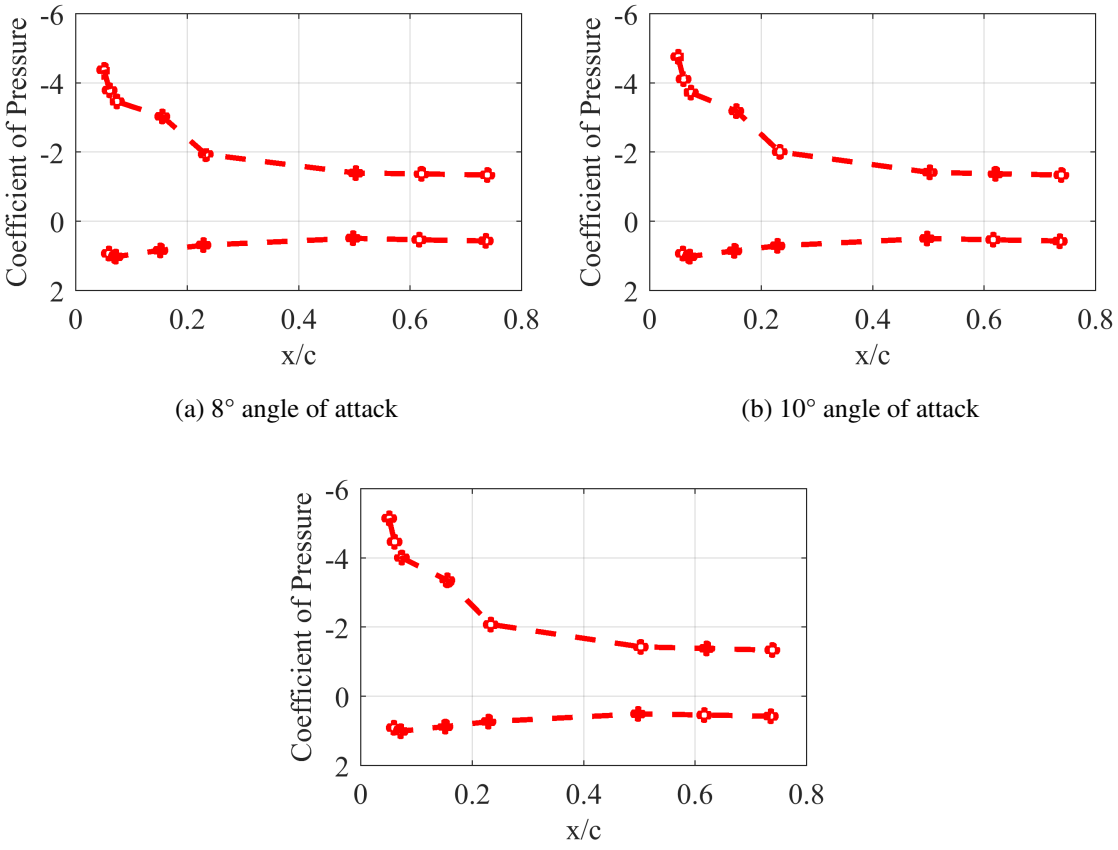

(a) 8° angle of attack

(b) 10° angle of attack

(c) 12° angle of attack

Figure 3.8: Pressure distribution over main wing of untreated high lift device configuration at multiple angles of attack. see Figure 3.7

3.2.3 SMA SCF Wing Prototype Performance

With the baseline wing performance established from the untreated, reference configurations, the change in performance due to the addition of the SMA SCF can be determined. The SMA SCF wing prototype was tested under the same conditions as the untreated configuration to be able to make a comparable judgment on the improvement caused by the addition of the SMA slat cove filler. Each test was conducted at a steady 13° C, 15 m/s across a variable range of angles of attack. To ensure the SMA remained securely bonded to the slat during wind tunnel testing and to reduce any potential bond fatigue, the test matrix was reduced by eliminating test configurations at intermediate stages of retraction, when the SCF underwent the most stress. Aerodynamic results were collected in the fully deployed high lift device configuration, and during DIC wind-on testing when the high lift devices underwent a full retraction cycle at a constant angle of attack. Multiple, independent tests were conducted over several days to ensure all data collected is repeatable.

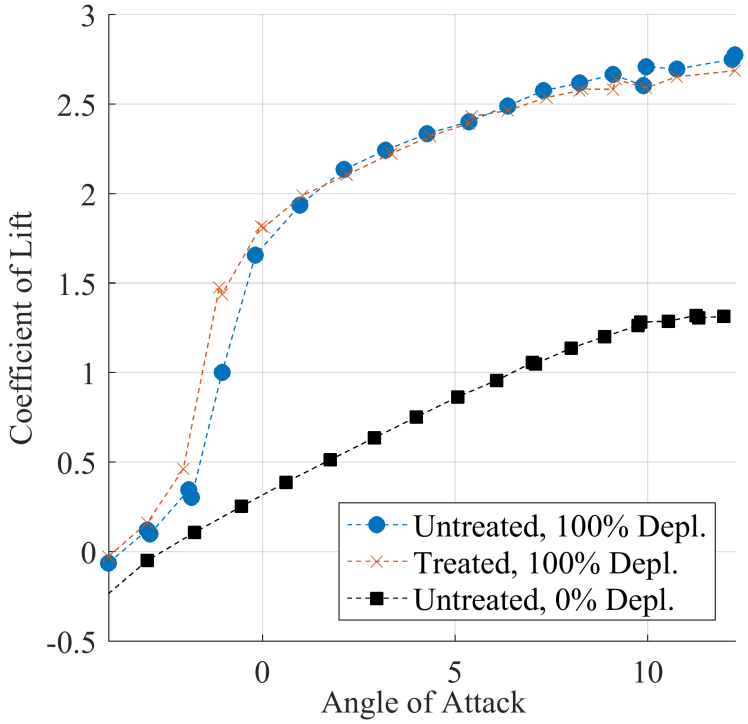

Figure 3.9: Lift comparison between untreated (no SCF) and treated (SCF) slat configurations.

In Figure 3.9, a comparison of the lift-curve slopes between slat configurations is shown. The lift curve slope for the untreated, 100% retraction high lift device configuration is shown, in black, for baseline reference. The treated slat configuration (shown in red) matches well with the untreated slat, shown in blue, both at 0% high lift device retraction. The addition of the SMA-based SCF increases the lift at lower angles of attack (<1°), while it slightly reduces lift at angles greater than 6°. In the angle range of most interest, between 4° and 8° angles of attack, the SMA SCF slat configuration differs in overall lift by an average of 1.0%.

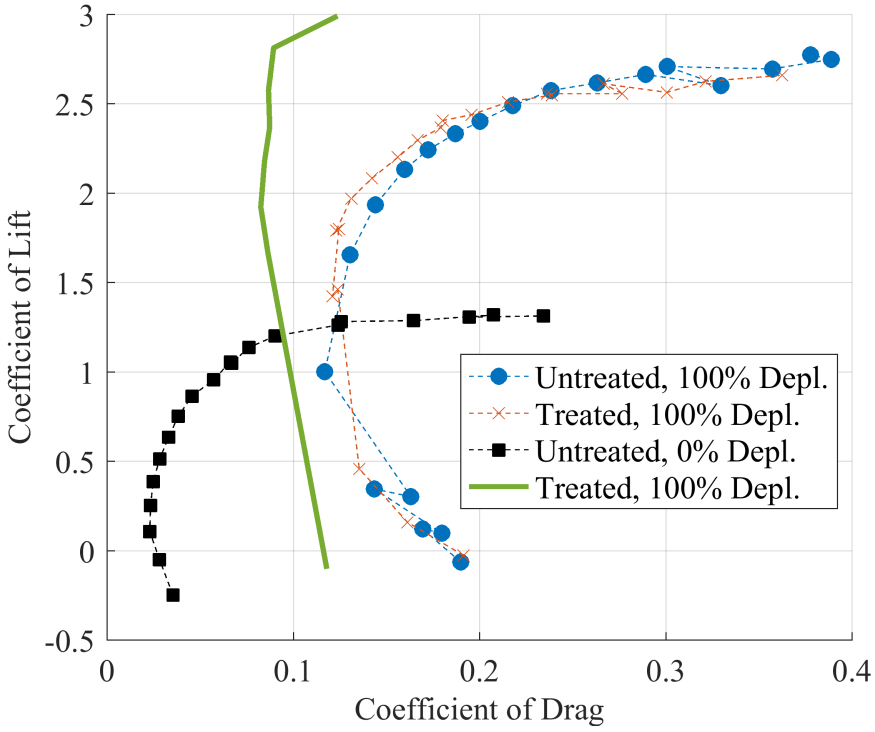

Figure 3.10: Drag comparison between untreated (no SCF) and treated (SCF) slat configurations.

Figure 3.10 compares the performance of the treated and untreated configurations though a drag polar. As shown previously in 3.9, the lift does not vary significantly between slat configurations. However at high levels of section lift (c_l = 1.5 - 2.5), there is a drastic reduction in section drag, averaging a 7% reduction over the entire range, with a maximum percent difference of 12% at a c_l of 2.0. The addition of the slat cove filler greatly improves the drag characteristics of the wing prototype in the pitch range of importance for this research (4° to 8°), which is typical for the approach, and landing phases of flight. Shown in both Lift and Drag Polar figures are results from a computational fluid dynamics program, for which this data is being used to validate.

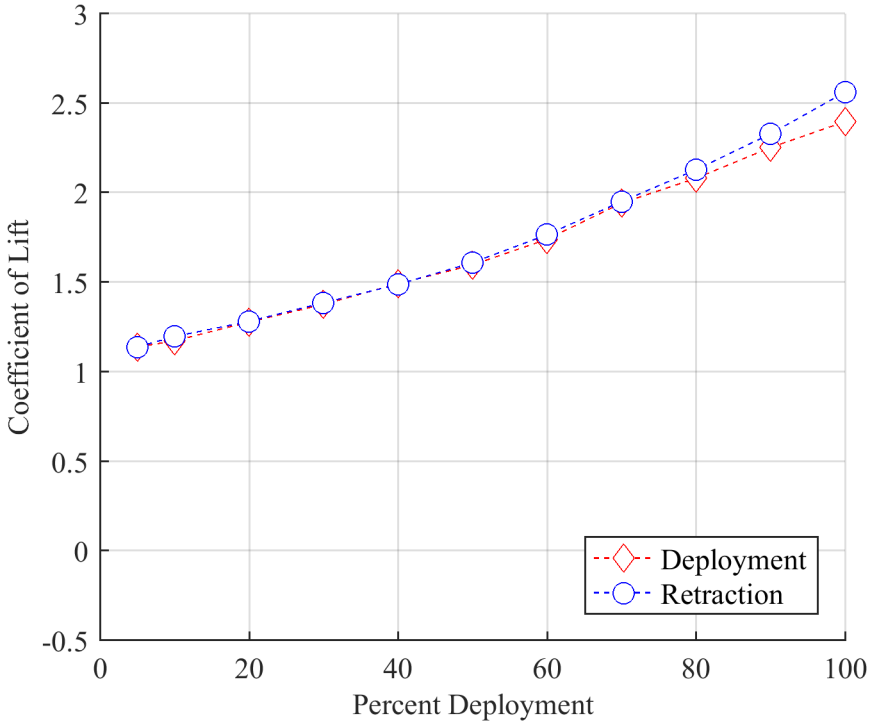

Figure 3.11: Slat retraction effects with respect to coefficient of lift.

Pitching moment, which has yet to be explored computationally, was collected using the ATI F/T load cells simultaneously with Lift and Drag forces. Shown in Figure 3.12, the pitching moment comparison between treated and untreated configurations. The pitching moment is measured from the load cell mounting point, roughly 2 cm forward of the center of gravity of the deployed wing. In both instances, the wing prototype exhibits negative stability across the full pitch range, peaking at 0° angle of attack. The treated condition however, has a reduced negative stability forward of the low peak, angles greater than 0° .

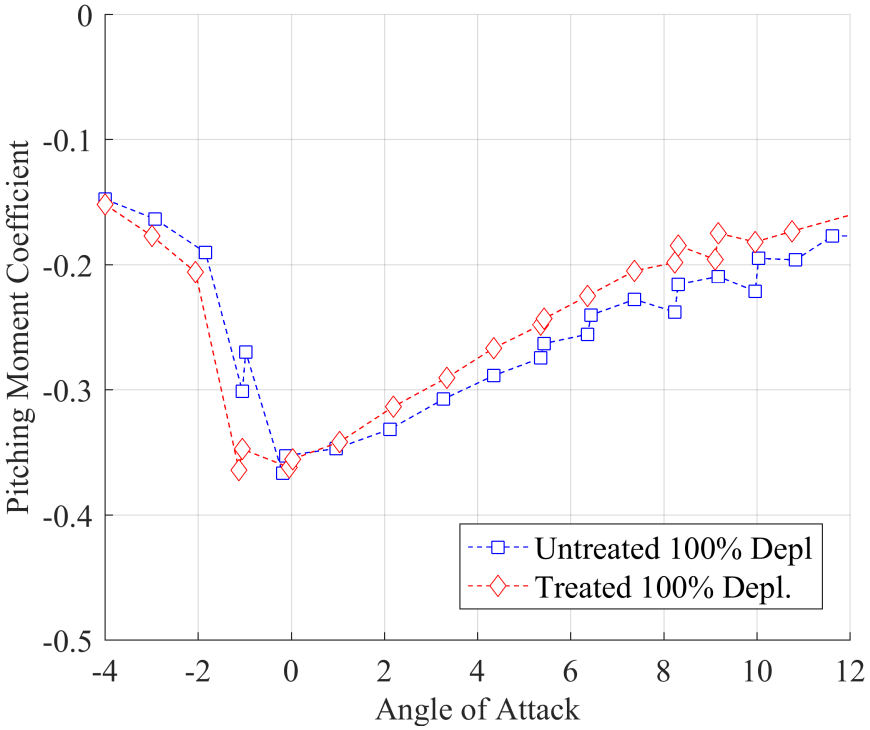

Figure 3.12: Slat retraction effects with respect to pitching moment coefficient.

Aerodynamic data was also collected during DIC wind-on experiments, where the wing angle of attack was held constant at 6° and the high lift devices underwent a full retraction cycle. Figure 3.11 visualizes the change in lift as the high lift devices are retracted then deployed. Aerodynamic data was collected at each 10% deployment interval with 100% deployment corresponding to fully deployed slats and flaps. The slight hysteresis response shown when the deployment and retraction arcs diverge at the fully deployed condition is thought to be caused by the data averaging procedure not fully removing data variations. The retraction/deployment arcs are shown in Figure 3.13 from a three-dimensional perspective of how lift changes with respect to angle of attack and deployment percentage. For reference, the fully retracted untreated wing configuration is also plotted.

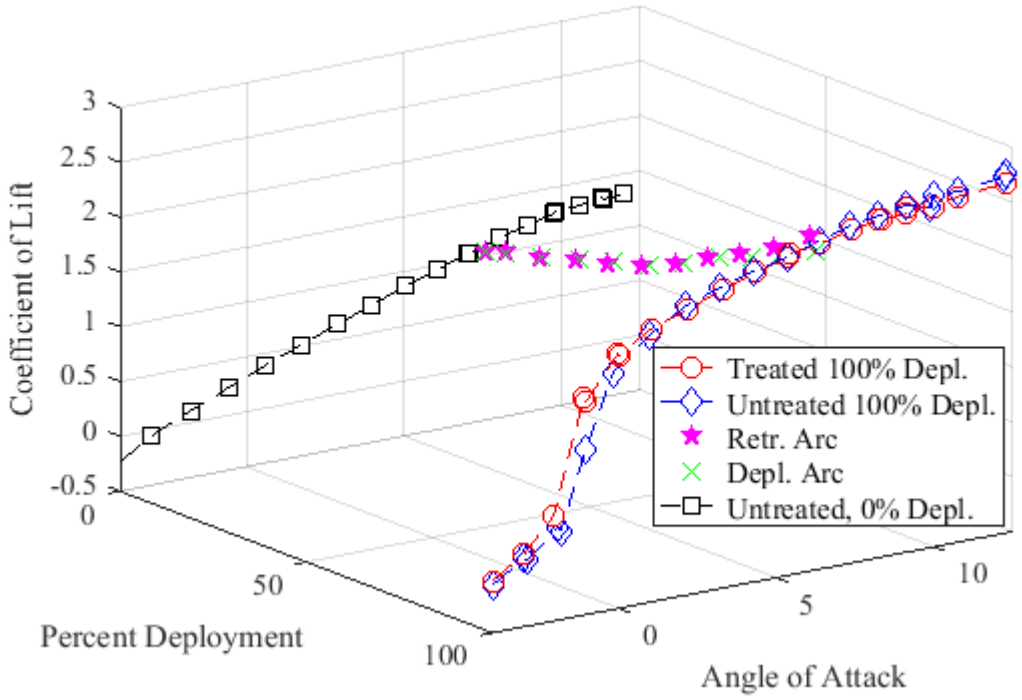

Figure 3.13: Surface plot showing retraction arcs connecting the fully deployed and fully retracted lift-curve-slopes.

Aerodynamic efficiency can be captured through relating the ratio of Lift to Drag between slat configurations. As shown in Figure 3.14, across the entire range of angles of attack, the aerodynamic efficiency of the wing is improved. This demonstrates clearly that the addition of the SMA-based SCF improves the aerodynamic performance of the CRM-based wing prototype. The final comparison between untreated and treated slat configurations can be made between pressure data collected by the Scanivalve pressure scanner during wind tunnel tests. Figure 3.15 compares the treated and untreated pressure distributions over the main wing section. For the sake of brevity, and to show results at a view-able scale, pressure comparisons are limited to two angles of attack of most interest. Shown in (a), the treated configuration outperforms the untreated configuration; with the

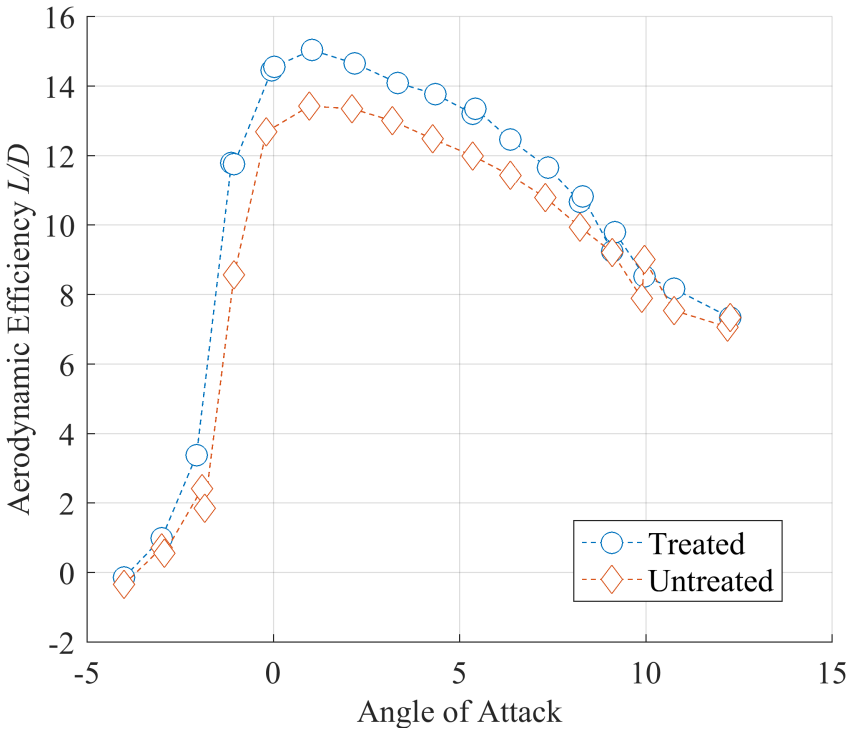

Figure 3.14: Aerodynamic efficiency comparison between treated and untreated wing configurations.

addition of the SMA SCF increasing the leading edge pressure spike. In (b), the untreated configuration surpasses the treated configuration, mirroring results shown previously. In both cases, the pressure distribution over the main wing matches over the great majority of the wing, with the only differences being near the slat treatment influence area.

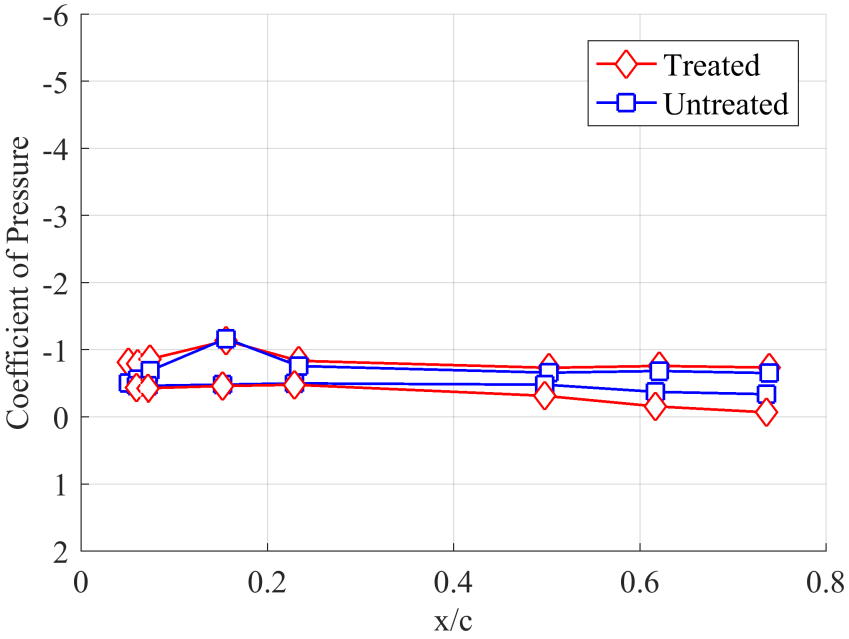

(a) -2° Angle of Attack

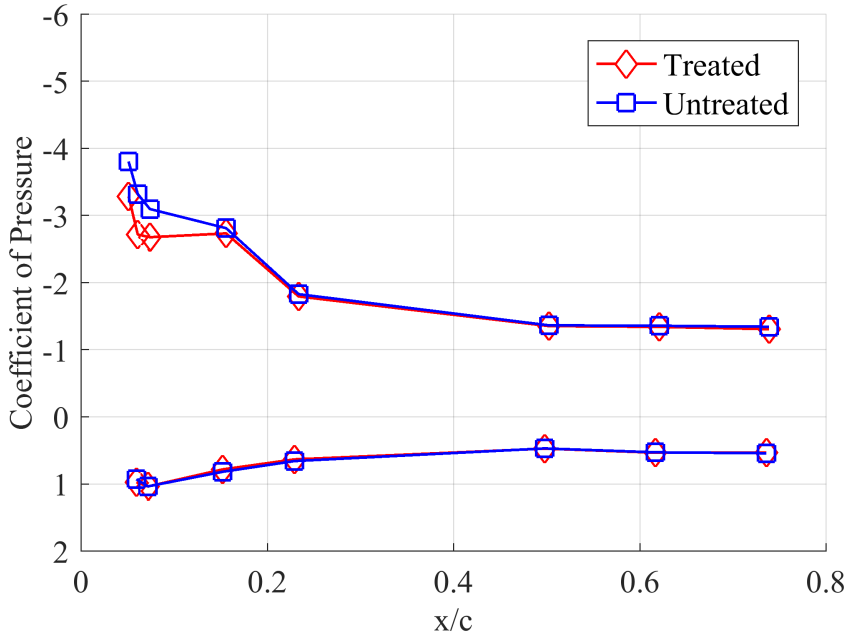

(b) 6° Angle of Attack

Figure 3.15: Pressure distribution comparison between treated and untreated slat configurations at -2° and 6° angles of attack.

3.3 Structural Testing

To determine the structural response of an SMA-based SCF during wind tunnel testing, the wing prototype was non-intrusively tested with experimental results being used to validate a co-developed computational modeling tool. Experiments were conducted in two phases: wind-on and wind-off testing. For model validation, only wind-off results were considered, as the computational model does not account for forces from aerodynamic effects. Conducted experiments comprise of digital image correlation (DIC) testing, displacement tests using the developed laser displacement system (LDS), and tip deflection measurements collected during wind-off retraction cycling. Experimental data was used to correlate results from computational modeling, and to improve upon existing modeling tools for future development use. Results from experiments conducted during wind tunnel operation by the DIC system to determine structural response under aerodynamic loading will then be discussed. Results presented from the LDS, DIC, and FEA analysis will be compared from a common inertial coordinate system, aligned with the rotation axis of the LDS. From this fixed reference frame, each methodology is able to be compared during each stage of slat deployment.

3.3.1 Digital Image Correlation

Digital Image Correlation (DIC) is a non-intrusive, optical, full-field structural response measurement tool used to determine how a structure deforms and changes position during loading and rigid body motion. Previously described methods were used to prepare the wing prototype for, and to conduct static experiments on the SMA-based SCF during slat retraction under atmospheric conditions and operating wind tunnel conditions. The results from the wind-off testing, are used to compare with other experimental methods, as well as to validate the co-developed computational FEA model of a the SMA SCF. Wind tunnel test results, denoted wind-on, was compared with wind-off results to determine

how the structural response of an SMA-based SCF during a retraction cycle changes when exposed to aerodynamic loads.

As previously described in the experimental methods section detailing the use of DIC in testing the slat cove filler, DIC experiments were conducted at a constant 6° angle of attack. During the test, the slat underwent a full retraction cycle in which the slat was retracted at 10% intervals until it reached the fully retracted state, then deployed back at the same interval. At each retraction interval, the DIC system captured images of the leading edge slat and slat cove filler from beneath the test section. The first image captured for each test, designated as the 100% deployment state, is defined as the reference image from which VIC 3-D is able to resolve motion and deformation.

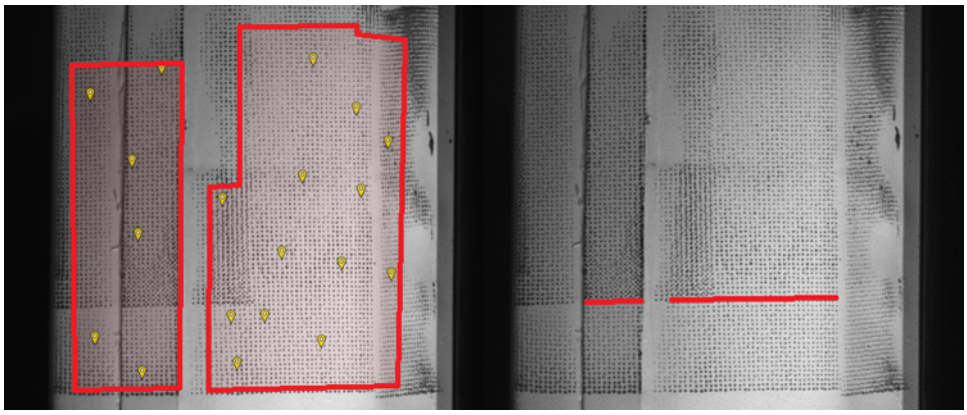

(a) Area of Interest (b) Line of Interest

Figure 3.16: DIC Analysis area selections.

Due to how the speckle pattern was applied to the lower surface of the slat, there are four main areas of interest from which the DIC system resolved structural response. Figure 3.16 shows the reference image for the wind-off DIC experiment, with four areas of interest, and the line of interest used to select areas for analysis. Note the yellow specified

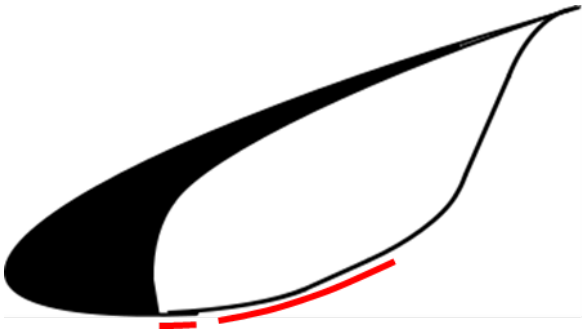

Figure 3.17: Side view of treated slat with 2-D DIC reference line beneath speckle area.

points. Points of interest are chosen by the user to assist the DIC computation software in resolving full-field structural results and motion. This was especially useful in this effort as the SMA SCF retracts behind the main wing, removing all SCF speckle points from the captured image. When the slat deploys out from behind the main wing, these points are used to ensure the VIC 3-D software recognizes the correct geometry. With the areas and points of interest chosen, the VIC 3-D software analyzes each collected image frame and compares speckle orientations and skews to determine rigid body motion and deformation of the SMA SCF slat.

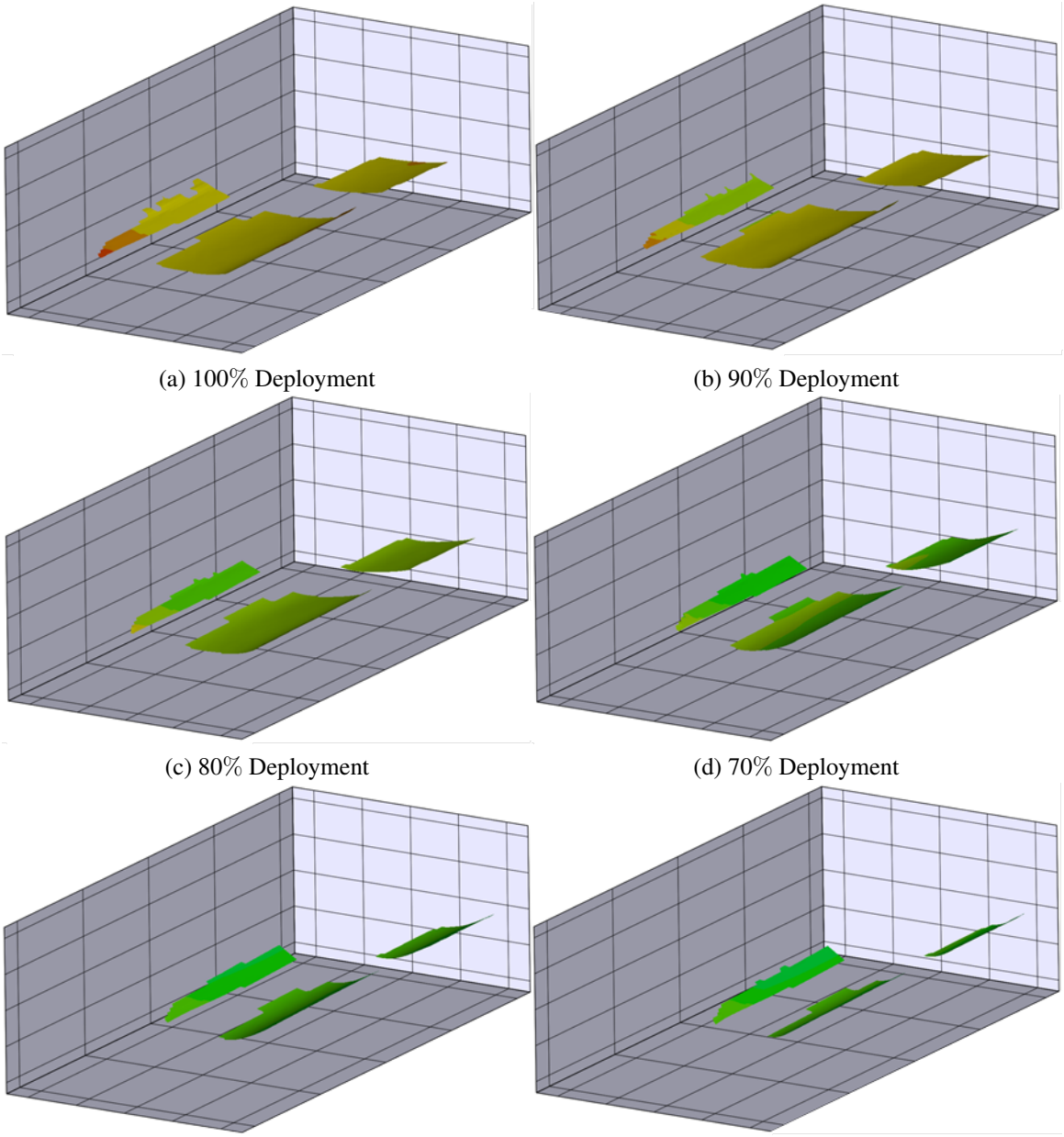

(a) 100% Deployment

(b) 90% Deployment

(c) 80% Deployment

(d) 70% Deployment

(e) 60% Deployment

(f) 50% Deployment

(g) DIC scale

Figure 3.18: DIC Wind-On 3-D Retraction

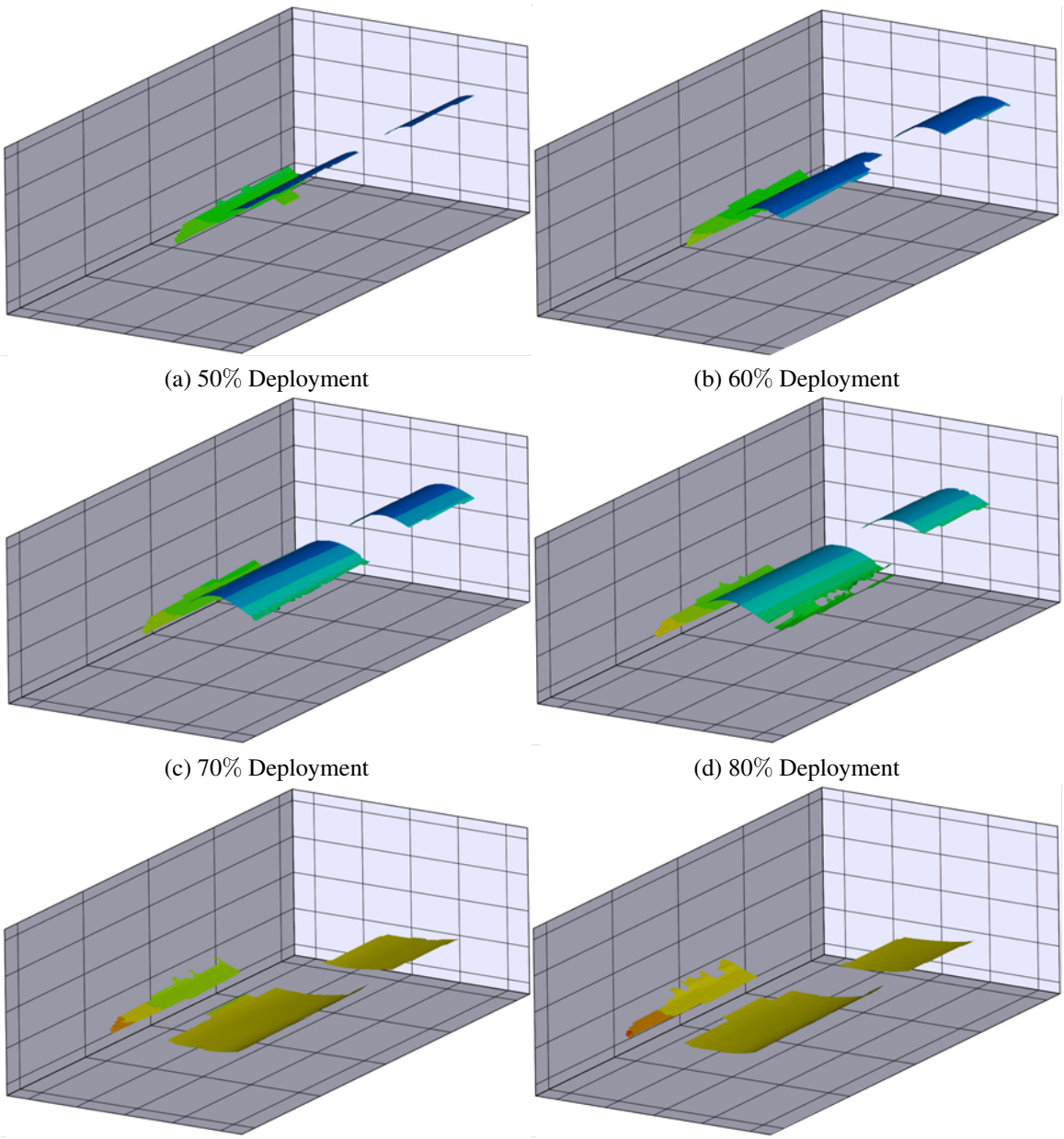

(a) 50% Deployment

(b) 60% Deployment

(c) 70% Deployment

(d) 80% Deployment

(e) 90% Deployment

(f) 100% Deployment

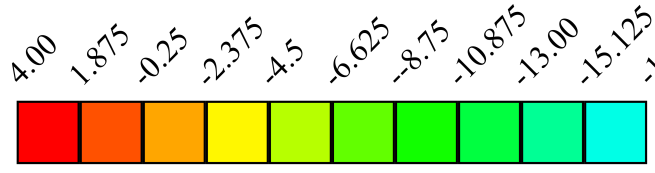

(g) DIC scale

Figure 3.19: DIC Wind-On 3-D Deployment

The images in Figure 3.18 and 3.19 show the 3D response of the SMA SCF as it completes a full retraction cycle during a wind-off DIC experiment. For reference, the long, thin regions correspond to the steel slat cusp, while the wider regions correspond to the SMA SCF. From this result, the SMA SCF is able to be tracked at each retraction frame, showing clear deformation as the SCF contacts the main wing. Note that on the deployment path, the SMA SCF remains in the stowed configuration nearly over the entire deployment path, only deploying outward when it passes 20% deployment. These results demonstrate that DIC testing is a valuable experimental method in wind tunnel testing when determining structural response.

To compare results from DIC testing, laser displacement testing, and FEA analysis, a common set of displacement data must span all three methods. Shown in 3.16, the Line of Interest marked on the DIC speckle pattern refers to the chord line which will be measured in all three methods. This section of the speckled area was chosen due to its uniqueness compared to surrounding area, and the ability of the area to be recognized clearly over multiple testing images and multiple experiments. The Line of Interest is located 15 mm inboard from the starboard side, quarter-span location. From this analysis line, comparisons are able to be made between the DIC wind-on and wind-off results, determining the influence of aerodynamic loading on the SMA SCF during a full retraction cycle. In Figures 3.20 and 3.21, the outer mold line of the lower surface of the slat is shown with respect to the structural coordinate system, previously mentioned, fixed beneath the test section and aligned with the free-stream velocity. Deployment stages lower than 50% deployment are not shown; the slat too close to the leading edge of the wing, reducing the quality and amount of data collected by the DIC system. This is one drawback to non-intrusive, far-field measurements on the SMA SCF. When the slat is retracted against the main wing, the response of the SMA SCF cannot be determined without line-of-sight.

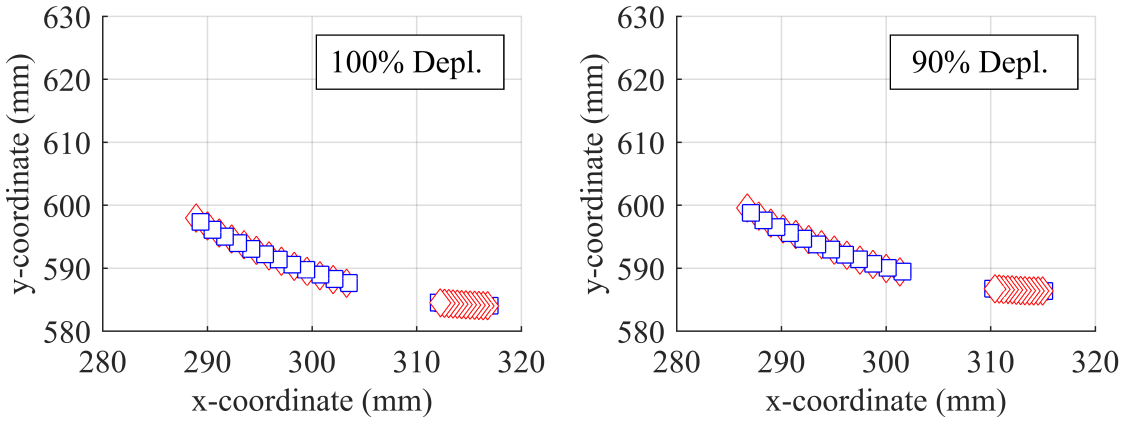

(a) 100% Deployment

(b) 90% Deployment

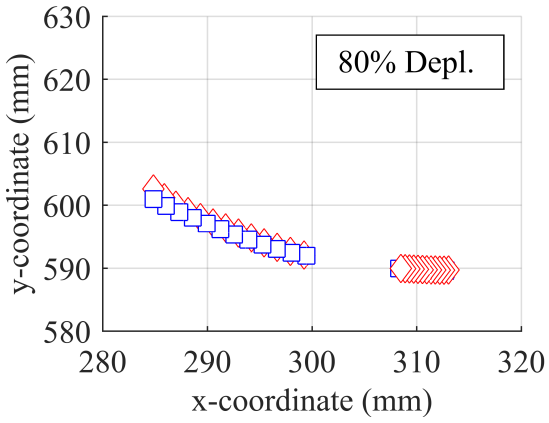

(c) 80% Deployment

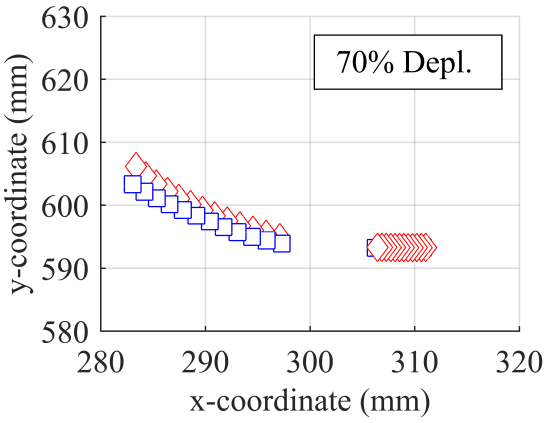

(d) 70% Deployment

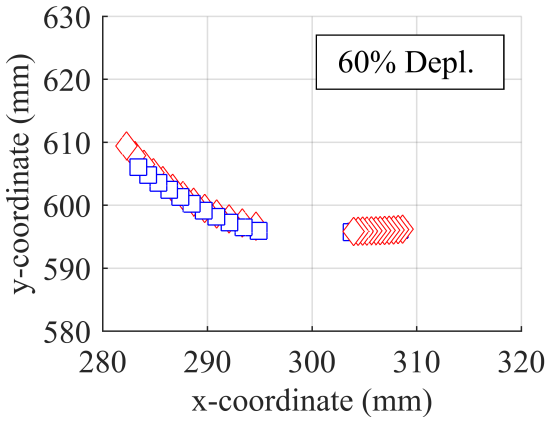

(e) 60% Deployment

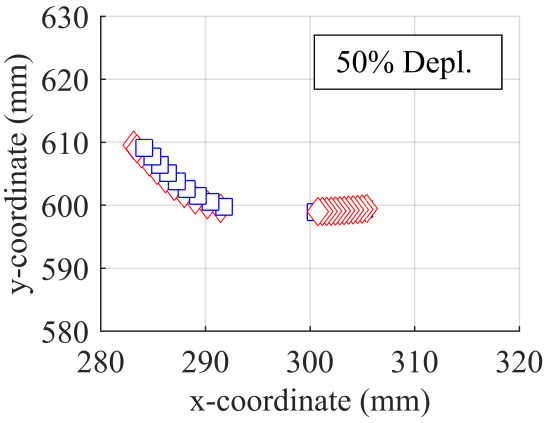

(f) 50% Deployment

Figure 3.20: DIC wind on/off comparison retraction arc.

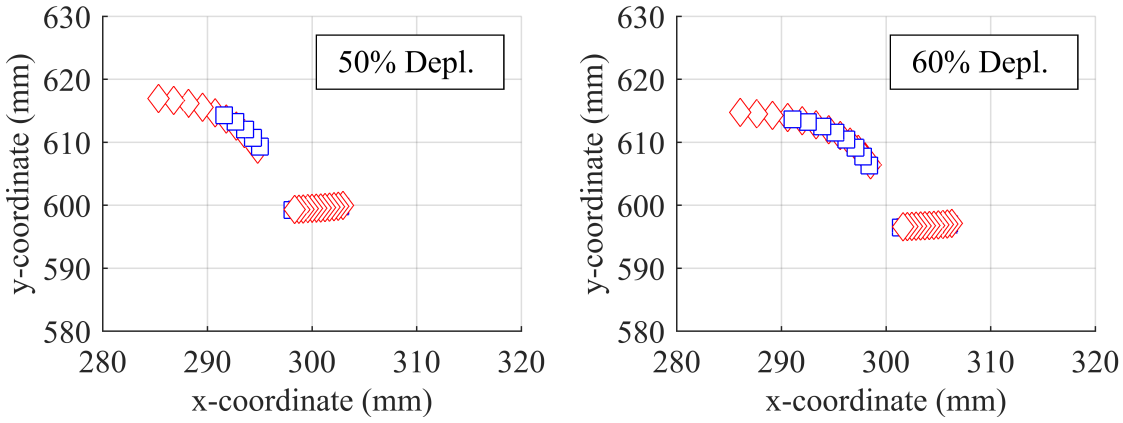

(a) 50% Deployment

(b) 60% Deployment

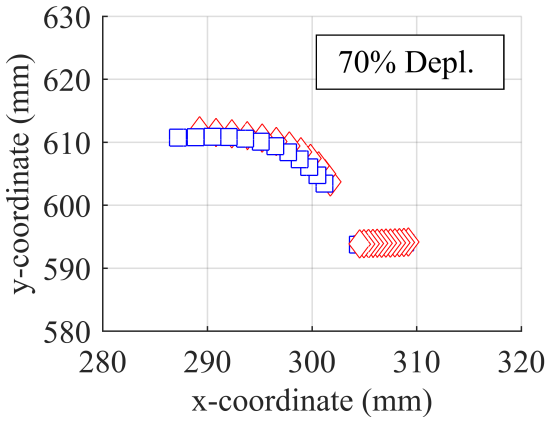

(c) 70% Deployment

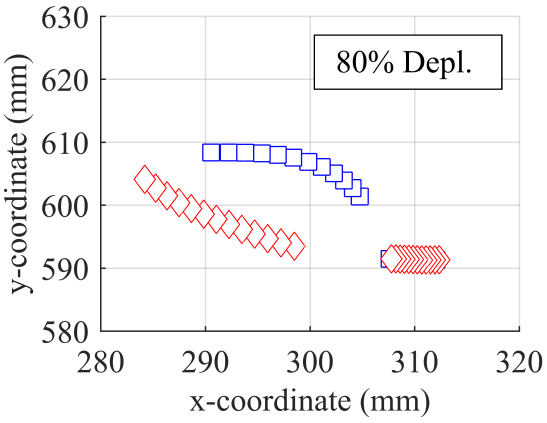

(d) 80% Deployment

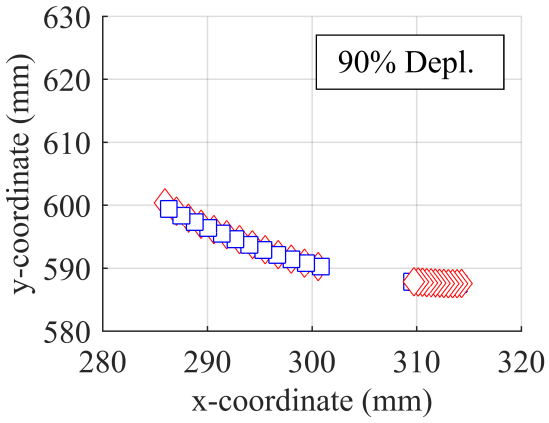

(e) 90% Deployment

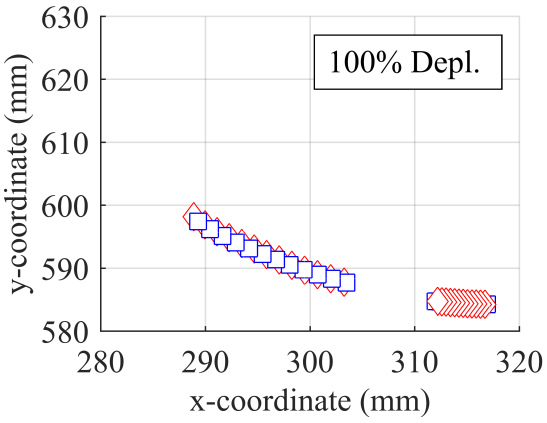

(f) 100% Deployment

Figure 3.21: DIC wind on/off comparison deployment arc.

Results from the wind-on DIC experiment are shown in Figures 3.20 - 3.21, which overlay the wind-on data, shown in blue squares, over the wind-off data, shown in red diamonds. Shown specifically in Figure 3.21 (c), the wind-on SMA SCF deploys outward at a lower percent deployment than the wind-off SMA SCF. This shift is caused by inaccuracies in the actuator response and imperfections in the slat-track design. The actuators are controlled by an open-loop signal being sent from the data controller, commanding the actuators to retract or deploy. The inputs sent to the actuators follow the desired test plan for the experiment, giving correct commands at each desired retraction point, however the actuators respond imperfectly with an error of up to 5% retraction. It is of note, shown throughout the retraction path, that the SMA SCF wind-on results are displaced further away from the slat (shown lower than the wind-off data). This results is unexpected, as previous modeling results suggest sufficient stiffness in the SMA SCF under flow to resist any sizable deflection [25]. Future work will investigate this outward deflection further.

3.3.2 Laser Displacement

To Support the results from DIC experiments on the slat cove filler, laser displacement testing was conducted to measure the response of the SMA-based slat cove filler during a slat retraction cycle. As previously mentioned in the Methods chapter, measurements were taken of the lower surface of the wing and slat to determine the effects of slat retraction on the SMA SCF. The resolution of data collected from the LDS is influenced by both instrument limitations and the speed at which the laser is rotated. For tests on the SMA SCF, the LDS was manually rotated with a total sweep time of seven seconds per sweep. This was to ensure at least 70 data points were collected during each test run. Discussed in greater detail in the Conclusions and Future Work is the possibility of servo-motor controlled LDS rotation, reducing error from human sources.

As mentioned previously in Section 2.1.2, the Pitch Plunge Drive System (PPDS) gen-

erates significant electromagnetic interference, affecting unshielded devices and connections. The rotary potentiometer, is greatly affected by the activation of the PPDS, with residual signal noise increasing by two orders of magnitude from 0.05° background to 5.00°. This limited the application of the PPDS to wind-off structural deflection tests. However, results from DIC experiments and LDS can still be used to validate computational models for wind-off retraction response. Results from the wind-off LDS experiment and DIC results are shown in Figures 3.22 and 3.23. The experimental data collected during LDS testing is shown in blue, while DIC results are shown in red. One benefit to the LDS, is the ability to measure surfaces without the need for a detailed speckle pattern, thereby expanding the area of data collected significantly from the DIC tests.

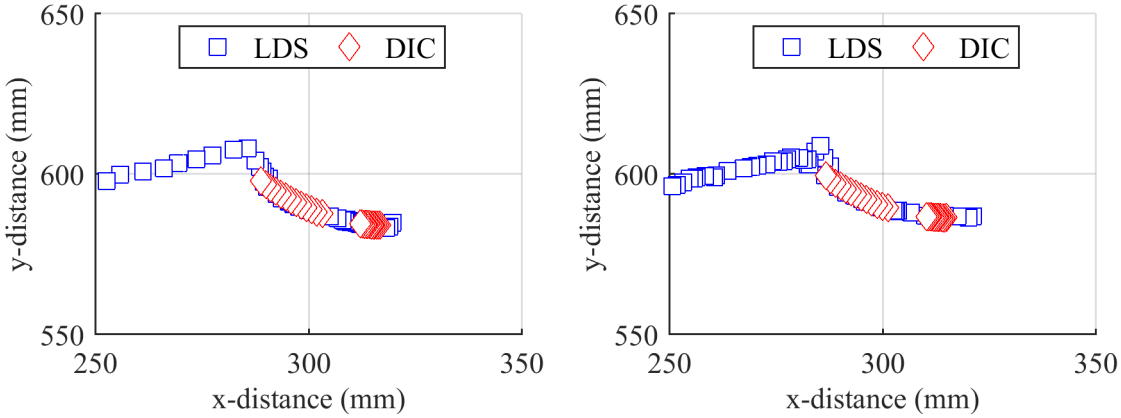

(a) 100% Deployment

(b) 90% Deployment

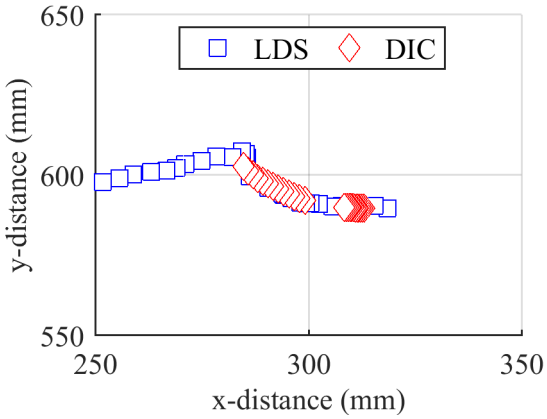

(c) 80% Deployment

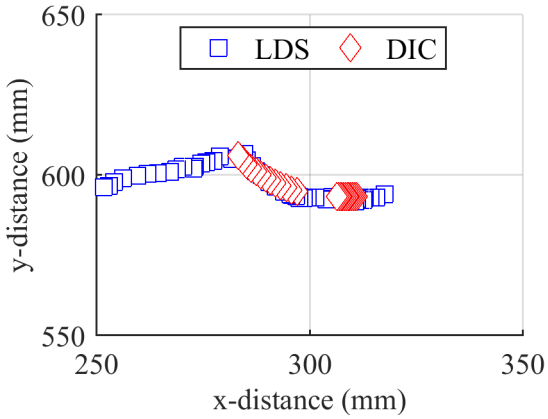

(d) 70% Deployment

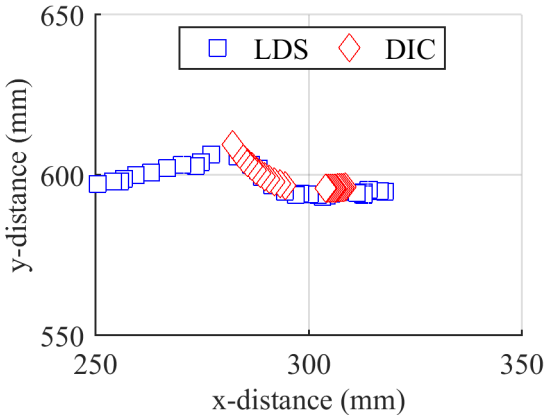

(e) 60% Deployment

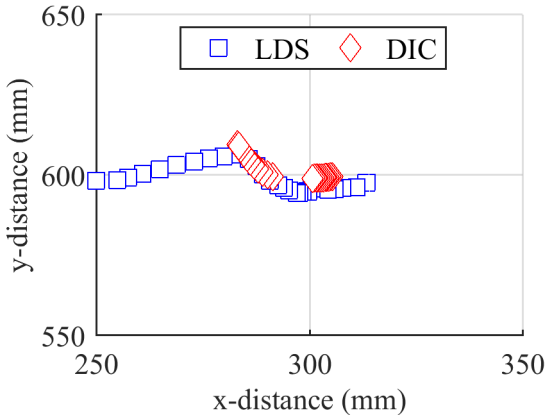

(f) 50% Deployment

Figure 3.22: Laser + DIC Wind-Off Retraction

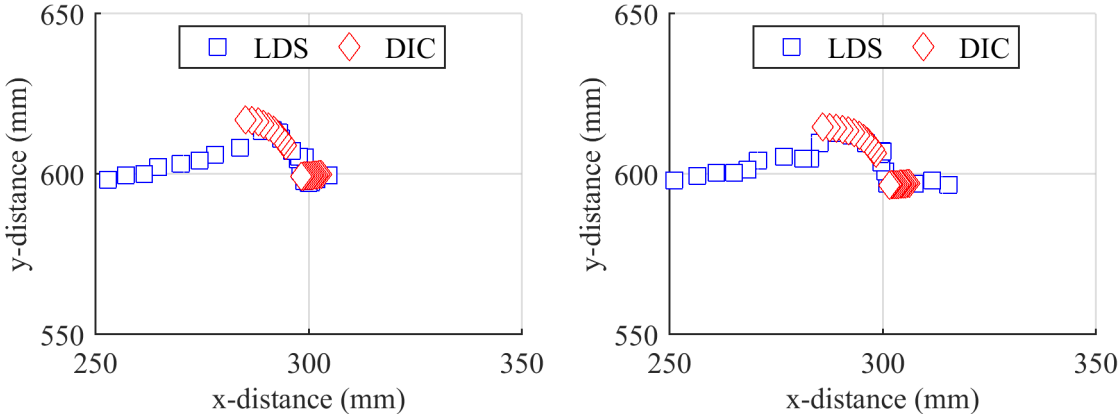

(a) 50% Deployment

(b) 60% Deployment

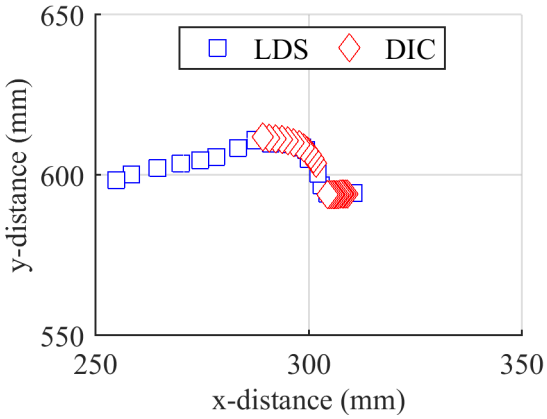

(c) 70% Deployment

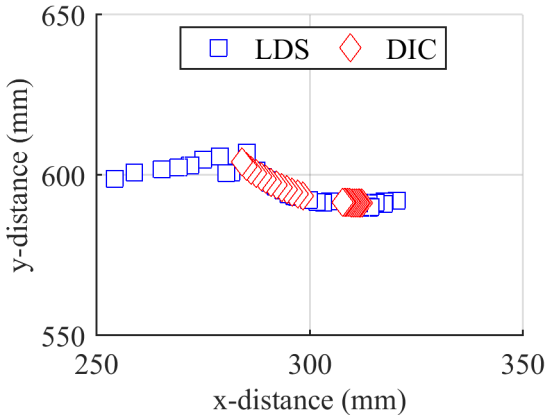

(d) 80% Deployment

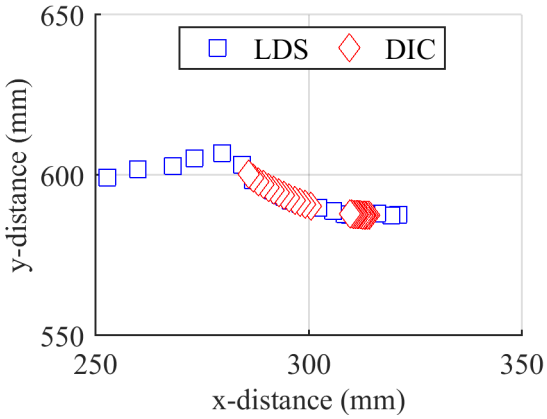

(e) 90% Deployment

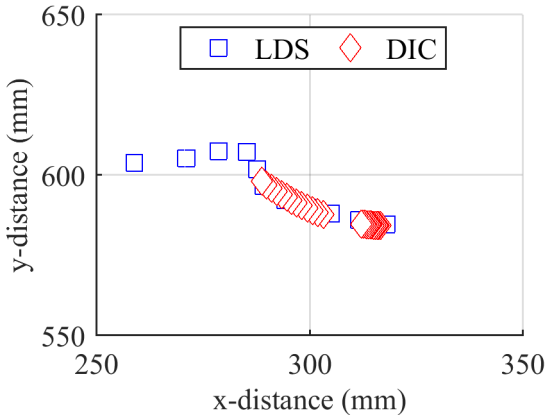

(f) 100% Deployment

Figure 3.23: Laser + DIC Wind-Off Deployment

Each test (LDS, DIC) was conducted separately, as the sensor installation area for the LDS blocked the view of the DIC camera system from above. This fact, coupled with inconsistent response from the slat actuators is shown in multiple frames of the data. Each test recorded slighly different retraction percentages to the same input voltage, corresponding to imperfections in matching retraction percentage data between LDS and DIC results. However, data collected from both the DIC and LDS systems matches well, with the LDS filling in data gaps of the DIC system caused by discontinuous speckle pattern. Differences in response can also be attributed to how the SMA SCF reacts at high retraction percentages. At percentages greater than 50% in the retraction arc, the actuators struggle to smoothly and evenly retract the slat. During the deployment arc however, the actuators are assisted by the reaction force of the SCF acting on the main wing, leading to more accurate slat placement. This can be noted by better matching between the DIC and LDS results, especially on the deployment arc shown in Figure 3.23. Note that the DIC and LDS results closely match during the snap-out action between 30% and 20% retraction and subsequent return to fully deployed state.

Significant erratic measurements can be seen at higher levels of retraction (>50%) in the LDS results, one cause is suspected to be a shortcoming of the LDS. The sharp change in geometry between the leading edge of the main wing and slat cove filler is nearly parallel to the emitted beam from the LDS. At high incidence angles with respect to measurement surface, where the measured surface is parallel or near parallel to the emitted beam, there is a high level of uncertainty in the distance measurement from the LDS. However, with perpendicular surfaces, expected errors in measurement are within 0.05 mm. One major benefit to the use of the LDS, is the ability to have a wide view-field of measurement. The LDS is able to capture the leading edge of the entire SMA SCF wing prototype reaching past the mid-chord location on the wing. With slight modifications to the viewing window, it would be possible for the LDS to measure the entire lower surface of the SMA SCF wing

prototype from leading edge to trailing edge. When compared directly with the use of DIC imaging techniques, the LDS is a low resolution, wide-angle measurement tool (0.05 mm resolution, 180°>x>90° view-angle), while the DIC allows for more precise but narrow field of view measurements (1920×1200 pixels, focused on a 16 cm × 12 cm field of view).

3.3.3 Computational Modeling

Results from finite element modeling will be presented to match experimental results, such that a good comparison between experiment and computational modeling can be made. Of most interest is the geometric response of the SMA SCF during a full retraction cycle, with slices of the leading edge slat and slat cove filler being taken along the same cutting plane as the DIC and LDS results. Once validated with the experimental data, the computational model can be utilized to further explore the SMA SCF performance, and to provide a more complete description of the structural response. Of key interest is the slat trailing edge deflection across the entire span of the wing prototype. Experimental measurements were collected during a wind-off laser displacement test of key points on the trailing edge tip of the slat, which will be compared with computational results.

3.3.3.1 Computational Validation with Experiment

To validate the accuracy of the computational model, comparison must be made between experimental results collected during DIC and LDS tests. Limitations in data collected during both experiments limit comparisons to changes in slat cove filler configuration and orientation with respect to slat retraction percentage. As previously presented, results from LDS and DIC testing compare well over the two-dimensional lower surface outer contour. The comparison between the experiments and computational modeling tools are shown in Figures 3.24, 3.25. As previously discussed when comparing DIC and laser results, errors in the actuation control system lead to inconsistent slat retraction lo-

cations, especially at high retraction percentages. This is clearly shown when comparing results from FEA with the DIC and LDS systems. However, it is important to note better matching between results from the DIC experiment and FEA.

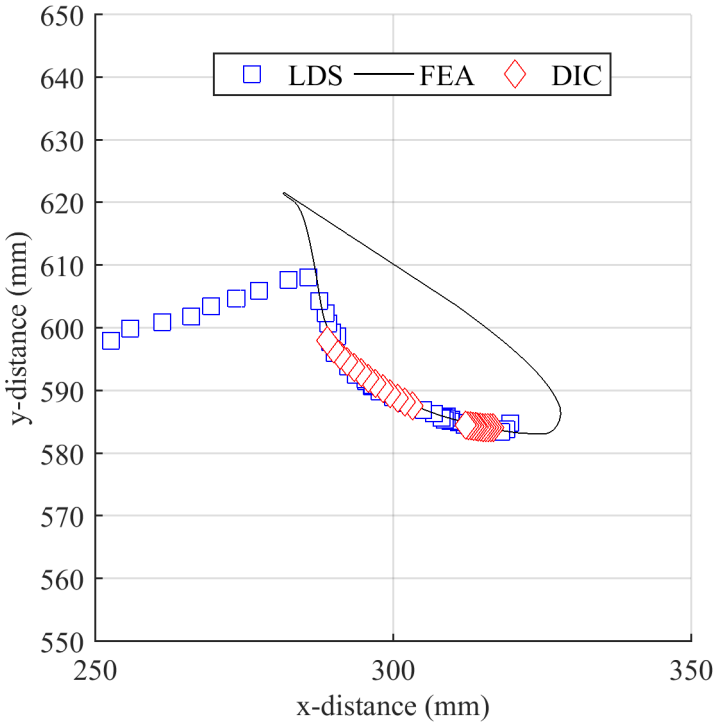

Figure 3.24: Laser, DIC, and Abaqus comparison of lower slat and slat cove filler outer mold line at 100% Deployment, 6° angle of attack.

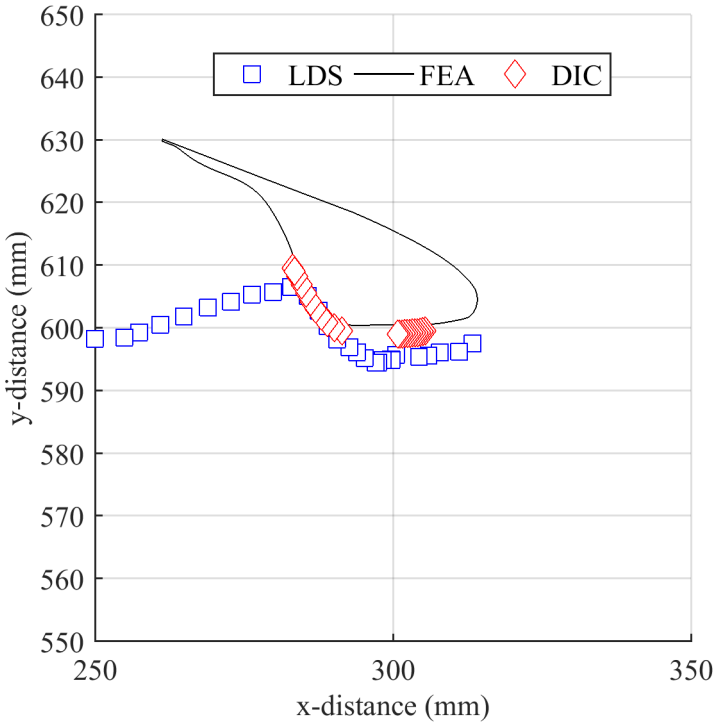

Figure 3.25: Laser, DIC, and Abaqus comparison of lower slat and slat cove filler outer mold line at 50% Deployment, 6° angle of attack.

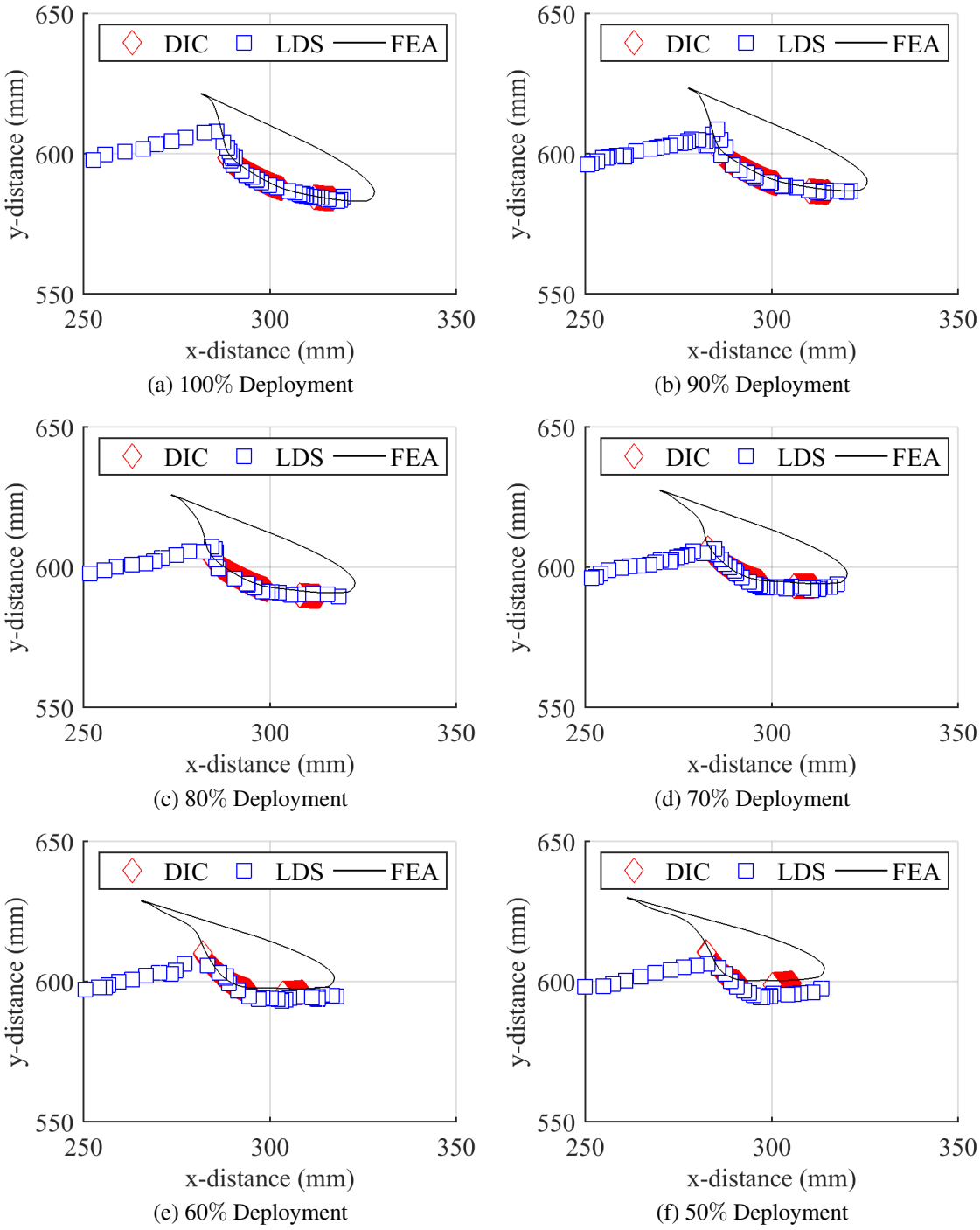

(a) 100% Deployment

(b) 90% Deployment

(c) 80% Deployment

(d) 70% Deployment

(e) 60% Deployment

(f) 50% Deployment

Figure 3.26: Laser + DIC + FEA Wind-Off Retraction

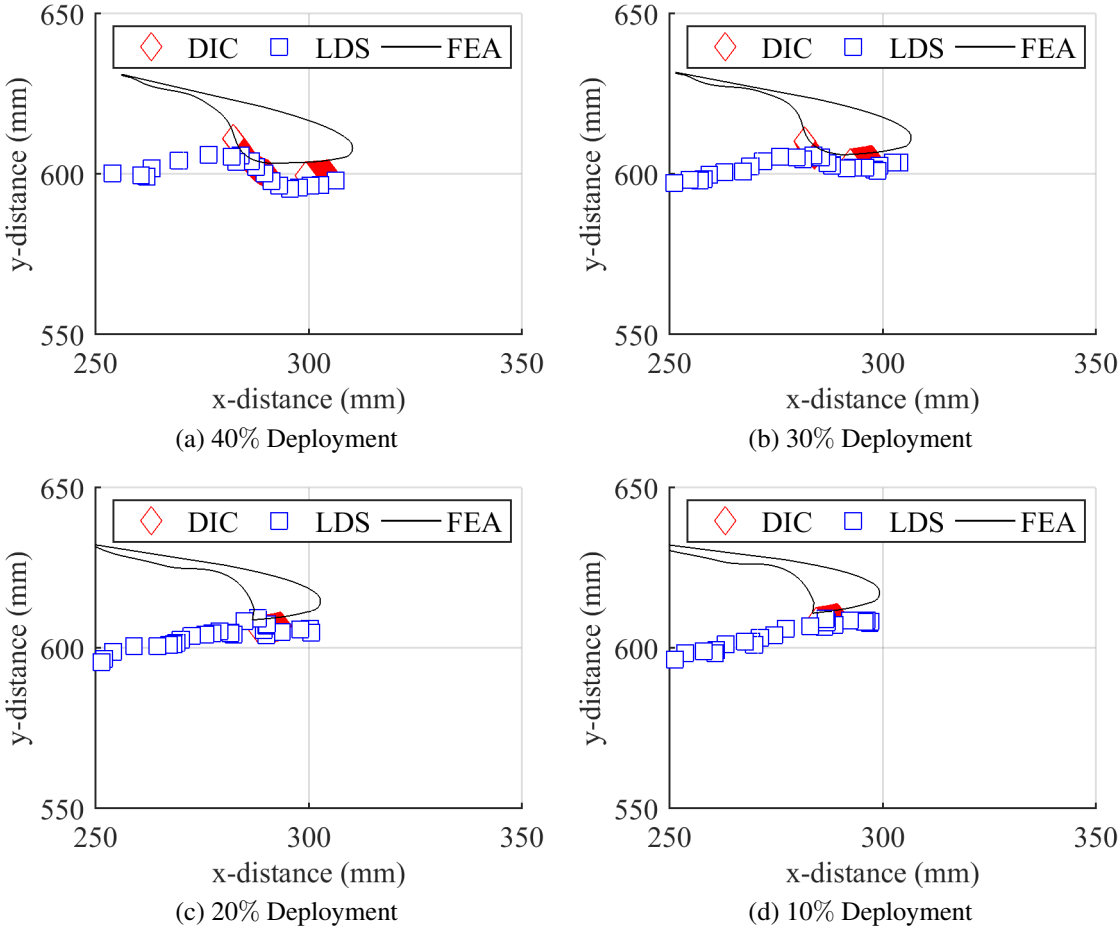

(a) 40% Deployment

(b) 30% Deployment

(c) 20% Deployment

(d) 10% Deployment

Figure 3.27: Laser + DIC + FEA Wind-Off Retraction (cont.)

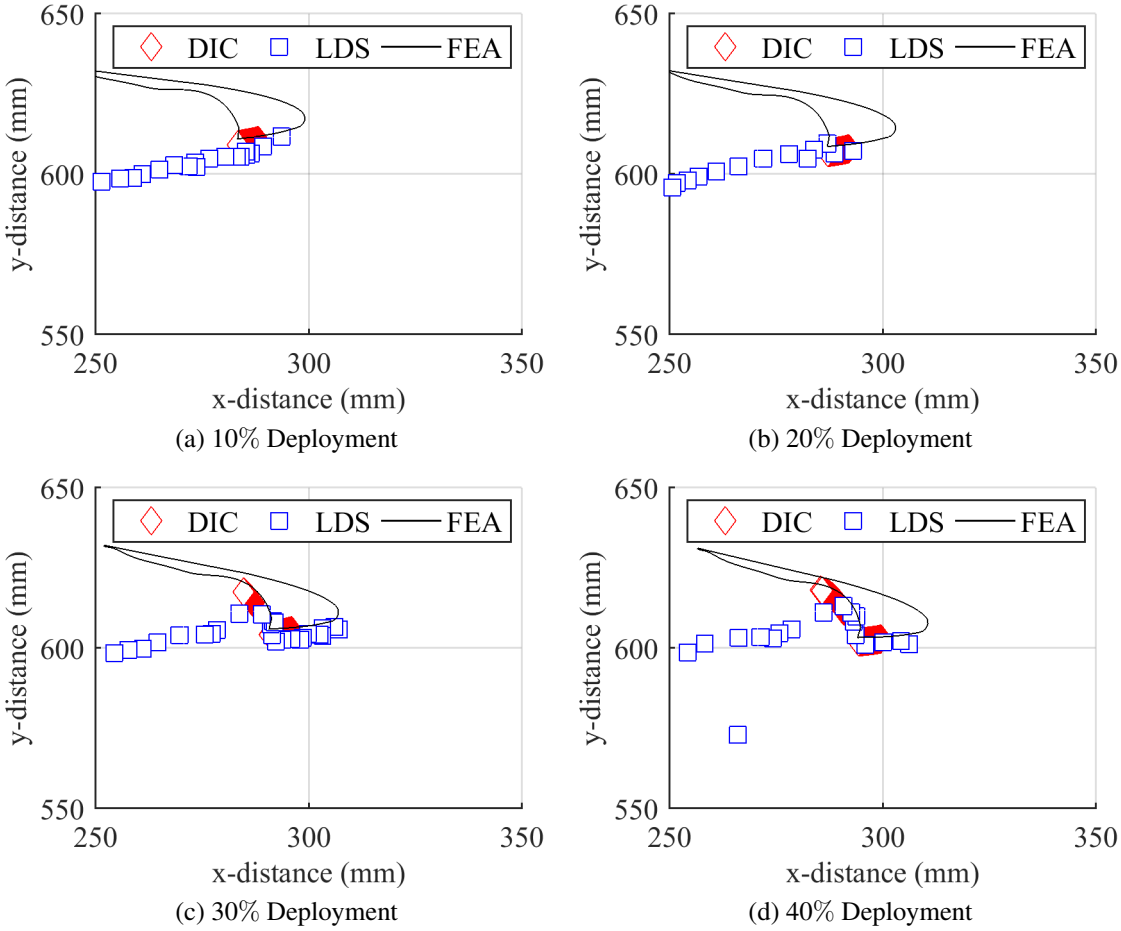

(a) 10% Deployment

(b) 20% Deployment

(c) 30% Deployment

(d) 40% Deployment

Figure 3.28: Laser + DIC + FEA Wind-Off Deployment

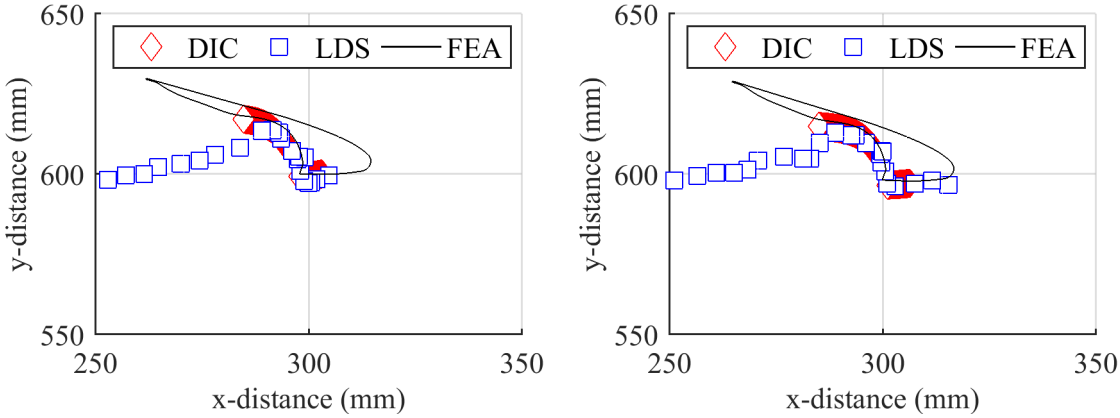

(a) 50% Deployment

(b) 60% Deployment

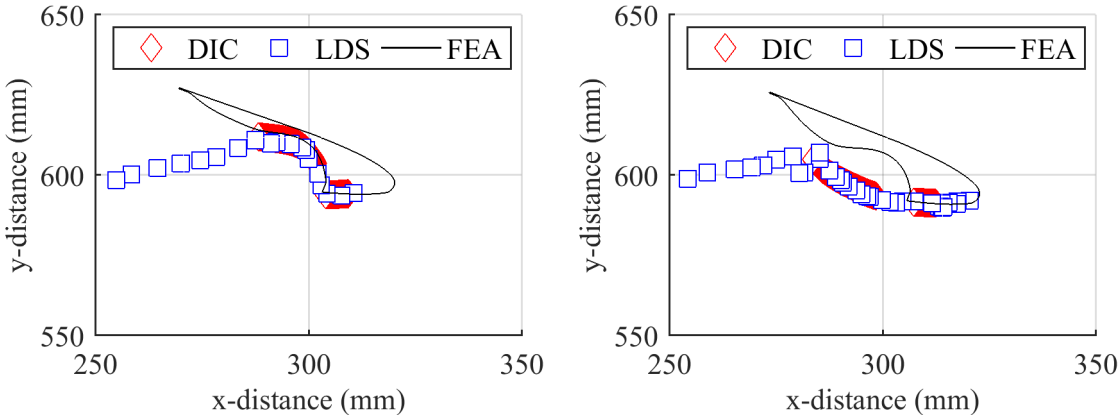

(c) 70% Deployment

(d) 80% Deployment

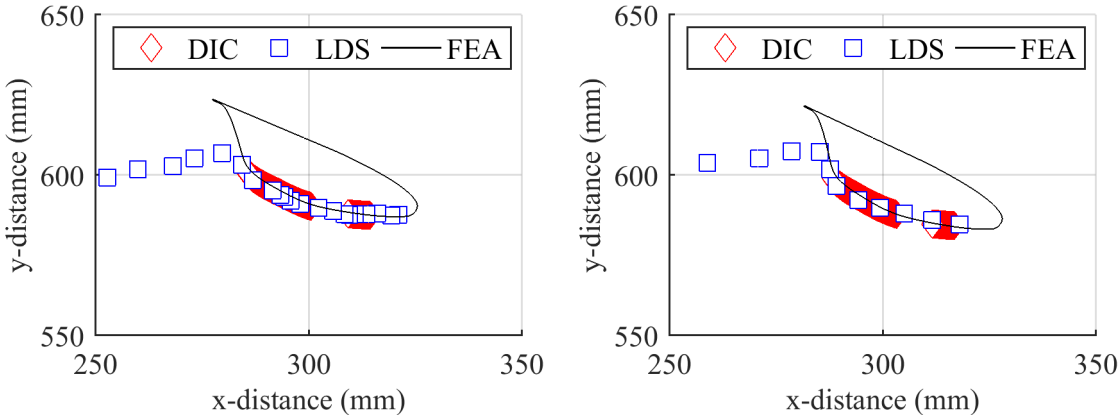

(e) 90% Deployment

(f) 100% Deployment

Figure 3.29: Laser + DIC + FEA Wind-Off Deployment (cont.)

With good agreement between structural experiments and computational modeling tools, further structural analysis can be made using the FEA model to learn more about the response of the SMA SCF. Shown below in Figure 3.30, the stress distribution over a section of the span of the SMA SCF slat. The area of highest stress during retraction occurs when the SMA SCF first begins to stow inside the slat cove. This stress concentration is not present in the deployment arc where the SMA SCF remains stowed until near the end of the arc. At this point in the retraction arc, the SMA SCF experiences 281 MPa stress from compression into the slat cove. The area of highest stress over the full retraction cycle occurs at the bond line between the SMA SCF and the top trailing edge surface of the slat. At this point, the SMA SCF experiences 304 MPA stress. From the SMA characterization shown in Section 2.1.5, the SCF is below the transformation stress required to begin phase change.

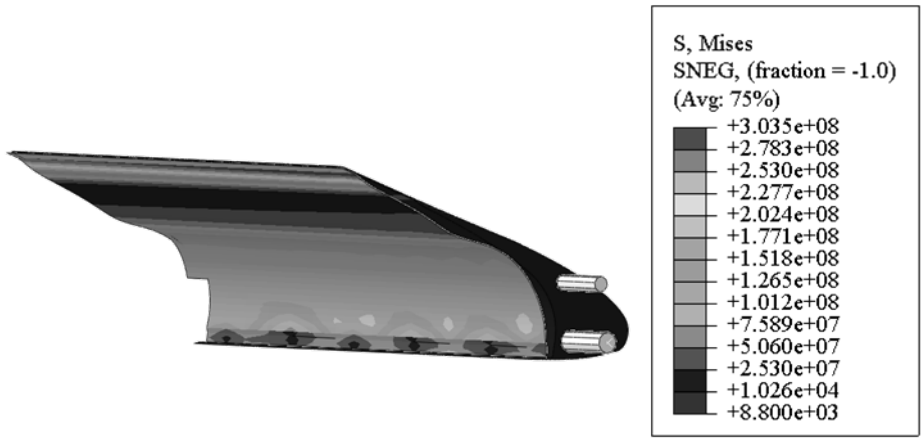

(a) SCF + Slat bond stress

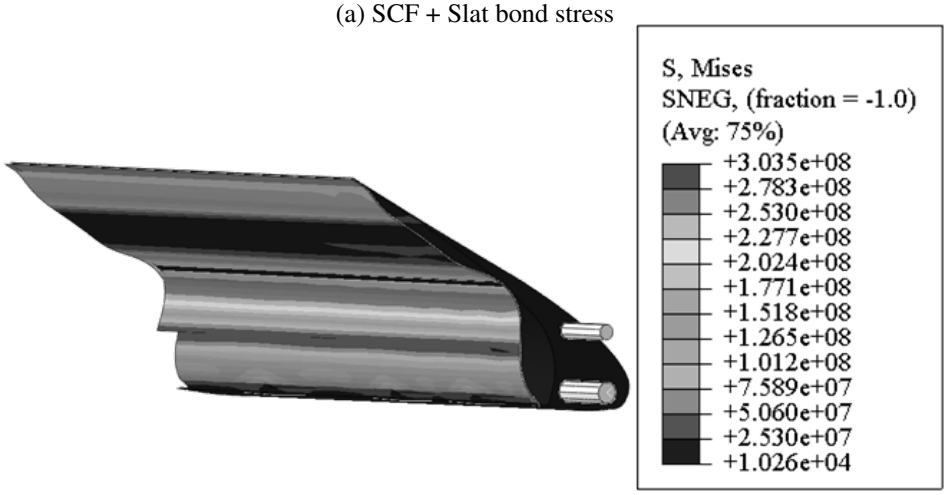

(b) SCF retraction stress

Figure 3.30: High stress values during slat retraction

3.3.3.2 Tip Deflection Testing

To further validate computational modeling tools, the trailing edge of the slat was measured during a wind-off retraction cycle to determine slat tip deflection as a result of retraction. At each stage of a full retraction cycle, the normal distance between the main wing surface and the trailing edge of the slat was measured using a ruled measurement device. The tip deflection was measured at three points on the starboard half-span section of the wing. The slat acts as a beam with a pin connection at each end, and a distributed applied force from contact with the main wing. Typical beam solutions for this boundary condition and load application dictate a parabolic response with the most deflection at the midpoint of the beam. As shown in Figure 3.31, selected results from comparing tip deflection measurements between experimental results and FEA results. During the full retraction cycle, the FEA predicts a maximum vertical tip deflection less than 0.5 mm however, experimental results differ during the entire retraction cycle. At the maximum, the experiment measured the maximum tip deflection to be 3.5 mm away from the surface of the wing.

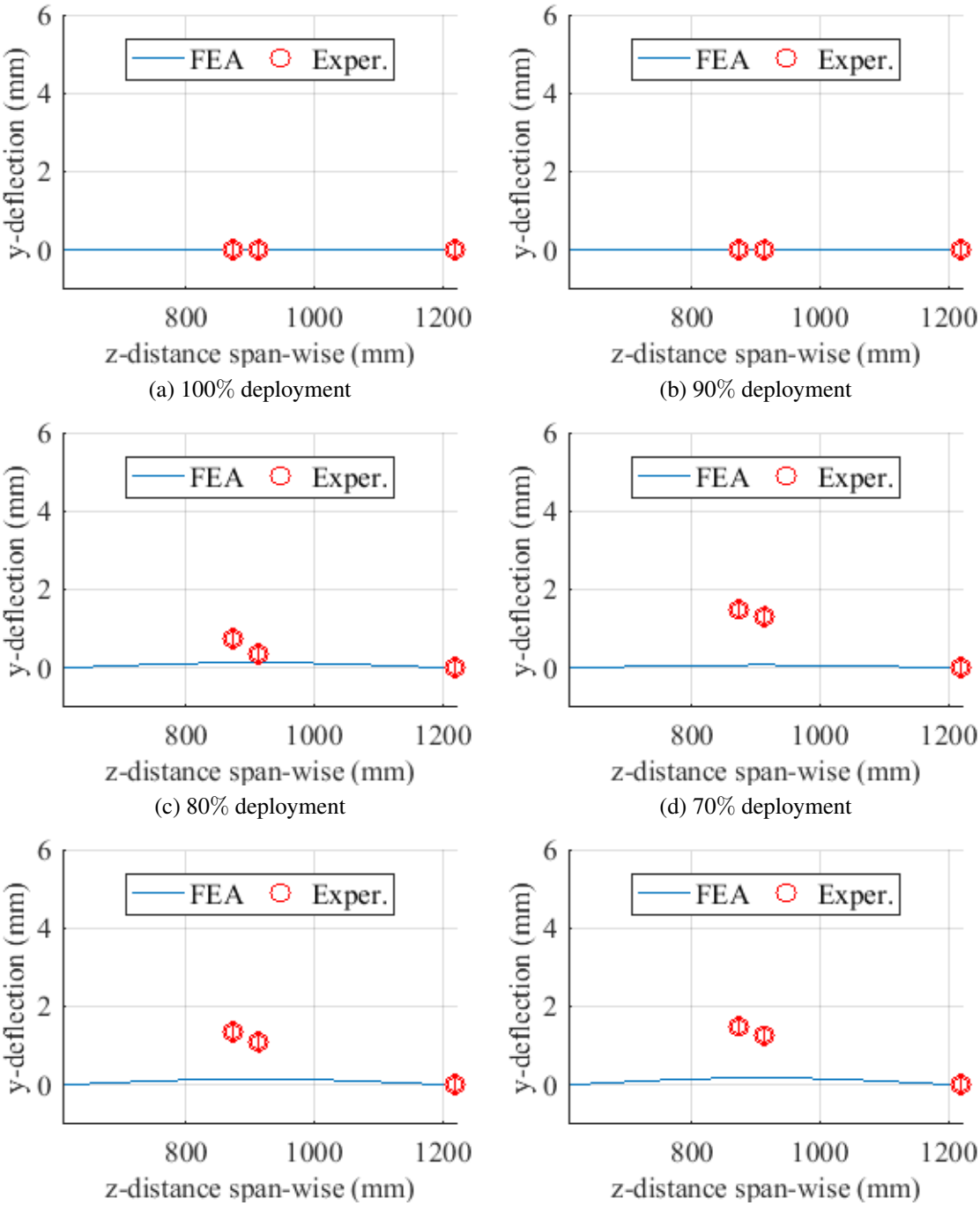

(a) 100% deployment

(b) 90% deployment

(c) 80% deployment

(d) 70% deployment

(e) 60% deployment

(f) 50% deployment

Figure 3.31: Tip deflection comparison between experiment and FEA results

Differences in results can be explained through imperfections in experimental wing prototype construction. The experimental model uses a sliding pin connection at each span extent, and has a splitter plate at mid-span to assist in high lift device retraction. The sliding pin connection tolerance is too large for precise slat and flap control, and allows for rotation of the slat down and away from the main wing when resisting the reaction force of the SMA SCF on the main wing.

3.4 Closing Remarks

From experiments conducted on the SMA SCF wing prototype, and co-developed computational FEA model, conclusions can be made about the performance impacts of the SMA SCF. The aerodynamic performance of the constructed wing prototype is improved by the addition of the SMA SCF. Specifically, the lift is increased at low angles of attack, and the drag is reduced at higher angles of attack. This leads to a more efficient wing design across all angles. Structurally, results from DIC testing, LDS testing, and computational modeling tools match across a full retraction cycle, with results from DIC testing providing the highest resolution experimental data to compare best with computational modeling. The use of a custom-design laser displacement sensor system was validated with DIC results, providing a new experimental platform for low-cost, simple measurement system able to determine spatial geometry of complex surfaces at long distance (1.00 m). Results from the validated FEA model were then used to show regions of maximum stress in the SMA SCF and at which point in the retraction cycle they occurred.

4. CONCLUSIONS AND FUTURE WORK

This chapter discusses conclusions from the results presented in the previous section. Additionally, future work and testing improvements made in the slat cove filler project will be discussed. The aerodynamic characteristics of the addition of the slat cove filler will be made. Its contributions and detriments to the overall aerodynamic performance of the CRM-based wing prototype. The structural response of the SMA SCF will be discussed by interpreting experimental results and comparisons with developed computational modeling tools. Overall experimental limitations, discovered shortcomings in experimental design, and future solutions will be discussed in detail to inform the reader on how to improve experimental results. Ultimately, the future developments in testing the SMA-based slat cove filler concept will be discussed with details presented on future experimental prototypes, experimental procedures, and new methods in determining the aeroacoustic response of the SMA SCF.

4.1 Aerodynamic Performance

While the introduction of the SMA-based slat cove filler only directly effects the design of the leading edge slat, the aerodynamic influences outweigh the added complexity of the design and construction. Shown both through experimental tests directly measuring the overall lift generated by the wing prototype, as well as through pressure measurements, the aerodynamic performance of the SMA SCF wing prototype increased in lift performance, and reduced drag in the intended performance envelope. However, aeroacoustic conclusion cannot be made based on the aerodynamic performance of the SMA SCF wing. For future aerodynamic tests, improvements can be made to standardize testing methods, as well as improve the quality of the collected data.

Presented previously in the results, clear improvements have been made by the addi-

tion of the SMA-based SCF. In the main flight envelope for the leading edge slat, between 4°and 8°angles of attack during the take-off, approach, and landing phases of flight, the lift performance is improved over the untreated slat configuration. Most notably however is the large reduction in drag in the flight envelope. Figure 4.1 compares the lift and drag performance increases in the treated slat configuration with the untreated slat configuration, also shown previously in the Results section. The improved effects of the SMA SCF are not just present in the flight envelope either. At low angles of attack, the flow attaches to the lower surface of the wing section leading to leftward shift in the lift curve slope of the wing. This also correlates to higher coefficients of lift in the treated slat at lower angles of attack at each discrete angle position

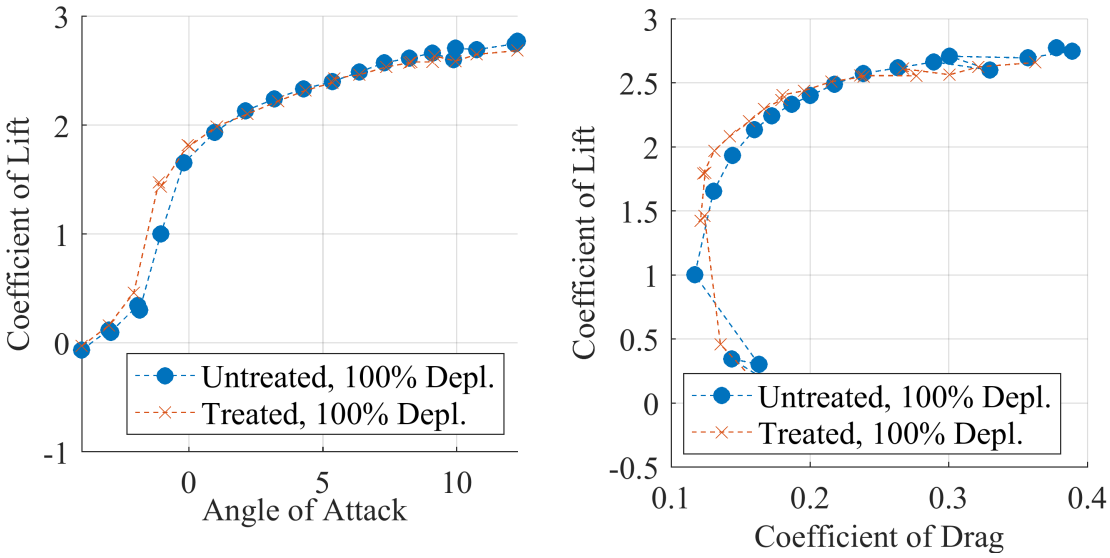

(a) Lift Curve Slope

(b) Drag Polar

Figure 4.1: Aerodynamic performance of treated slats compared with untreated configuration

Below in Figure 4.2, the aerodynamic efficiency is presented in the form of the lift

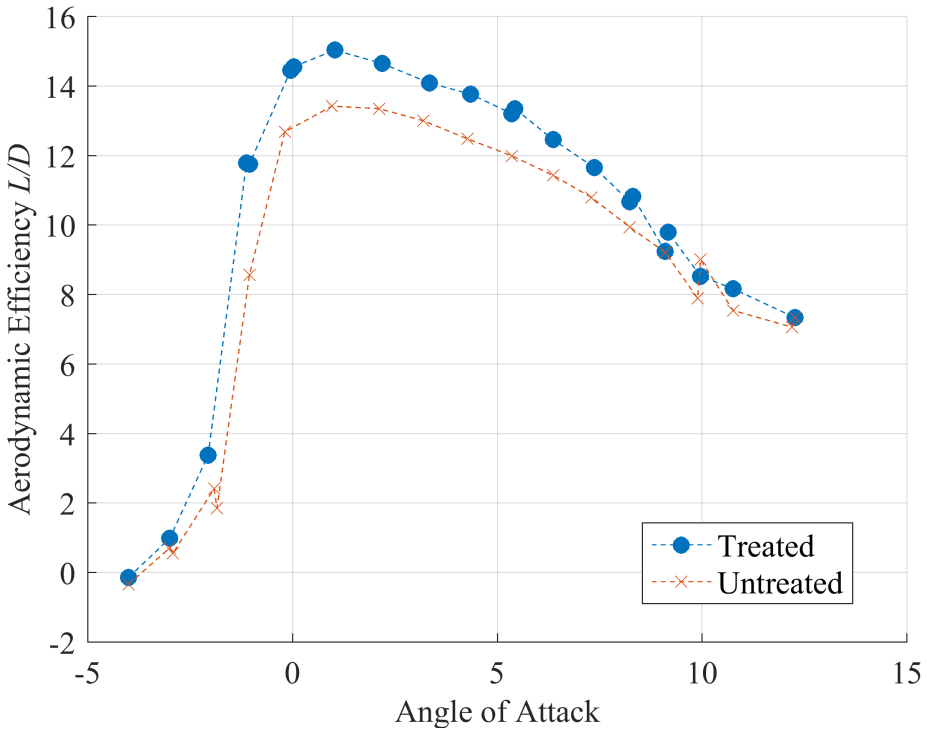

Figure 4.2: Aerodynamic efficiency comparison between treated and untreated wing configurations (L/D)

force divided by the drag force plotted versus the angle of attack of the wing prototype. This parameter is a measure of the aerodynamic efficiency, coupling aerodynamic lift and drag. As shown the inclusion of the SMA SCF to the leading edge slat produces an increase in overall aerodynamic performance. This is further reinforced with results from the Scanivalve pressure scanner collecting the pressure distribution over the main wing during wind tunnel testing. The treating slat configuration generates greater lift at lower angles of attack, with only slight reductions at high angles.

Experiments conducted for this research were able to produce quality data, capable of concluding that the addition of the SMA SCF improved the aerodynamic performance. However improvements in data collection procedure and experimental methods could have

simplified testing methods and reduce irregularities from different data collection methods. Most notable is the recent discovery of the PPDS as a large source of EMI emissions during testing. This source of noise in data collection was accidentally discovered during a wind-off instrument verification test which did not require the use of the PPDS to secure the wing at a constant angle of attack. All previous tests had been conducted with the PPDS drive motor engaged to secure the wing prototype from free rotation and unintended vibration. The PPDS EMI emissions effect only unshielded data collection sources most visibly (i.e. potentiometer (LDS), temperature sensor, velocity sensor). However, data from the temperature, and velocity sensors directly affect the quality of the coefficients of lift and drag with them appearing as large terms in the dynamic pressure. It was also found that the potentiometer used in the LDS was rendered almost useless by the introduction of the PPDS EMI. Background electrical noise during normal operation typically introduces an error of 0.05°, at least an order of magnitude lower than what is needed to report accurate data for this research. However, the activation of the PPDS increases the electrical noise in the data to over 5°, well over two orders of magnitude increase. Proper cable shielding will improve data streams from previously mentioned sources, however sensor shielding may be required to insulate the electrical connection between each device and the data acquisition device. In the future work section, at the end of this chapter, improvements in structural testing characteristics will be further discussed. The implementation of a solid, full span slat will be investigated, which removes the exposed leading edge slat track, potentially reducing drag and improving lift characteristics of the wing.

4.2 Structural Performance

Previously presented results from multiple structural response experiments were used to validate and develop better computational design tools and accurate models of the response of the SMA SCF. This section will dicuss what can be concluded about the in-

fluence of the SMA SCF on the performance of the CRM-based wing section and wing prototype. Experiments were conducted on the SMA SCF using DIC imaging and a custom design LDS to measure the response of the SMA SCF during a retraction cycle. As well, a computational model of the scaled wing prototype was developed using ABAQUS CAE, and validated with experimental results, to predict the structural response of the SMA SCF during retraction.

As presented in the results previously and shown again in Figure 4.3, 4.4, results showing the SMA SCF geometry at multiple stages of slat retraction. A clear case for model validation through experimental results is made, showing agreement across the entire slat retraction cycle.

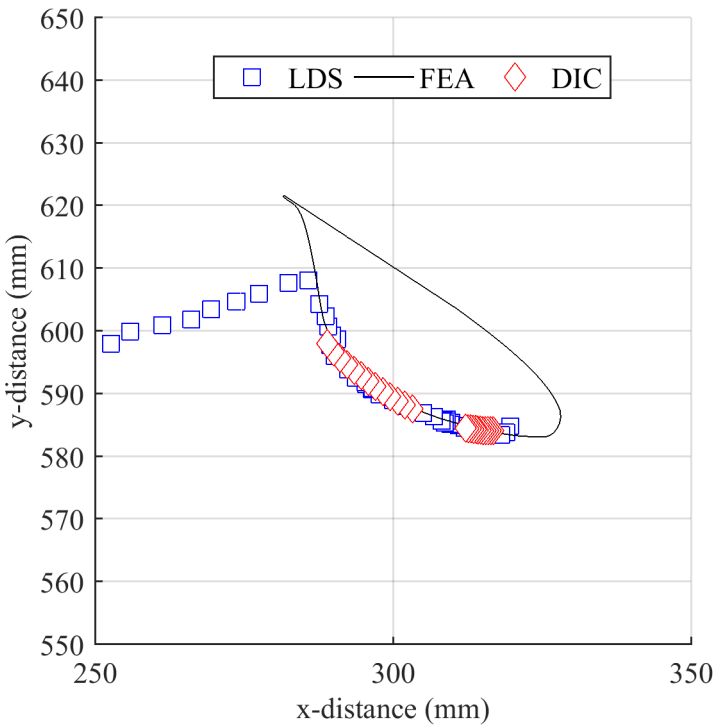

Figure 4.3: Laser, DIC, and Abaqus comparison of lower slat and slat cove filler outer mold line at 100% deployment, 6°angle of attack.

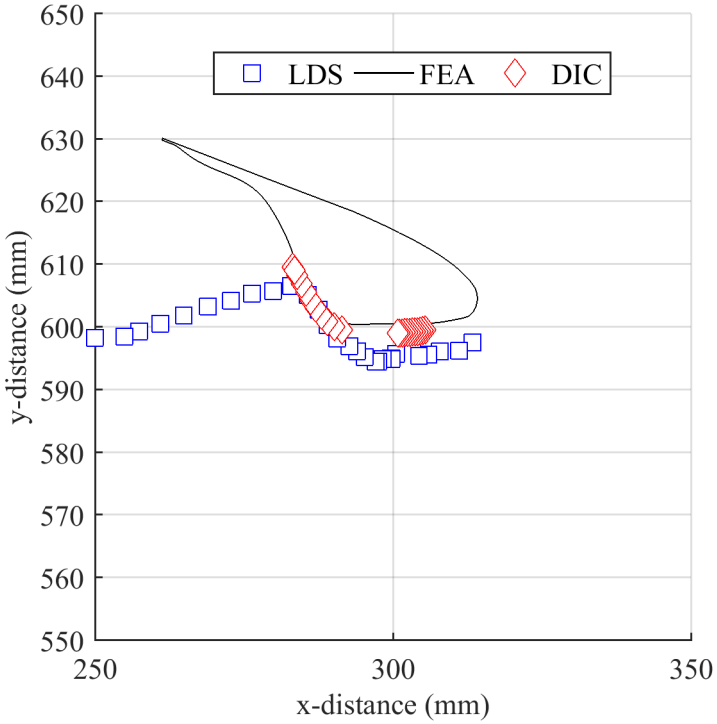

Figure 4.4: Laser, DIC, and Abaqus comparison of lower slat and slat cove filler outer mold line at 50% deployment along the retraction arc, 6°angle of attack.

As mentioned previously, significant EMI interference is received by the potentiometer system. This makes experimental testing with the LDS unfeasible during wind-on structural testing. Possible solutions to resolve this issue include: improved cable and system shielding from EMI emissions, secondary pitch secure system to allow fixed pitch during wind tunnel experiments. Another limitation in structural testing the wing prototype is the inconsistency and variability in slat retraction during a retraction cycle. Currently, the slat and flap actuators are controlled using open-loop Actuonix linear actuators which respond to an input signal and report position with a voltage signal. During multiple experiments in which the high lift devices were actuated produced inconsistent output voltage signals with the same input signal. The maximum output signal variation never exceeded 5% re-

traction from the commanded retraction point, however for fixed-frame measurements like the LDS and DIC systems, any difference in slat position produces different results than expected. This makes consistent retraction measurements difficult to replicate. One simple solution is to conduct the LDS and DIC experiments simultaneously during a single retraction cycle. Due to test area difficulties, amount of space required for each system, this was not conducted for this research, however it should be investigated as a quick solution to inconsistent results during a span of multiple experiments. Another potential solution is to use a closed-loop feedback controller connected to an inertial measurement system which determines the position of the slat with respect to the retraction arc. This would reduce error in retraction percentages across both the DIC and LDS experiments. With regards to the LDS, more consistent, smooth measurements could be achieved through motor controlled rotation of the LDS. Current set-up requires manual rotation control which could introduce unintended vibration and unsteady measurements along the measurement plane. Of great interest is the outward deflection of the SMA SCF under flow. Previous work by **??** have suggested no change in structural response when exposed to aerodynamic loading. Future work will investigate experimental deflection in the slat cove filler under flow conditions.

4.3 Future Work

Research into the effects of an SMA-based slat cove filler will continue to investigate the aeroacoustic response. At Texas A&M University, researchers will continue work using the CRM-based experimental wing prototype in pursuit of developing useful computational modeling tools to better simulate aerodynamic, structural, and acoustic responses. Potential future concepts include the development and testing of a solid, continuous leading edge slat, reducing mechanical complexity of the wing prototype and improving aerodynamic characteristics of the wing. Investigations into the slat gap filler have been pro-

posed, a similar SMA-based aeroacoustic treatment for the leading edge slat which simulates a drooped-slat instead of the use of acoustic treatments within the slat cove to reduce noise. These concepts, as well as others, will then be used in the investigation and future development of an acoustic wind tunnel test section. Wind tunnel construction, test section geometries, and acoustic treatments will be proposed to develop a system able to directly test the acoustic signature and response of previously developed acoustic wing treatments.

Future experimental and computational developments have been proposed and are in current development to further research into the slat cove filler concept. A solid, full span, stainless steel slat is in fabrication for future experimental testing on the existing wing prototype. The addition of a full span slat allows for improvement in data collection methods, and data quality for experiments conducted on the wing prototype. The solid slat allows for a more rigid structural response when exposed to retraction and aerodynamic loads. The current slat significantly deflects in response to aerodynamic loading at extremely low angles of attack (<1°), when the free stream velocity is nearly perpendicular to the surface of the slat. As well, the full span, solid slat will remove the necessity of the mid-span slat-track system, reducing the exposed frontal area and overall drag force acting on the wing prototype.

The next concept to test the addition of SMA components for use in reducing aeroacoustic emissions from high lift devices is the slat gap filler. Similar noise reduction capabilities are prediction from a design that mimics a drooped slat effect, instead of closing the resulting slat cove during high lift device deployment. The slat gap filler (SGF) works through the use of superelastic SMA closing the gap present when the slat is fully deployed, away from the main wing. When stowed however, the SGF retracts similarly to the SCF except is stored in the leading edge of the main wing. This concept will be tested using the CRM-based wing prototype with slight modifications to allow for stowage in the leading edge of the main wing.

One major limitation currently in developing acoustic treatments is the ability to experimentally test the acoustic response. Acoustic testing in a wind tunnel requires a controlled environment with applicable test equipment. Future work proposes to investigate necessary modifications to the 3'$\times$4' wind tunnel hardware and design, and any application surface treatments for test section upgrades. Necessary test instruments will be determined based upon the scope of acoustic testing proposed. With an upgraded wind tunnel facility capable of meaningful acoustic measurements, the next iteration of the slat cove filler design can be tested for acoustic influence at the Texas A&M University's 3'$\times$4' low speed wind tunnel.

REFERENCES

[1] A. L. Hansell, M. Blangiardo, L. Fortunato, S. Floud, K. de Hoogh, D. Fecht, R. E. Ghosh, H. E. Laszlo, C. Pearson, L. Beale, S. Beevers, J. Gulliver, N. Best, S. Richardson, and P. Elliott, "Aircraft noise and cardiovascular disease near Heathrow airport in London: small area study," *BMJ : British Medical Journal*, vol. 347, Oct. 2013.

[2] P. Maryniak, "New law may offer hope to residents plauged by aircraft noise," *East Valley Tribune*, p. 1, Jan. 2017.

[3] R. Girvin, "Aircraft noise-abatement and mitigation strategies," *Journal of Air Transport Management*, vol. 15, no. 1, pp. 14 – 22, 2009.

[4] C. Clark, "Aircraft Noise Effects on Health," tech. rep., Queen Mary University of London, May 2015.

[5] S. Martens, "Jet noise reduction technology development at ge aircraft engines," *ICAS Paper*, vol. 842, 2002.

[6] F. T. Calkins, J. H. Mabe, and G. W. Butler, "Boeing's variable geometry chevron: morphing aerospace structures for jet noise reduction," vol. 6171, pp. 61710O–61710O–12, 2006.

[7] M. Gorji-Bandpy and M. Azimi, "Airframe noise sources and reduction technologies in aircraft.," *Noise & Vibration Worldwide*, vol. 43, pp. 29–36, Oct. 2012.

[8] D. P. Lockhard and G. M. Lilley, "The airframe noise reduction challenge," 2004.

[9] T. Imamura, Y. Yokokawa, S. Enomoto, K. Yamamoto, and T. Hirai, "Designing of slat cove filler as a noise reduction device for leading-edge slat," *AIAA Paper*, no. 2007-3473, 2007.

[10] T. L. Turner, R. T. Kidd, D. J. Hartl, and W. D. Scholten, "Development of a SMA-Based, Slat-Cove Filler for Reduction of Aeroacoustic Noise Associated With Transport-Class Aircraft Wings," no. 56048, p. V002T02A005, 2013.

[11] T. L. U. Turner, R. T. U. Kidd, D. P. U. Lockard, M. R. U. Khorrami, C. L. U. Streett, and D. L. U. Weber, "Autonomous slat-cove-filler device for recution of aeroacoustic noise associated with aircraft systems," 2016.

[12] W. D. Scholten, R. Patterson, Q. Chapelon, D. J. Hartl, T. W. Strganac, and T. L. Turner, "Experimentation and Computational Assessment of an SMA-Based Slat-Cove Filler For Noise Reduction in a High Lift Wing," in *25th AIAA/AHS Adaptive Structures Conference*, AIAA SciTech Forum, American Institute of Aeronautics and Astronautics, Jan. 2017. DOI: 10.2514/6.2017-0732.

[13] D. C. Lagoudas, *Shape memory alloys : modeling and engineering applications. Dimitris C. Lagoudas, editor.* New York ; London : Springer, [2008], 2008.

[14] J. H. Mabe, F. T. Calkins, and G. W. Butler, "Boeings variable geometry chevron, morphing aerostructure for jet noise reduction," *AIAA Paper No. AIAA-2006-2142*, 2006.

[15] M. G. Dodson, *An Historical and Applied Aerodynamic Study of the Wright Brothers' Wind Tunnel Test Program and Application to Successful Manned Flight*. US Naval Academy, 2005.

[16] J. E. Cermak *et al.*, "Wind tunnel studies of buildings and structures," American Society of Civil Engineers, 1999.

[17] J. Vassberg, M. DeHaan, S. Rivers, and R. Wahls, "Development of a common research model for applied CFD validation studies," in *Collection of Technical Papers - AIAA Applied Aerodynamics Conference*, 2008.

[18] C. H. Wolowicz, J. S. Bowman, and W. P. Gilbert, "Similitude Requirements and Scaling Relationships as Applied to Model Testing," in *NASA Technical Paper 1435*, p. 65, NASA, Aug. 1979.

[19] M. A. Sutton, H. W. Schreier, and J.-J. Orteu, *Image correlation for shape, motion and deformation measurements : basic concepts, theory and applications. Michael A. Sutton, Jean-José Orteu, Hubert Schreier.* New York : Springer, [2009], 2009.

[20] P. Wu, B. Stanford, W. Bowman, A. Schwartz, and P. Ifju, "Digital image correlation techniques for full-field displacement measurements of micro air vehicle flapping wings," *Experimental Techniques*, vol. 33, no. 6, pp. 53–58, 2009.

[21] R. Albertani, B. Stanford, J. Hubner, R. Lind, and P. Ifju, "Experimental Analysis of Deformation for Flexible-Wing Micro Air Vehicles," in *46th AIAA/ASME/ASCE/AHS/ASC Structures, Structural Dynamics and Materials Conference*, Structures, Structural Dynamics, and Materials and Co-located Conferences, American Institute of Aeronautics and Astronautics, Apr. 2005. DOI: 10.2514/6.2005-2231.

[22] J. L. Wagner, S. J. Beresh, K. M. Casper, J. Henfling, R. Spillers, P. Hunter, and R. Mayes, "Experimental Investigation of Fluid-Structure Interactions in Compressible Cavity Flows," in *43rd Fluid Dynamics Conference*, Fluid Dynamics and Co-located Conferences, American Institute of Aeronautics and Astronautics, June 2013. DOI: 10.2514/6.2013-3172.

[23] B. Gwashavanhu, A. J. Oberholster, and P. S. Heyns, "Rotating blade vibration analysis using photogrammetry and tracking laser Doppler vibrometry," *Mechanical Systems and Signal Processing*, vol. 76, pp. 174–186, Aug. 2016.

[24] D. Grandi and U. Stefanelli, "The souza-auricchio model for shape-memory alloys.," *Discrete & Continuous Dynamical Systems-Series S*, vol. 8, no. 4, 2015.

[25] W. D. Scholten, D. J. Hartl, T. L. Turner, and R. T. Kidd, "Development and Analysis-Driven Optimization of Superelastic Slat-Cove Fillers for Airframe Noise Reduction.," *AIAA Journal*, vol. 54, pp. 1078–1094, Mar. 2016.

[26] Y. Babbar, V. S. Suryakumar, and T. Strganac, "Experiments in Free and Forced Aeroelastic Reponse," (Grapevine, Texas), p. 16, AIAA, Jan. 2013.

APPENDIX A

FIRST APPENDIX

METHON Grégory
4th year Mechanical Engineering
2nd Semester 2016-2017

NATIONAL ENGINEERING SCHOOL OF SAINT-ÉTIENNE
58 rue Jean Parot – 42023 Saint-Étienne cedex 2

"Aeroacoustic noise reduction in general transport class aircraft using a shape memory slat-cove filler (SCF). Current research work focuses on computational analysis and wind tunnel testing of scaled SCF models. New testing methods, hardware, and software are needed and may be developed by the student intern."

AEROSPACE ENGINEERING
TEXAS A&M UNIVERSITY

Department of Aerospace Engineering
Texas A&M University
3409 TAMU College Station, TX 77843-3409

Jury:
ENISE advisor: Mr. ROUX Jean-Christophe
Texas A&M University advisor: Dr. HARTL
English teacher: Mr. DORCHIES Ryan

Summary

Table of contents

I-Introduction

This semester I had the chance to do my internship abroad in the Aerospace Department of the Texas A&M University in College Station, Texas, USA. I joined Dr. Hartl and the M²AESTRO laboratory to engage in scientific research. After last year's internship, it was a real chance to do another placement in aerospace. This is a sector I would like to work in during my future career of engineer. Even if my studies at ENISE are mechanical engineering, doing internships in the aerospace sector allow me to broaden my skills and knowledge.

Thanks to this internship, I have learnt a lot of things both on academic and personal prospects. I had the chance to live in Texas, one of the most iconic state of the USA, where I could experience the rich culture through the food and the various traditions.

I'll present, in this report, the main project I was leading for 5 months; the comparison between a wind tunnel testing of a NACA-0012 wing and its computational fluid dynamics model. This project was directly linked to another one, the Slat Cove Filler wing, that I'll present next. I'll also talk briefly about the turbulences measurements in a wind tunnel. All those projects were directly in link with wind tunnel experiments. Finally, I'll conclude this report by both a professional and a personal assessment.

II-Context

1) Texas

Texas, the second largest state in the United States by both area and population, is located in the south central part of the United States of America. Texas is nicknamed "The Lone Star State" to remind its former status as an independent republic, and as a reminder of the state's struggle for independence from Mexico. The "Lone Star" can be found on the Texas state flag and on the Texan state seal. The origin of Texas's name is from the word "Tejas," which means "friends" in the Caddo language.

Location of Texas in the United States of America

The state's economic fortunes changed in the early 20th century, when oil discoveries initiated an economic boom in the state. With strong investments in universities, Texas developed a diversified economy and high tech industry in the mid-20th century. As of 2015, it is second on the list of the most Fortune 500 companies with 54.

The Lone Star flag

Due to its size and geologic features, Texas contains diverse landscapes that resemble both the U.S. Southern and Southwestern regions. You can then encounters prairies, desert, forests, mountains …

While American football has long been considered "king" in the state, Texans today enjoy a wide variety of sports. Texas is home of many professional sports teams: two NFL teams, two Major League Baseball teams, three NBA teams, and one National Hockey League team.

Texans also enjoy the rodeo shows, the world's first rodeo was hosted in Pecos, Texas. The annual Houston Livestock Show and Rodeo is the largest rodeo in the world.

Rodeo in Houston, Texas

Tony Parker playing for the San Antonio Spurs

2) Texas A&M University

The Texas A&M University, often called TAMU, is a public research university in College Station, Texas. The school opened on October 4, 1876 as the Agricultural and Mechanical College of Texas. "Aggie", a diminutive shortening of agricultural, was then given as nicknames for all the students.

Texas A&M logo

Texas A&M graduation ring

With a bit more than 60,000 students and a 21km² campus, TAMU is one the biggest and largest university in America.

In sports, the Aggies are a member of the Southeastern Conference. The best sports teams of the university are the football, basketball and baseball ones. This year, Myles Garrett (defensive end for the football team) was drafted first overall in the 2017 NFL Draft, which means that Texas A&M trained the best university player in the whole country. The sports facilities of the university are impressive; the football stadium, the Kyle Field, is the 5th biggest stadium in the world. (more than 106,000 seats).

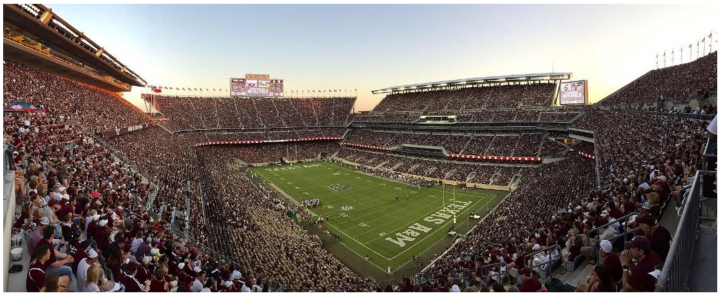

The Kyle Field stadium of Texas A&M, during a game.

3) M²AESTRO Laboratory

The Multifunctional Materials and Aerospace Structures Optimization (M²AESTRO) Lab is the research team of Dr. Darren J. Hartl. The M²AESTRO laboratory is part of the Aerospace department of Texas A&M.

The laboratory capabilities include a customizable 3'x4' wind tunnel test section for acquisition of fully three-dimensional surface deformation, strain, and thermal fields as measured on adaptive aerospace structures in a flow environment.

III-The Project

1) Objective

The objective of this study was to make a comparison between results from wind tunnel testing of a NACA-0012 wing and a corresponding computational fluid dynamics (CFD) model in order to validate our SC-Tetra model. The process includes the use of wind tunnel, the development of a computational model, using a Scanivalve scanning pressure transducer and the post processing of the results. The Scanivalve integrates all of the electronics for the analog-to-digital (A/D) conversion process and a processor supporting the engineering unit conversion process and all communications overhead, results are directly exported to a ".txt" files containing all the pressure datas in Pascal. These datas will be, then, compared to the pressure values extracted from the CFD model. This validation was done so wind tunnel tests could be run on more complex airfoils (i.e. the Slat Cove Filler wing) knowing the setup and experimental plans were good and reliable.

2) Hands-on engineering

To conduct all the experiments, the following setup has been used:
-NACA-0012 airfoil
-A closed-loop wind tunnel with a 0.91m x 1.22m (3ft x 4ft) test section at Texas A&M University
-Scanivalve MPS4264 (Pressure scanner)

The NACA-0012 wing is a symmetric airfoil; the equation for the outer mold line is:

$$y = 182.4 \times (0.2969 \times \sqrt{\frac{x}{c}} - 0.126 \times (\frac{x}{c}) - 0.3516 \times (\frac{x}{c})^2 + 0.2843 \times (\frac{x}{c})^3 - 0.1015 \times (\frac{x}{c})^4)$$

With x: abscissa along the chord, c: chord and $0 < \frac{x}{c} < 1$

We will set $\frac{x}{c} = 0$ as the leading edge and $\frac{x}{c} = 1$ as the trailing edge.

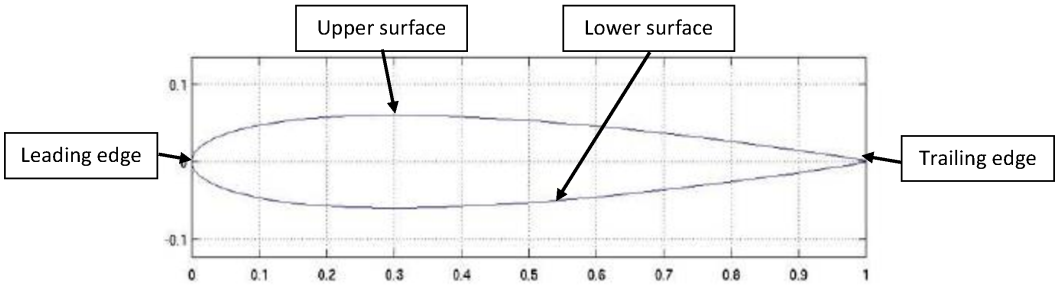

NACA-0012 airfoil

The NACA-0012 wing is known as a “validation airfoil”, it is used as a validation case for turbulence models. “NACA” stands for “National Advisory Committee for Aeronautics”.
The wing prototype, which will be experimentally tested, has 50 pressure ports spaced all along the chord of the airfoil. The wingspan is 3 feet and the chord is 303mm.

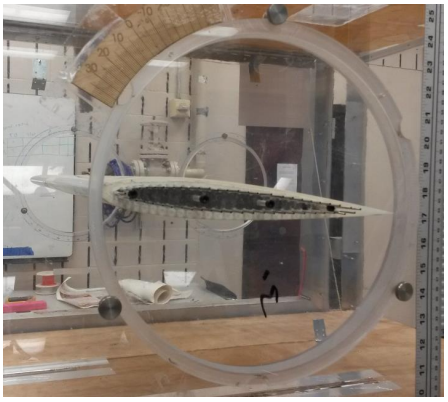

NACA-0012 airfoil in the wind tunnel test section

The wind tunnel is a closed loop design, with a 3ft x 4ft test section providing full aero structural morphing testing capabilities.

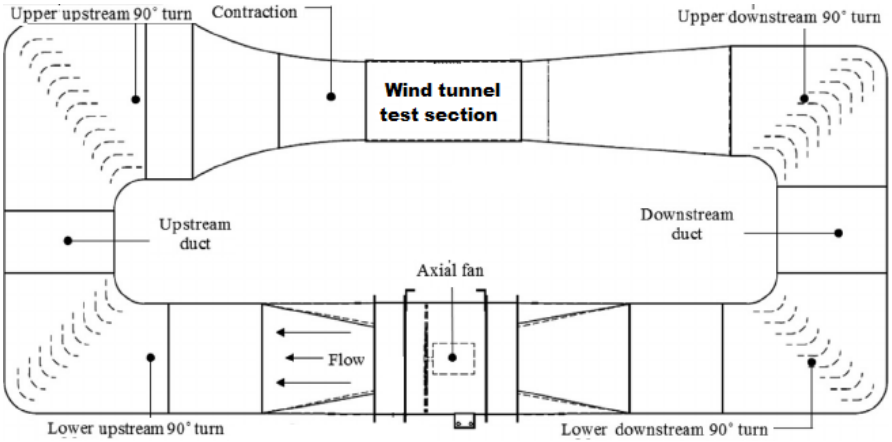

Close loop wind tunnel drawing

As the wingspan is 3 feet and the test section is 4 feet wide, a 5mm thick Plexiglas splitter plate was installed in order to hold the wing on its end and approximate a semi-infinite wing (no wingtip effects).
The splitter plate was fixed with flat angle brackets and screws both on the floor and on the ceiling to ensure the stability of the wing and to avoid vibrations.

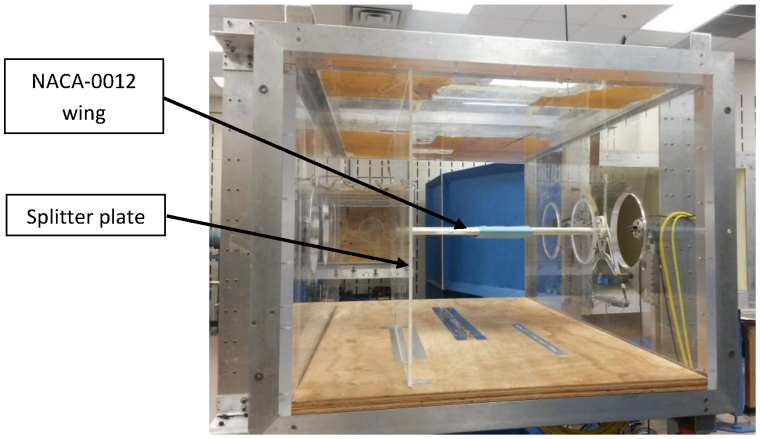

3ft x 4ft wind tunnel section

The Scanivalve device, used in this work, is a Miniature Ethernet Pressure Scanner. The pressure ports of the NACA-0012 are plugged on the device, with pressure tubing, which analyzes in real time the pressures applied on the airfoil. The device has 64 channels, 50 of them were used for our tests. This device shows an accuracy of 0.06% of the ±1 PSI total pressure range.

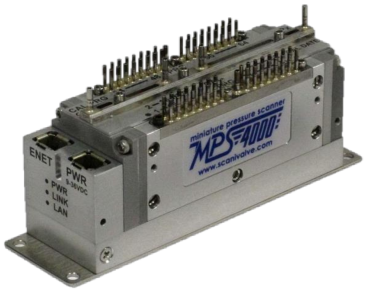

Scanivalve MP4264

The post processing of the data consist of averaging the values recorded for all the pressure ports. During the tests, the frame per scan was set on 100 and the scan rate on 10, which means we collected 100 values for every channel during 10 seconds.
Those values were averaged in order to summarize this large amount of data into one set of values for all the pressure ports. Averaging was also useful as it indicates the variability around this single value within the original data.

Once the data is post processed, we use the following formula of pressure coefficient to normalize our results:

$$C_p = \frac{P - P_\infty}{\frac{1}{2} * \rho * v^2} \text{ with } \begin{cases} P \text{ static pressure} \\ P_\infty \text{ freestream pressure} \\ \rho \text{ air density} \\ v \text{ air velocity} \end{cases}$$

A pitot tube inside the wind tunnel, forward of the wing which measures the freestream pressure is directly plugged into the Scanivalve device that includes
The 'REF' port ties into a manifold that connects the back side of all transducers together. The 'REF' port of low pressure modules (below 15 psi) has to be be routed to a known, stable static location. Typically this "reference" location will be a wind tunnel static port such as a pitot tube for example.

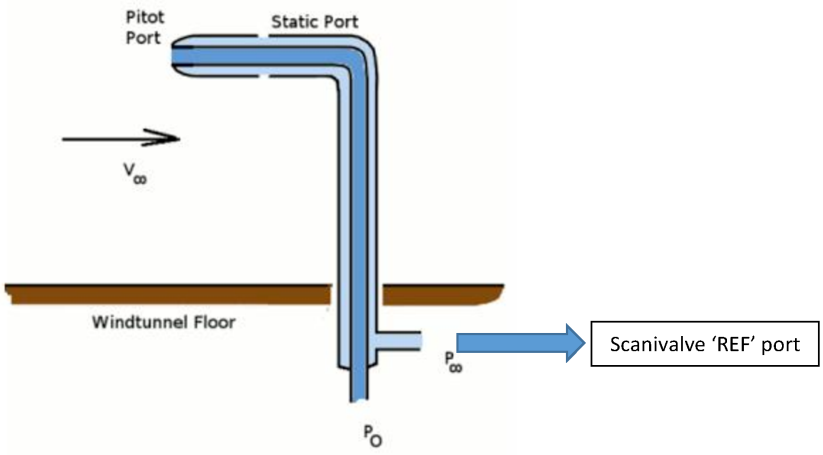

Scheme of a Pitot tube, similar to the one we installed.

The device automatically subtracts the measured freestream pressure from the static pressure of each channel.
The formula becomes:

$$C_p = \frac{\Delta P}{\frac{1}{2} * \rho * V^2}$$

To create the plots, that are Cp function of x/c, the pressure taps had to be located.
Using a caliper and a Matlab code, in order to have the best accuracy, the coordinates for the pressure ports were found and summarized in the appendix (see Annex.1).

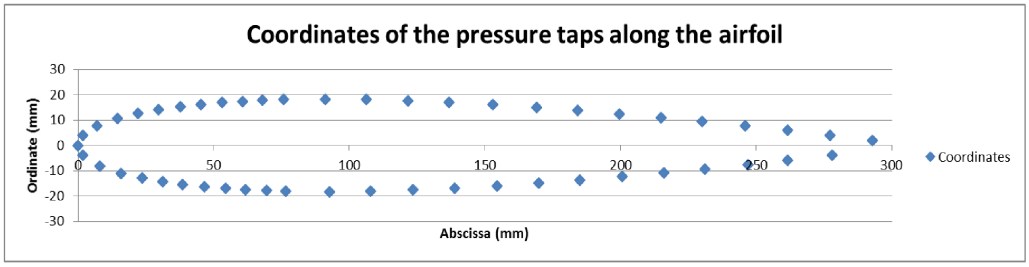

Regarding the experimental plan, the tests were run at two different speeds (15 and 25m/s) and six different angles of attack (0, 2, 4, 6, 8 and 10°). Tests were not performed for negative angle as our airfoil is symmetrical.

Before running any tests, it is imperative to record the pressures read by the Scanivalve without air velocity (V=0m/s). These values will be called “windoff”, it represent the pressure values read while it should indicate “0 Pa”. For all the tests made, we will have to subtract the windoff values to obtain the corrected pressure values. This procedure is similar as the tare function on a balance.

3) Computational Fluid Dynamics

a) Abaqus

Note: All the values in Abaqus are in meters

Abaqus is a software suite used for finite elements analysis, it allows to model and analyze mechanical components and assemblies.
I used Abaqus to reproduce our experimental setup that is made up of the wing airfoil inside the wind tunnel section.
The first of the computational fluid analysis was to create the wing airfoil in Abaqus. The sketch has been created by importing the coordinates of the airfoil. Then, the tool "Create Lines/Connected" allowed me to link all those points to create the following airfoil.

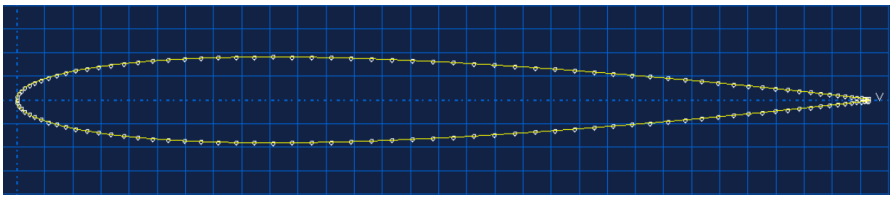

NACA-0012 airfoil representation in Abaqus

The two next steps are then to create the wind tunnel test section and two areas of interest around the wing. All we will proceed to a 2 Dimension analysis in SC Tetra (one element in spanwise direction), the section will viewed from the side.

Regarding the first step, we will proceed by creating a "solid extrude" and fill the different dimensions of our setup. The wing is located in the middle of the section that is 2 meters long and 0.9 meter high, we then obtain the next sketch.

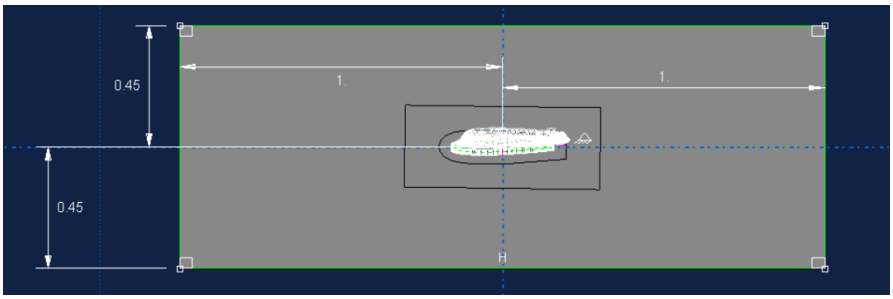

Abaqus view of the wind tunnel section from the side

The second one, called “areas of interest”, I created two different size of areas. One (in red) is a rectangle and the other one (in yellow), drawn closer to the airfoil, has an airfoil shape. Later, when running the CFD, we will use these areas to reduce our meshing around the wing to get results the most accurate possible. The bigger the areas are, the more results you will get but the longer will take the analysis to be done. We can then jump from minutes to hours if we expand to much this area. To create this area, I’ve used the feature “partition face”.

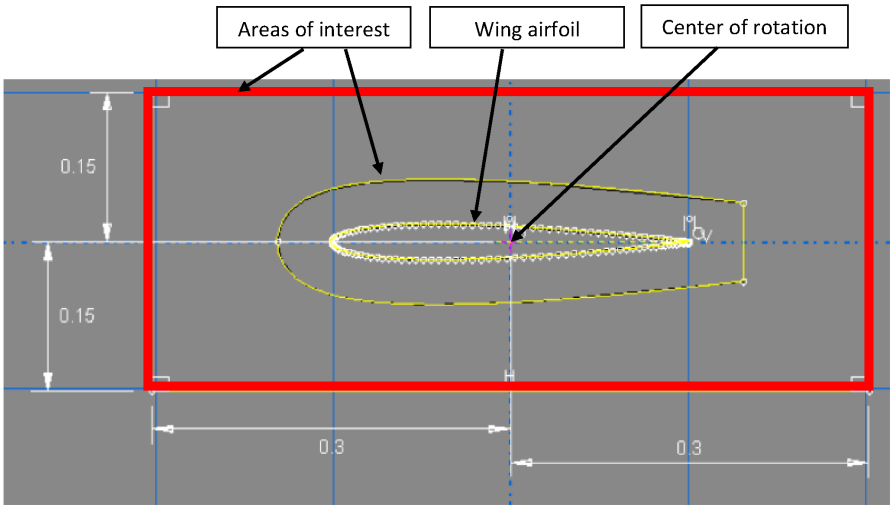

Areas of interests for the NACA-0012 CFD study

Note: I created a center of rotation (located 50% of the chord) that will be used to rotate the wing in the different Angle of Attack (AoA) we need.

b) SC Tetra CFD and meshing

SC/Tetra software was used to run the Abaqus model. SC/Tetra is a general purpose thermo-fluid simulation software using hybrid mesh to represent the surface shape with high accuracy. It will allow us to simulate the air flow inside the wind tunnel section, and then extract the pressure data applied on the airfoil. We will also be able to see how the flow behave in the tunnel section.

The main concern will be to create a model and set the boundary conditions as close as possible to the reality. Parameters will be set and a meshing created, the mesh (can also be called “grid”) is the basis for all simulation software and studies. Create a mesh is like representing a geometric object as a set of finite elements, it divides our model in cells.

All the flow variables & any other variables are solved at centers of these discrete cells. The meshing has to be fine enough to have good results but now too fine or the solving time can jump to days, weeks …

I imported the models previously designed in Abaqus .

First step was to create the materials and the different faces of the system. In this study, we need to use two different materials, one for the wing and one for the flow. Obviously, we will set the flow as "incompressible/air" and the wing material as a metal (copper for example).

Then, we can set the boundary conditions.
The walls of the wind tunnel section (ceiling and floor in the 2D representation) will be set as free slip surfaces. The "no-slip" boundary condition is the most commonly used as it's the closest of the reality; indeed, the fluid/surface friction is really small. The shear stress is close to zero/negligible.
The faces that had to be defined were: the inlet, the outlet, the WT ceiling, the WT floor and the wing contour.

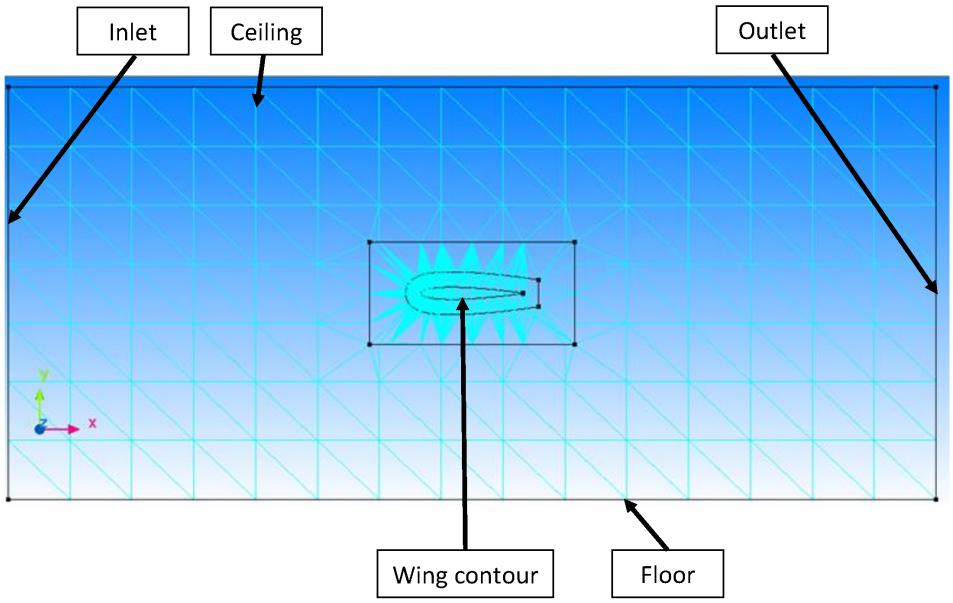

Regarding the air flow properties:
Inlet is defined as a 15m/s air flow. (Or 25m/s depending of the study).
Outlet is set as "0Pa, static pressure" face. Setting the pressure equal to zero at the outlet results in a zero pressure gradient along the length of the test section. This allows a uniform flow to enter and exit the model at approximately the same velocity. If the outlet pressure is not zero, then the flow will either accelerate or decelerate depending on the sign of the outlet pressure.

The recommended (and most convenient) outlet condition is a gage static pressure equal to 0. No other boundary conditions should be applied to an outlet with a Pressure = 0 condition.

We also have to define the areas we will use to create the mesh. We will define 3 kind of areas, depending of their importance, we will call them: full, medium and fine. Both the medium and the fine areas have been explained and detailed in the Abaqus part (page.12). The area "full" represents the area of the test section, it doesn't need to be really accurate so its meshing will be the biggest. The "medium" is an area closer to the wing, the mesh will be smaller than the previous one. And the "fine" is the area really close to the airfoil that needs to be really precise, its mesh will be really fine so we can get accurate values.

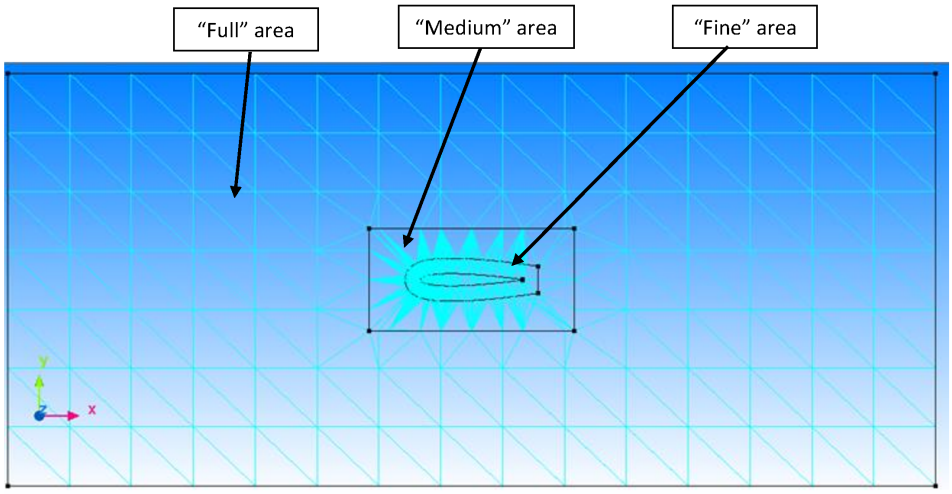

The result of the meshing will be as follow:

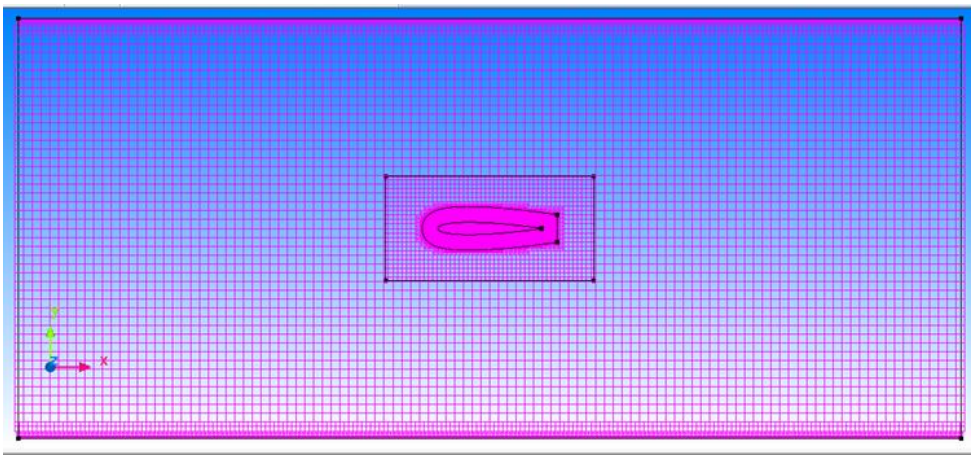

Meshing of a NACA-0012 airfoil at 0°angle of attack

We will solve this model in a steady analysis. We will use this method, and not the transient analysis, because we have unchanging conditions with time.

This meshing is composed of 4 million elements and takes an hour to be solved by the computer. The model has to be run for all the different configurations (12 times in total).

c) Results and comparison

As said previously, the pressure coefficient plots are used to compare the experimental data extracted from the wind tunnel tests with the CFD values. All the plots are summarized in the appendix (see Annex.2).

The blue dashed curve represents the experimental data and the solid orange one symbolizes the CFD results. We notice that both these curves perfectly match at 0° angle of attack, and a 25m/s freestream velocity.

The 0° plot is really important as it allows us to be sure we set correctly the angle of attack in our experimental setup.

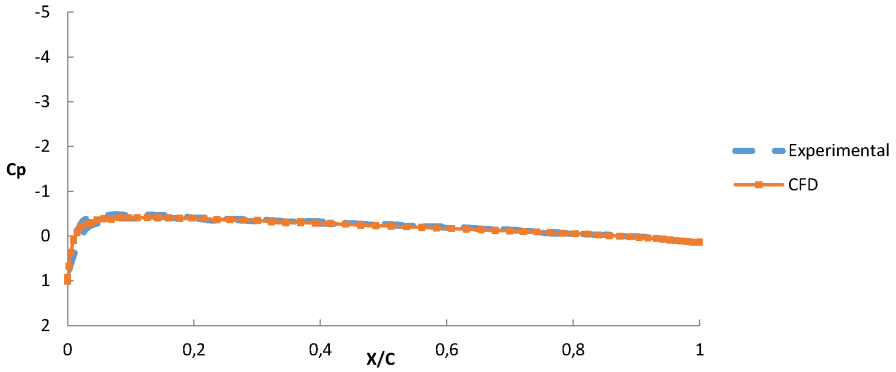

Cp function of X/C, 0° angle of attack with a freestream velocity of 25 m/s

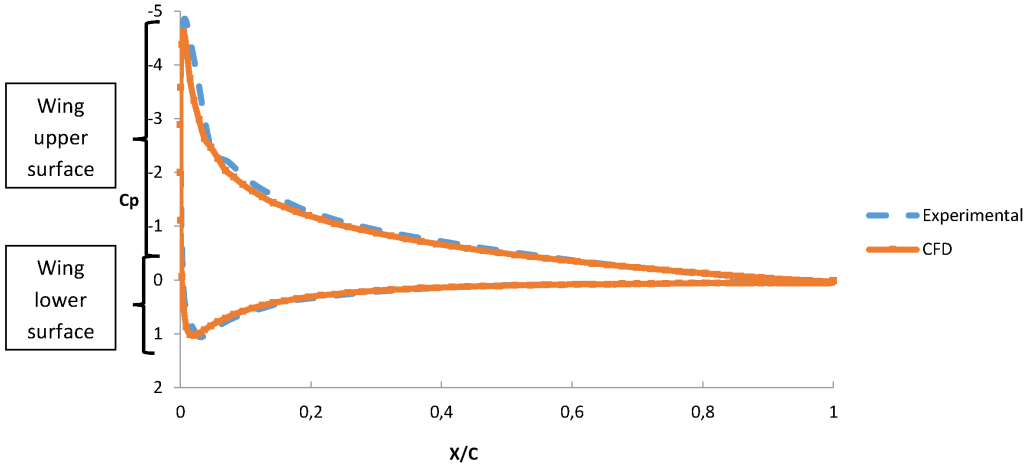

Cp function of X/C, 10° angle of attack with a freestream velocity of 25 m/s

On the previous plot, we can note a slight shift between the experimental and CFD curves between 0 and 0.2 X/C on the wing upper surface, we can evaluate the scientific credibility of these results.
We can study, in greater detail, this shift in order to know its importance and if it's a problem or not in our data correlation.

In the chart below, I listed 9 different pressure taps between 0 and 0.2 X/C on the upper surface of the wing in order to compare the CFD and experimental pressure values.

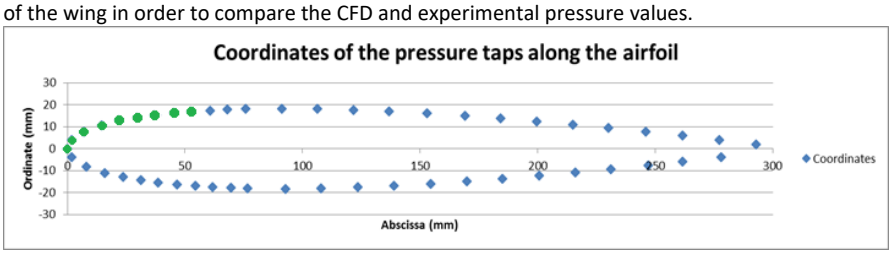

In green, the 9 pressure taps studied in the chart

X/C	CFD Pressure (Pa)	Experimental Pressure (Pa)	Delta Pressure (Pa)	Delta Pressure (%)
0,20	-470	-500	30	5.6
0,18	-510	-540	30	5.6
0,12	-610	-660	50	7.5
0,10	-710	-760	50	6.5
0,07	-800	-860	60	6.9
0,05	-930	-950	20	2.1
0,02	-1370	-1570	200	14.5
0,01	-1730	-1900	170	9.8
0	-1350	-1340	10	0.7

How can this shift be explained?

- Air flow velocity, the air flow is set on 25m/s in the wind tunnel but it appears to be closer to 25.1 & 25.2m/s depending of the tests
- Angle of attack precision in the setup. A slight shift of the wing AoA from 10° to 9.9° (or 10.1°) can lead to higher delta pressure, especially around the leading edge.

Is the shift a problem?
Except one value above 10%, the delta pressure appears to be really low (5% in average). It only concerns 9 points on the airfoil (where the pressure gradient is the most important, at the leading edge), the other 41 points perfectly match the CFD results.

We can conclude that this shift is not a problem and we can validate the scientific credibility of these results.
Note: SC/Tetra also allows us to visualize the pressure distribution on the airfoil.

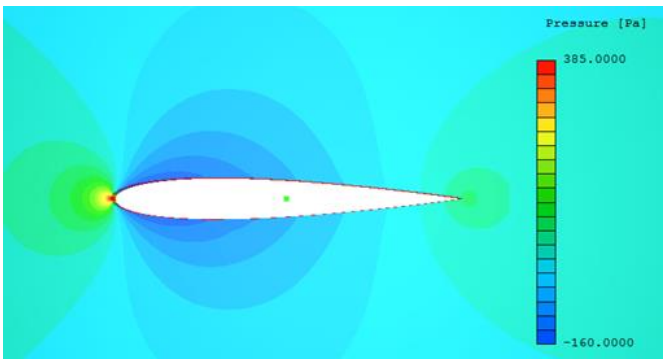

Pressure distribution for the NACA-0012 airfoil at 0° angle of attack with a freestream velocity of 25 m/s

4) Conclusion

This study was successful as you can see of the previous plots and the ones in the appendix. We have correlated the values between the experimental datas and the CFD models which was the main objective of this study.

Through the wind tunnel tests and CFD analysis, we have learnt a lot about the use of the Scanivalve device, the experimental plans to run tests on an airfoil and modeling a system in Abaqus and solve it with SC/Tetra. Thanks to this validation, we can now proceed to assessment of other airfoils such as the AVIAN wing or the "Slat Cove Filler wing".

IV-Slat cove filler wing

1) The project

This project was started in 2014 at the NASA with Dr. Turner and then studies were lead in the Aerospace department at Texas A&M. The main goal of the project is to reduce the noise of the airplane during the low speed maneuvers. A significant source for this noise is the cove of the leading-edge slat. A slat-cove filler (SCF) has been shown to be effective at mitigating slat noise.

The wing prototype has been designed and built in 2015 during the internship of a previous ENISE student: Jeff Volpi. He built this wing with PhD student William Scholten and the wing is actually at the heart of Ryan Patterson's master thesis.

The wing was conceived with 15 pressure taps and a deployable slat.

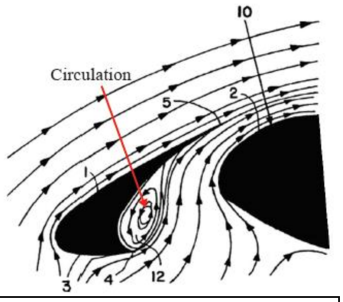

Illustration of flow in region of slat for a conventional airfoil

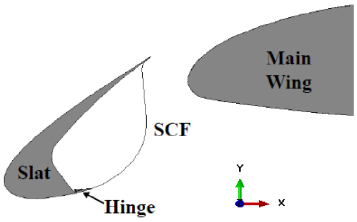

Slat cove filler design

2) The setup and experiments

To lead these tests, we have used the same kind of setup that we used for the NACA-0012 wing experiments but we also added a new technology to the setup: the Digital Image Correlation (DIC).

The DIC is an optical method that employs tracking and image registration techniques for accurate 2D and 3D measurements. This is often used to measure deformation, displacement and strain but it is widely applied in many areas of science and engineering. The DIC setup is composed of 2 cameras with lenses and 2 software (one to record during the tests and the other to post process the data).

The first step of the DIC process is to apply a “speckle pattern” on the slats we have to study. This consists of painting the area of the slat where the lenses are focused on. We used two different kind of slats: the first one, called “untreated”, without any slat cove filler (SCF) and a second one, called “treated”, with SCF. The main goal was to make a CFD comparison for both cases.

On the right: View of the slat cove filler

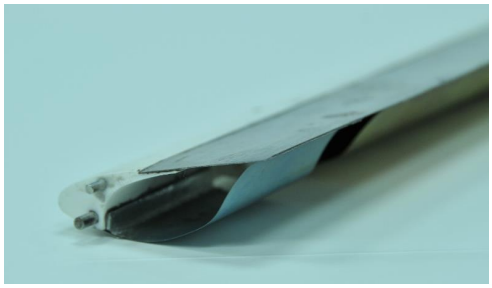

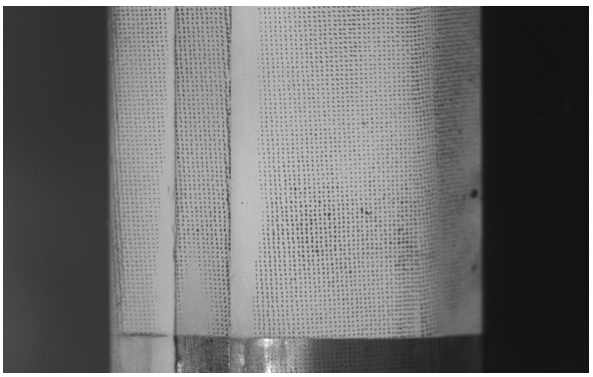

On the left: Speckle pattern applied on the slat

On the right: Slat cove filler prototype wind inside the wind

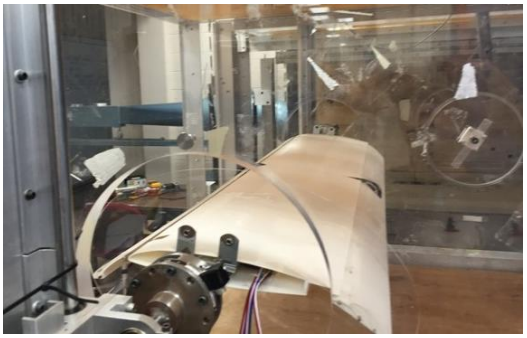

On the left: lenses setup under the wind tunnel section. Lenses aim at a Plexiglas panel installed on the floor of the wind tunnel.

The tests were run at two different speeds (15 and 25m/s) and six different angles of attack (0, 2, 4, 6, 8 and 10°). In this case, we also had to perform tests for negative angles as the airfoil is asymmetrical (not as the NACA-0012 wing).

However, these tests have been run for different configurations, depending of the slat used and its position.

We ran the tests with two different positions: fully deployed and fully retracted.

View of the wing inside the test section.

<u>Note:</u> In the experimental plan below, UT means Untreated slat, T means Treated slat.

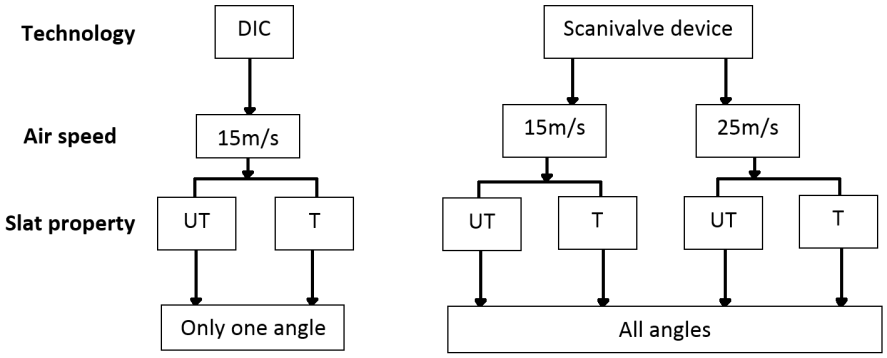

Experimental plan for the SCF-wing

The main limit of the DIC process is that the cameras needs to be always focused on the speckle pattern, so we can't use the DIC for all the angles of attack.

Using the Scanivalve device and the DIC setup, allow us to lead two comparisons with the fluid-structure interaction (FSI) model of W.Scholten. The Scanivalve will have the same role than in the NACA-0012 study: we will use the device to record the pressure values and compare it to the CFD data. The DIC will be focused on the slat cove filler and will allow us to see how the prototype interacts with the wing in the wind tunnel. We will be able to study the deformation, displacement, we will know how and when the SCF deploys/retracts.

3) Results

Unfortunately, as we made these tests during my last weeks at Texas A&M, I didn't have time to post process all the data we recorded (both Scanivalve and DIC data). Ryan Patterson is working on the post-processing for his thesis.

V-Turbulences measurements

1) Hot-wire technology

During this internship, I was also asked to study the hot-wire technology in order to record the turbulences in the airflow of the wind tunnel.

1D hot wire probe

A hot-wire anemometer is composed of a thin heated wire, that wire is kept as constant temperature. During the test, the wire is cooled down by the air flowing in the wind tunnel section, the voltage that keeps the hot wire at the same temperature is analyzed to determine the turbulences.

Even if the hot wire is really delicate to use, it offers a good resolution to know the changes of speed in the flow.

I, then, had to compare and choose between 1D, 2D or 3D probes, all had advantages and drawbacks. I created a decision matrix taking into account: if it matches our need, the accuracy, the price, the repair price (hot wire break really easily), calibration process difficulty.

The grades are from 1 to 3, 1 being the best and 3 the worst.

	Need	Accuracy	Price	Rep. Price	Calibration	Total
1D probe	1	1	1	1	1	5
2D probe	1	1	2	1	2	7
3D probe	2	3*	3	2	3	13

Simplified view of the decision chart

**3D probe might generate turbulence by itself which is dependent on the flow speed (Reynolds number). The wires of the 3D probe are 14 times thicker than the wires of the XW probe and the geometry of the 3D probe is much more complex.*

Regarding the results of the decision matrix, it was decided to purchase single sensors hot wire to lead our research.

2) In a near future

Unfortunately we didn't get all the equipment before I left College Station.

Once the equipment will arrive at the laboratory, it will be possible to calibrate and record the turbulences in the wind tunnel.

Conclusion

1) Professional

During this internship I had the chance to run a lot of wind tunnel experiments but also to work on computational fluid dynamics (CFD) models. Working both on hands-on experiences and theoretical models allowed me to learn a lot. The wind tunnel of the M²AESTRO lab was essential and very convenient to run all the experiments. I found really interesting to have to compare the experimental and computational data. The importance of this task helped me to overcome obstacles to finally find the solutions we were expecting and have a reliable structure to run the tests on other kind of wings.

At the end of my internship I had the opportunity, with Ryan Patterson, to run tests of the slat cove filler wing. It was really gratifying to continue the work that had been done on this wing by the previous ENISE students.

I also had the opportunity to use some of the knowledge acquired during ENISE classes such as: fluid mechanics and numerical simulation. Both these classes helped me to have a better understanding of what was asked to me to do and how to achieve my goals. I discovered a lot of new technologies that I didn't know before this internship. I could learn how worked different lab projects such as: shape memory alloys (SMA), liquid metal actuators and the digital image correlation (DIC). Working and taking a look on all these technologies was enriching.

To sum up, this internship helped me to improve my capability in many different fields but also to expand my knowledge on other topics I didn't know before.

2) Personal

Regarding my future engineer career, I would like to continue to work in the aerospace sector. Last year I already had the chance to work in an aerospace company in France and this internship is the confirmation that I would like to work in this sector later. Furthermore, I would like to try to work abroad especially in English speaking countries like the United States or the United Kingdom. This placement helped me to understand that it was really important to add value to my engineering diploma, this is why I've decided to do a Master degree, next year, for my 5th year of engineering school.

This internship has also been really enriching on a touristic point of view. As my internship period was shifted for a couple weeks I had the opportunity to visit different states before and after my internship: California (Los Angeles, San Francisco), Nevada and the East Coast (NYC, Philadelphia, Washington). With another intern of the laboratory we had the opportunity to visit Louisiana. We had the chance to experience the "Cajun" culture by visiting New Orleans and Lafayette, we also made a swamp tour in a world famous bayou, and this was an amazing and unforgettable experience.

Acknowledgments

I would like to thank:

- Dr. Hartl, my American advisor, for his help and his advices all along my internship
- Dr. Strganac and Dr. Turner, for their analysis and observations on our weekly NASA meetings
- PhD Student William Scholten for his availability and his guidance to learn more about Computational fluid dynamics
- Master Student Ryan Patterson for his help to do the experiments with the wind tunnel, the scanivalve device and the DIC setup.
- Dr. Roux from ENISE for his support as my school advisor
- Mr. Dorchies as my English tutor for this internship
- The international relations department of ENISE (Mrs. Favier and Mrs. Lietard) for making this internship possible.
- All the students from the M²AESTRO Laboratory for their help and their kindness, truly amazing people.

References & Key-words

References:

-Theory of wing sections, by Abbott & Doenhoff
-Reduction of actuation loads in a self-deploying SMA-based slat-cove filler for a transport aircraft (2015), W.Scholten, Dr.Hartl, Dr.Strganac, Dr.Turner

Key-words:
Airfoil
NACA-0012
Wind tunnel
Turbulences
Computational fluid dynamics
SC Tetra
Abaqus
Digital Image Correlation
Slat Cove Filler

Appendix

Annex.1

```
%% Finding x (and y) coordinates of every pressure taps of the NCACA0012 wing

clear; clc;

% Parameters

Rexpected = input ('What is the distance between the taps?')
x0 = input('What is the x coordinate of the previous point?')
y0 = input('What is the y coordinate of the previous point?')
c = 304 ;
xi = x0 + 0.01;
X = xi/c ;

%Calcul de yi

yi= (182.4)*((0.2969*sqrt(X))-0.126*X-0.3516*(X^2)+0.2843*(X^3)-0.1015*(X^4))

R=sqrt(((xi-x0)^2+((yi-y0)^2)))

while R<=Rexpected
  xi = xi + 0.01
  X=xi/c
  yi= (182.4)*((0.2969*sqrt(X))-0.126*X-0.3516*(X^2)+0.2843*(X^3)-0.1015*(X^4))
  R=sqrt(((xi-x0)^2+((yi-y0)^2)))
end
Resultatxi = xi,
Resultatyi = yi,
```

Annex.2

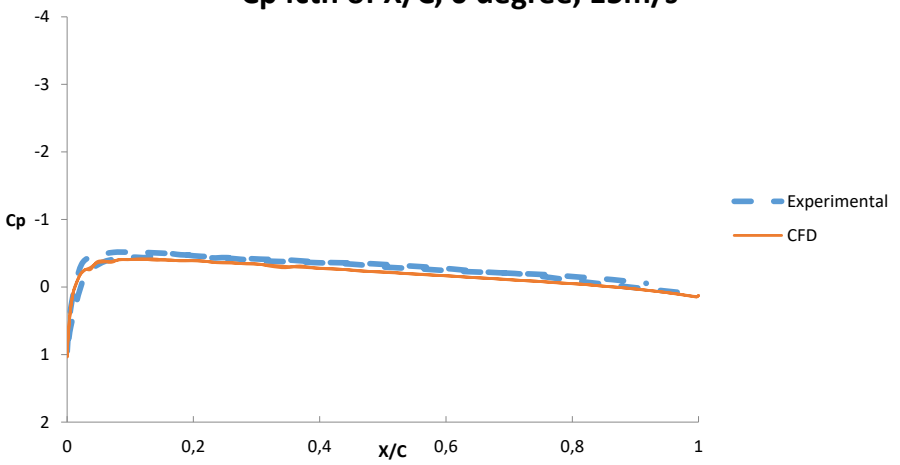
Cp fctn of X/C, 0 degree, 15m/s
-4
-3
-2
Cp -1
0
1
2
0
0,2
0,4
X/C
0,6
0,8
1
Experimental
CFD

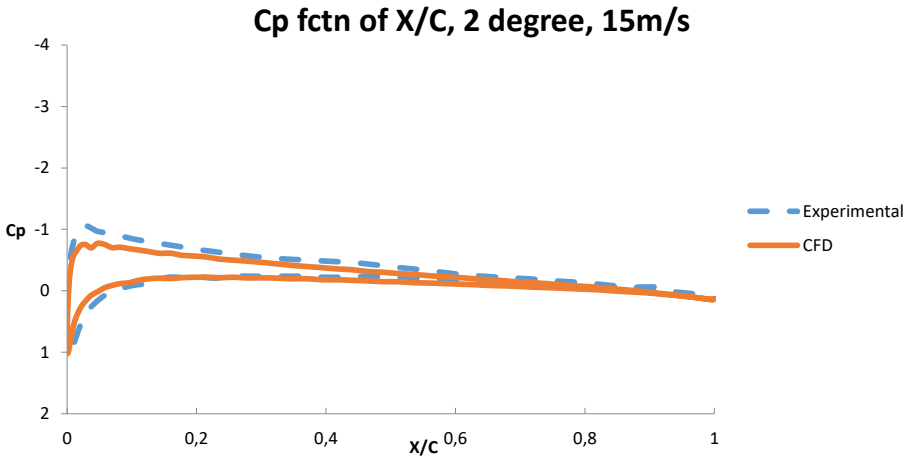
Cp fctn of X/C, 2 degree, 15m/s
-4
-3
-2
Cp -1
0
1
2
0
0,2
0,4
X/C
0,6
0,8
1
Experimental
CFD

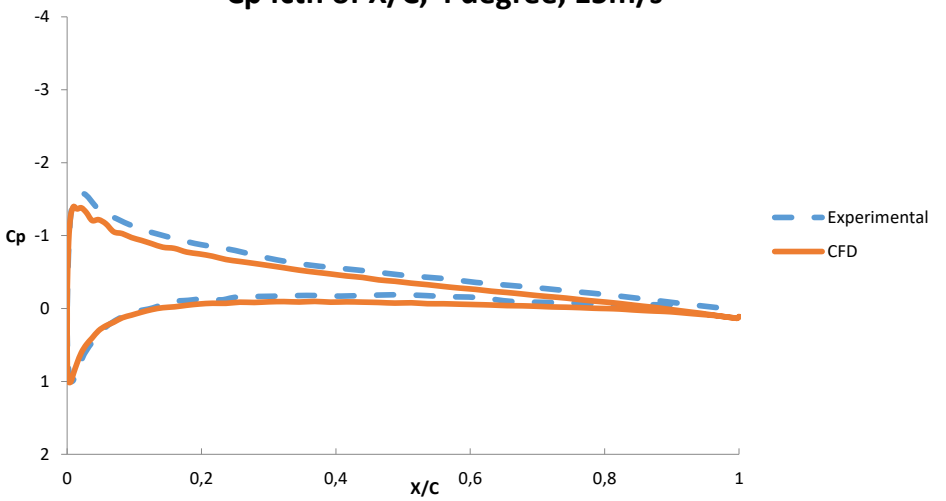
Cp fctn of X/C, 4 degree, 15m/s
-4
-3
-2
-1
0
1
2
Cp
0
0,2
0,4
0,6
0,8
1
X/C
Experimental
CFD

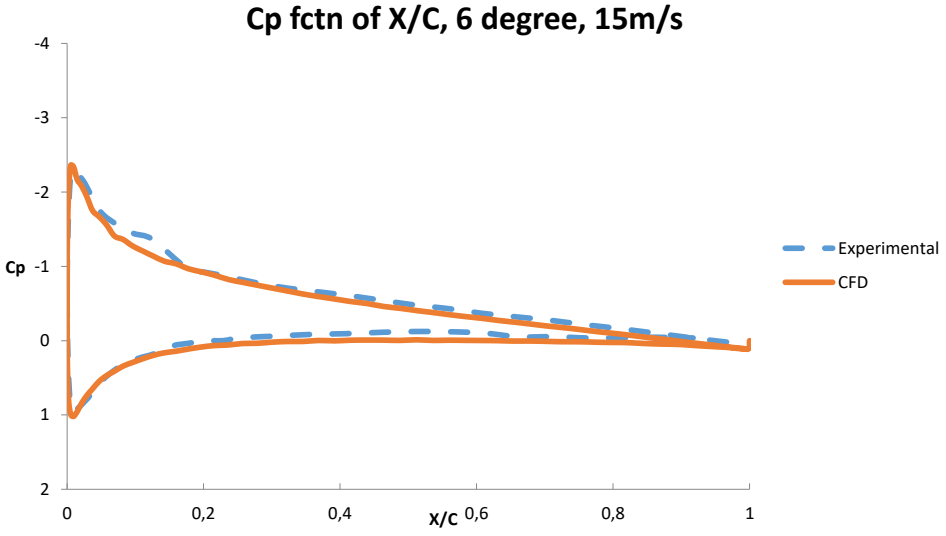
Cp fctn of X/C, 6 degree, 15m/s
-4
-3
-2
-1
0
1
2
Cp
0
0,2
0,4
0,6
0,8
1
X/C
Experimental
CFD

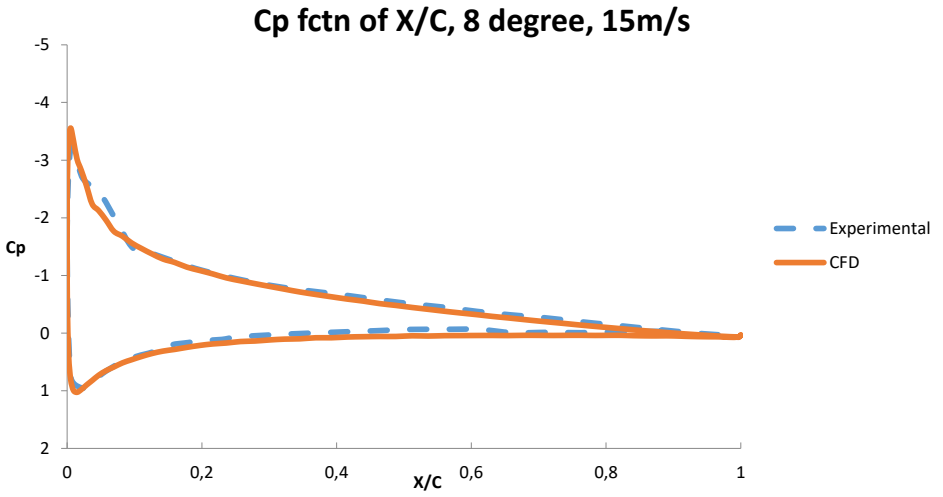
Cp fctn of X/C, 8 degree, 15m/s
Cp
X/C
-5
-4
-3
-2
-1
0
1
2
0
0,2
0,4
0,6
0,8
1
Experimental
CFD

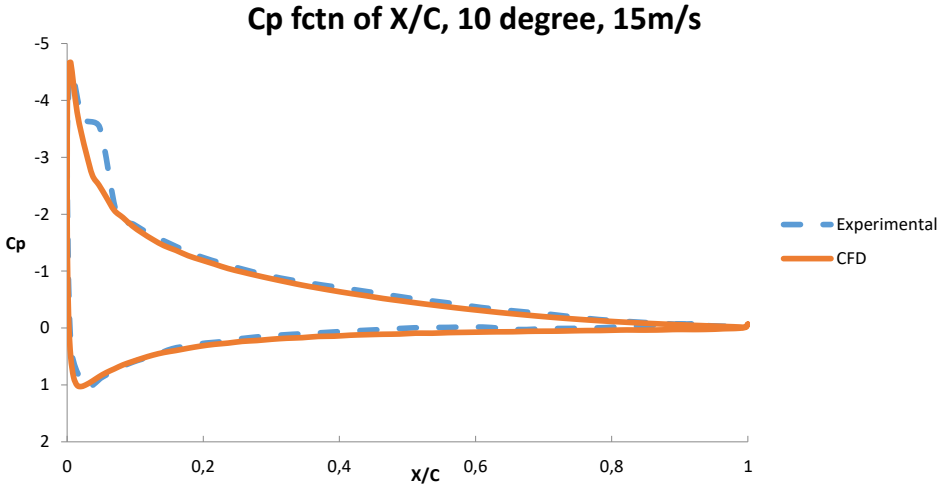
Cp fctn of X/C, 10 degree, 15m/s
Cp
X/C
-5
-4
-3
-2
-1
0
1
2
0
0,2
0,4
0,6
0,8
1
Experimental
CFD

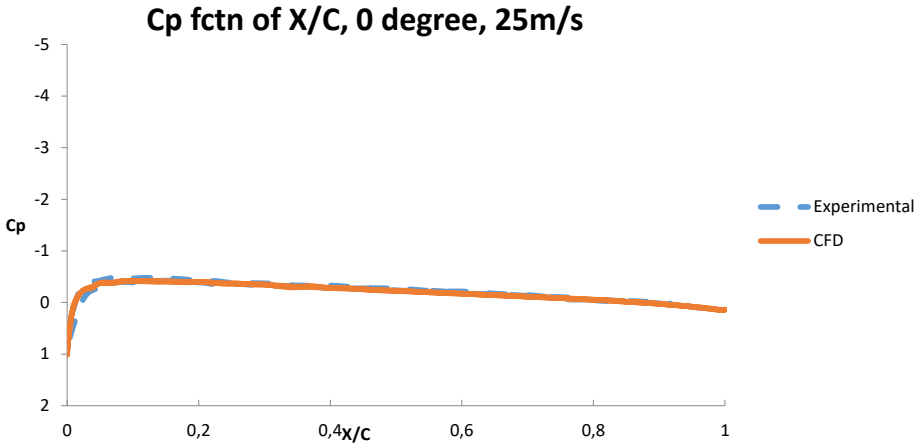
Cp fctn of X/C, 0 degree, 25m/s
Cp
-5
-4
-3
-2
-1
0
1
2
0
0,2
0,4
X/C
0,6
0,8
1
Experimental
CFD

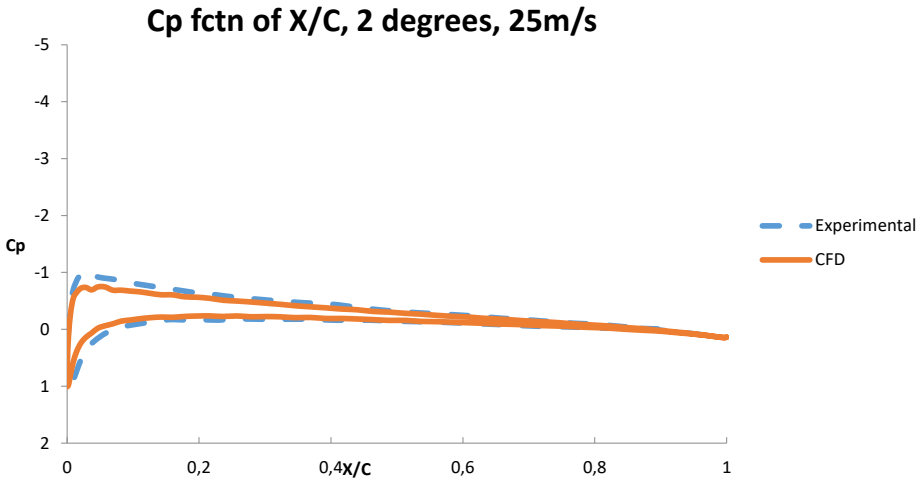
Cp fctn of X/C, 2 degrees, 25m/s
Cp
-5
-4
-3
-2
-1
0
1
2
0
0,2
0,4
X/C
0,6
0,8
1
Experimental
CFD

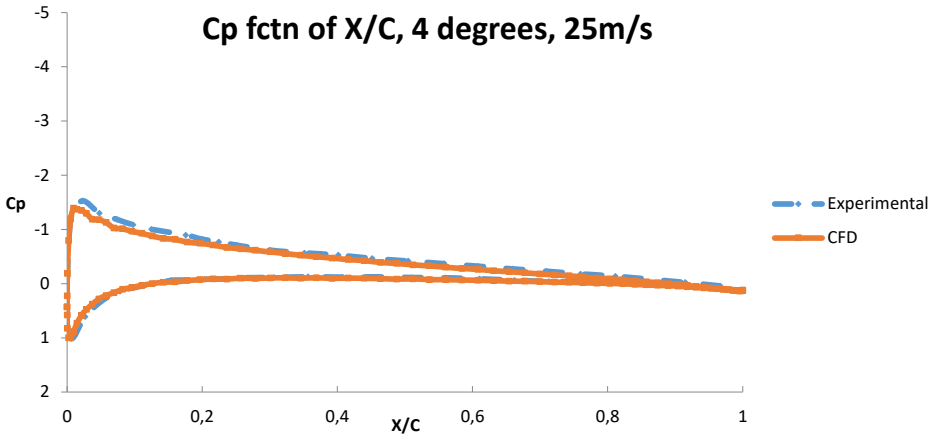
Cp fctn of X/C, 4 degrees, 25m/s
Cp
-5
-4
-3
-2
-1
0
1
2
0
0,2
0,4
0,6
0,8
1
X/C
Experimental
CFD

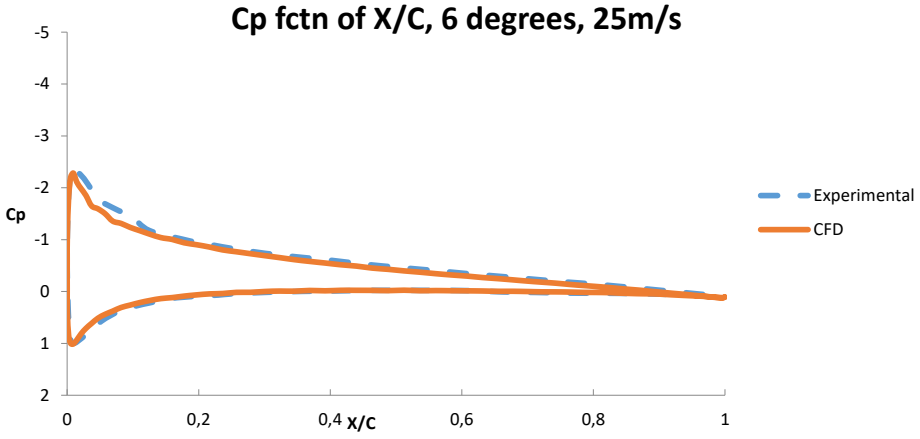
Cp fctn of X/C, 6 degrees, 25m/s
Cp
-5
-4
-3
-2
-1
0
1
2
0
0,2
0,4
0,6
0,8
1
X/C
Experimental
CFD

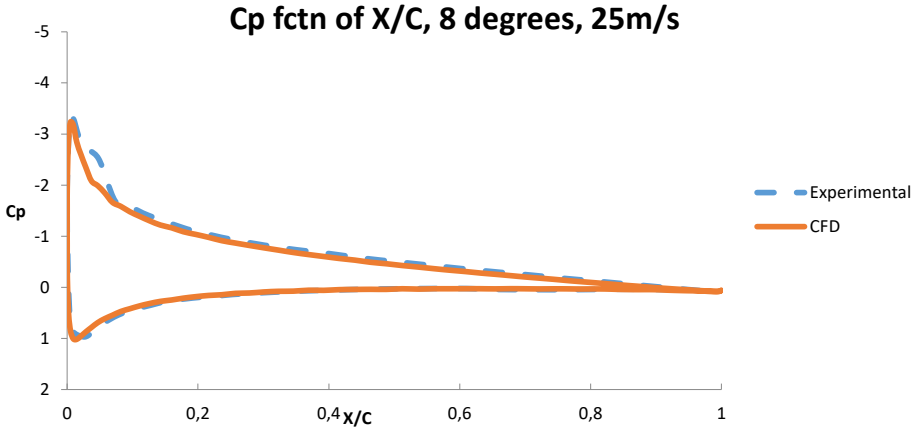
Cp fctn of X/C, 8 degrees, 25m/s
Cp
X/C
Experimental
CFD

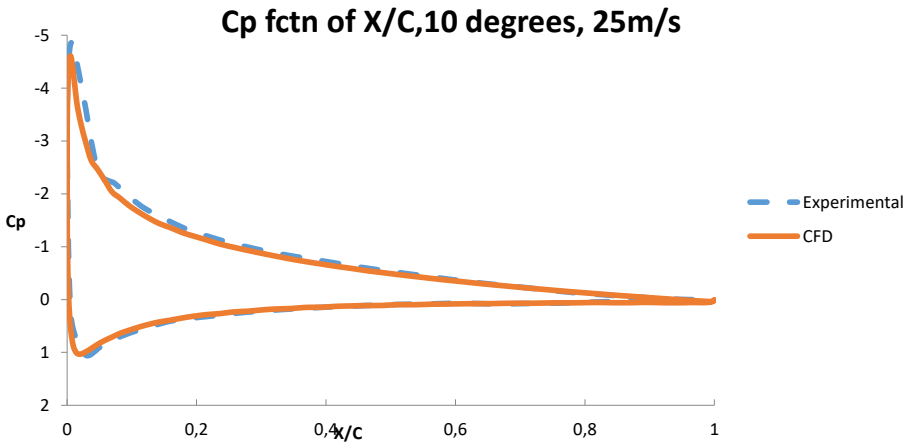
Cp fctn of X/C,10 degrees, 25m/s
Cp
X/C
Experimental
CFD